University of California
Santa Barbara

Zinc-IV-nitrides and scandium nitride for novel heterostructure applications

A dissertation submitted in partial satisfaction
of the requirements for the degree

Doctor of Philosophy
in
Electrical and Computer Engineering

by

Nicholas Lloyd Adamski

Committee in charge:

Professor Chris G. Van de Walle, Co-chair
Professor Steven DenBaars, Co-chair
Professor Umesh Mishra
Professor Chris Palmstrom

June 2020

The Dissertation of Nicholas Lloyd Adamski is approved.

Professor Chris Palmstrom

Professor Umesh Mishra

Professor Steven DenBaars, Committee Co-Chair

Professor Chris G. Van de Walle, Committee Co-Chair

June 2020

Zinc-IV-nitrides and scandium nitride for novel heterostructure applications

Nicholas Lloyd Adamski

To Grandpa Lloyd, who got me building early

Acknowledgements

I'd like to acknowledge the many people who helped me through my PhD. First, I'd like to thank my advisor, Dr. Chris Van de Walle, for taking me into his group and letting me work on the properties and materials I was most interested in. He is an incredible author and editor, and I hope to have absorbed some of that knowledge. Next, I'd like to thank my co-authors, Drs. Zhen Zhu, Darshana Wickramaratne, and Cyrus Dreyer, who were essential in brainstorming and workshopping ideas. Darshana and Cyrus in particular were crucial points of advice long after they had left the group. I could not have made it this far without their continual support.

I'd like to thank Michael Swift and Jimmy Shen for interesting discussions in physics and in all topics. Hartwin Peelaers and Wennie Wang taught me many useful tips for navigating the group early on, and were a great resource for computational advice and information. I also appreciated the interesting discussions and group meetings with Santosh KC, Azzedin Jackson, Leigh Weston, Karthik Krishnaswamy, and Youngho Kang.

The current members of Chris' group also deserve a lot of appreciation. I'd like to thank Andrew Rowberg for teaching me bridge. Mark Turiansky has helped me understand some of the more computer science aspects to materials science. Xie Zhang, Sai Mu, Stephanie Mack, and Mengen Wang have provided me with many interesting discussions and advice on my research.

More broadly, I'd like to thank my committee members, Chris Van de Walle, Steve DenBaars, Chris Palmstrom, and Umesh Mishra. I had the privilege of taking two courses with each of them, and it provided me with a foundation on which to base my whole degree. Each of them and their groups continue to push out research that supplies a plethora of seminars and presentations that has fueled my interest in semiconductors and devices.

Lastly, I'd like to thank my support networks. My local friends Adam, Daniil, and Carol, who've helped keep me distracted. My friends back home, in particular John, Henry, Andrew, and Stephanie, who've helped me keep a level head throughout. And to all my online friends, who have perhaps had to put up with me the most. On campus, I'd like to thank the support staff, Val De Veyra at ECE, Tal Margalith, Yukina Warner, and David Whitlatch at SSLEEC, and Paul Weakliem at CSC. Finally I'd like to thank my family. My parents Peter and Sandy who kept my mind on the goal when I was losing focus. And my brother Elliott and my extended family, who think I'm cut out for this.

The work described in this dissertation was supported by the Army Research Office under award number W911NF-16-1-0538 and by the Air Force Office of Scientific Research under Award No. FA9550-18-1-0237.

Curriculum Vitæ

Nicholas Lloyd Adamski

Education

2020	Ph.D. in Electrical and Computer Engineering, University of California, Santa Barbara.
2015	M.Sc. in Electrical and Computer Engineering, University of California, Santa Barbara.
2014	B.Sc. in Electrical Engineering, University of Alberta.

Awards

2019	American Physical Society Ovshinsky Student Travel Award
2019	Solid State Lighting and Energy Electronics Center Graduate Student Award

Publications

1. Christian Mounir, Ingrid L. Koslow, Tim Wernicke, Michael Kneissl, Leah Y. Kuritzky, Nicholas L. Adamski, Sang Ho Oh, Christopher D. Pynn, Steven P. DenBaars, Shuji Nakamura, James S. Speck, and Ulrich T. Schwarz, "On the optical polarization properties of semipolar $(20\bar{2}1)$ and $(20\bar{2}\bar{1})$ InGaN/GaN quantum wells", *Journal of Applied Physics* **123**, 085705 (2018).
2. Nicholas L. Adamski, Zhen Zhu, Darshana Wickramaratne, and Chris G. Van de Walle, "Hybrid functional study of native point defects and impurities in $ZnGeN_2$," *Journal of Applied Physics* **122**, 195701 (2017).
3. Nicholas L. Adamski, Zhen Zhu, Darshana Wickramaratne, and Chris G. Van de Walle, "Strategies for p-type doping of $ZnGeN_2$", *Applied Physics Letters* **114**, 032101 (2019).
4. Nicholas L. Adamski, Zhen Zhu, Darshana Wickramaratne, and Chris G. Van de Walle, "Optimizing n-type doping of $ZnGeN_2$ and $ZnSiN_2$", *Physical Review B* **100**, 155206 (2019).
5. Nicholas L. Adamski, Cyrus E. Dreyer, Chris G. Van de Walle, "Giant polarization charge density at lattice-matched GaN/ScN interfaces", *Applied Physics Letters* **115**, 232103 (2019).
6. Nicholas L. Adamski, Darshana Wickramaratne, and Chris G. Van de Walle, "Band alignments and polarization properties of the Zn-IV-nitrides", *Journal of Materials Chemistry C*, Advance Article (2020), [doi:10.1039/D0TC01578D].

Contributed Talks

2017	American Physical Society March Meeting, New Orleans, LA "Structural and electronic properties of $ZnGeN_2$"
2018	American Physical Society March Meeting, Los Angeles, CA "Strategies for p-type doping in $ZnGeN_2$"
2018	Nitrides Seminar, Santa Barbara CA "II-IV-nitrides for optoelectronic applications"
2018	Gordon Research Seminar: Defects in Seminconductors "Defects and doping in $ZnGeN_2$"
2018	Solid State Lighting and Energy Electronics Center Annual Review, Santa Barbara CA "II-IV-nitrides for optoelectronic applications"
2019	American Physical Society March Meeting, Boston MA "Polarization engineering with novel nitride heterostructures from first principles "
2019	Nitrides Seminar, Santa Barbara CA "Giant polarization charge density at lattice-matched GaN/ScN interfaces"
2019	Solid State Lighting and Energy Electronics Center Annual Review, Santa Barbara CA "Giant Polarization Charge Density at GaN/ScN Interfaces"
2019	Asia-Pacific Workshop on Widegap Semiconductors, Okinawa Japan "Zn-IV-nitrides for integration in electronic and photonic devices"

Abstract

Zinc-IV-nitrides and scandium nitride for novel heterostructure applications

by

Nicholas Lloyd Adamski

The wurtzite III-nitrides are an established set of wide-band-gap semiconductors with a wide range of applications in optical and electronic devices. Recently, new types of nitride semiconductors have been proposed to widen the range of accessible parameters and device applications. One class of such materials are the Zn-IV-nitrides, which have strong structural and electronic similarities to the III-nitrides. The predicted band gaps are desirable for optical devices operating in the visible spectrum, while the predicted band alignments to III-nitrides enable applications that are not achievable with III-nitrides alone. Another alternative nitride is ScN, which has the rocksalt crystal structure, but has a very small lattice mismatch to GaN. In this work, I thoroughly examine structural and electronic properties of these materials crucial to understanding and evaluating their application in devices.

In the Zn-IV-nitrides, we focus on $ZnGeN_2$, which has a very close lattice match to GaN, making it the most approachable of the Zn-IV-nitrides for integration with III-nitrides. We examine the conductivity by determining the stability of native point defects and dopants. We find that, in the absence of dopants, native defects will ensure $ZnGeN_2$ is insulating. To *n*-type dope the material, we find that P_{Ge} acts as a shallow donor with low formation energy. For *p*-type doping, we find that Al_{Ge} is a viable acceptor, with an acceptor level 0.24 eV from the valence-band maximum. However, there is strong compensation due to wrong-site doping of Al_{Zn}. This issue can be overcome by co-doping with hydrogen, and the hydrogen can be removed in a post-growth anneal.

We also thoroughly examine band alignments and polarization properties among all the Zn-IV-nitrides.

Lastly, we consider interfaces between rocksalt ScN and wurtzite GaN, and show how polarization charges can be calculated at this non-polar/polar interface. We demonstrate an extremely large polarization discontinuity of –1.358 Cm^{-2}, and propose that a ScN could be used as an interlayer in a tunnel junction device.

Contents

Chapter 1

Introduction

1.1 Wide-band-gap semiconductors

Wide-band-gap semiconductors have had huge economic impact since the invention of the gallium nitride-based blue light-emitting diode (LED) in the early 1990s [1]. The III-nitride materials system—based on alloys and heterojunctions between AlN, GaN, and InN—has lead to the development of smaller and more efficient light emitters: enabling portable electronics, the Blu-ray optical storage format, and a variety of other applications. GaN-based electronics have also been developed for transistor applications, making use of high breakdown fields [2] and high polarization charges for high-frequency and power conversion applications [3]. Research on these materials continues to evolve with the desire to expand the emission spectrum of LEDs to both shorter and longer wavelengths, higher efficiencies, and lower costs.

With these thoughts in mind, we look to expand the capabilities of these systems by exploring other materials that can be integrated with the III-nitrides materials system. The II-IV-nitrides are a class of materials based on the III-nitrides, where each pair of group-III cations is replaced by a group-II element and a group-IV element in an ordered

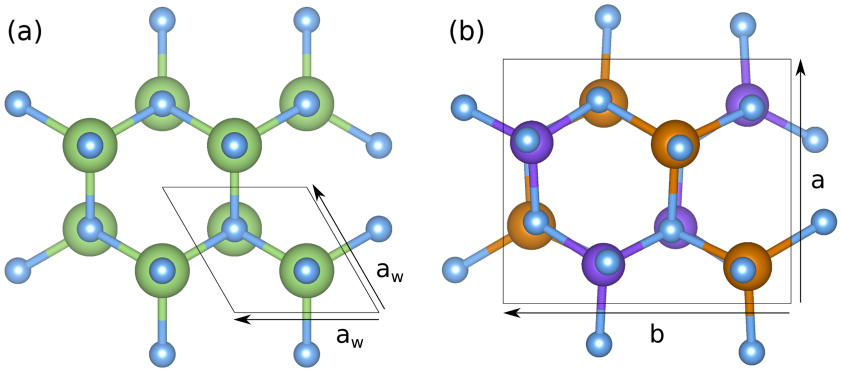

Figure 1.1: (a) Wurtzite GaN and (b) orthorhombic $ZnGeN_2$ crystal structure viewed along the c axis. The respective primitive unit cells are shown with a black outline. a_w is the in-plane lattice parameter for GaN, while a and b are the in-plane lattice parameters for $ZnGeN_2$.

fashion [4]. Such materials satisfy the octet rule, and are observed to have similar physical and electrical properties as the material they are based on [5]. For example, $ZnGeN_2$ shares strong similarities with GaN, as Zn has one less electron than Ga, but Ge has one more electron than Ga. These materials provide high flexibility, as it is possible to alloy on both the group-II site (with Mg or Cd) and on the group-IV site (with Si or Sn) as a means to tune the properties of the material.

The III-nitrides have the wurtzite crystal structure (space group $P6_3mc$), which has a hexagonal lattice. The substitution, changing two group-III ions for the pair of group-II and IV ions results in a reduction of symmetry to $Pna2_1$ with an orthorhombic lattice; the overall crystal structure is very similar. The similarities between the structures of GaN and $ZnGeN_2$ are illustrated in Fig. 1.1.

In selecting an appropriate material for a light emitter, we are primarily concerned with its band gap. The band gap of a semiconductor determines the wavelengths of light that will be absorbed and emitted. The band gap is the energy between the lowest unoccupied state in the conduction band, or conduction-band minimum (CBM), and the highest occupied state in the valence band, or valence-band maximum (VBM). These

band edges are different for different materials, and the alignment of band edges between different materials is important for understanding their macroscopic properties and thus a significant point of my study.

Another important property is the conductivity, which is impacted by the presence of charged point defects within the material. Native point defects (defects within pure material) include vacancies, interstitials, and antisite defects [6], while dopants (other elements) can be substitutional or interstitial. Each defect can exist in a variety of charge states, and understanding the properties of defects within each material is crucial to determining its suitability for device applications.

Light-emitting diodes function by confining both holes and electrons into a narrow region [7]. This is done by growing a double heterostructure, where a material with a smaller band gap is grown between two layers of a wider band-gap material. Electrons localize at the lowest part of the conduction band and holes localize in the highest part in the valence band. In heterostructures with a type-I band alignment, both electrons and holes will localize in the material with the smaller gap. Electrons and holes recombine and emit a photon of light (with energy approximately the band gap of the smaller gap material).

To reach high carrier concentrations, one of the wide-gap layers is doped p-type (containing acceptors), while the other is doped n-type (containing donors) [8]. As an example, in GaN, Mg is used to dope the material p-type, as Mg has one less electron than Ga and the Mg_{Ga} substitutional defect will capture an electron, leaving a hole in the valence band. Similarly, Si_{Ga} acts as a donor and is used to dope GaN n-type. In considering $ZnGeN_2$ and $ZnSiN_2$ as materials for integration with III-nitride devices, I examine a variety of elements that could be used for either n- or p-type doping.

A key feature of the III-nitride system is the strong spontaneous and piezoelectric polarization along the c axis due to their wurtzite crystal structure. The polarization

results in polarization charges at heterointerfaces and produces electric fields. These charges are undesirable in GaN/InGaN/GaN quantum-well structures, as they spatially separate electrons and holes, reducing recombination efficiency [9]. However, they can be beneficial in electronic devices, as free electrons will move to compensate the polarization charge, resulting in high-density two-dimensional electron gases (2DEGs) [3]. These electron gases can be modulated for transistor applications.

Working within ternary alloy systems, such as the InGaN/GaN system (where InGaN films are grown on GaN), band gaps and polarization properties are linked [10]. That is, a specific band gap can only be achieved for a specific $In_xGa_{1-x}N$ alloy concentration, which also yields a specific spontaneous polarization. This limits design possibilities, as it is not possible to engineer the polarization properties while keeping the band gaps and alignments constant. To add design flexibility, growth along nonpolar and semipolar axes has been employed, which reduces the effect of the polarization. Using the quaternary AlInGaN has also been considered to reach new combinations of band gap and polarization; however, growth of this quaternary is challenging as AlN and InN growth have very different ideal temperature ranges. I examine the II-IV-nitrides as another potential solution: with a new set of band gaps, alignments, and polarization properties, it will be possible to engineer II-IV-nitride/III-nitride interfaces with properties that are not achievable within the III-nitride system.

Lastly, I will examine polarization in nitrides more generally. While most research has studied wurtzite nitrides, there are some nitrides, such as ScN [11] and YN, that take the rocksalt crystal structure (space group $Fm\bar{3}m$. The rocksalt structure, being centrosymmetric, does not exhibit any macroscopic polarization; however, it is possible to create epitaxial interfaces between the wurtzite nitrides and these rocksalt nitrides. In particular, GaN and ScN have a very small lattice mismatch. Therefore, this provides a unique opportunity to examine interfaces between polar and nonpolar materials. I show

that such an interface results in polarization charges an order of magnitude larger than at wurtzite-wurtzite interfaces, which may be applicable for tunnel junctions in nitride devices.

1.2 First principles modeling of semiconductors

Before we delve into properties of materials, we must first examine how we calculate those properties. The computational framework that is most widely used is density functional theory (DFT), a so-called first-principles method. The following summary is based on *Electronic structure: basic theory and practical methods* by Richard M. Martin [12] and *Density functional theory: A practical introduction* by David Sholl and Janice A. Steckel [13]. For further reading, I would recommend those two textbooks.

In quantum physics, each system has a wavefunction Ψ that solves the time-independent Schrödinger equation,

$$H\Psi = E\Psi \ . \tag{1.1}$$

$H = T + U$ is the Hamiltonian of the system, and comprises the kinetic energy T and the potential energy U. The potential energy term is different depending on the system. There are eigenfunctions Ψ, which solve the equation, yielding a set of associated eigenenergies. In a simple atomic model, each atom comprises a nucleus, with a positive charge, and one or more electrons. Charges interact via the Coulombic interaction,

$$U = \frac{q_1 q_2}{4\pi\epsilon_0 r} \ , \tag{1.2}$$

where q_i is the charge, ϵ_0 is the dielectric constant of free space, and r is the separation.

Our first approximation is to model the nuclei as fixed point charges—the Born-Oppenheimer approximation. As the nuclei are much heavier than the electrons, they

will move orders of magnitude less, and can reasonably be approximated as fixed in space. Our focus shifts entirely to the electrons.

The simplest system, the hydrogen atom, has only a single electron and can be solved analytically and exactly. The lowest energy wavefunction describes an electron which is spread out in space, spherically symmetric about the nucleus. The square magnitude of the wavefunction returns the probability density of finding the electron at each point.

Moving first to single-atom systems with many electrons—with the goal of ultimately moving to many-atom systems—the equations quickly become much more complicated. The Hamiltonian can be written as

$$H = \sum_i \left(\frac{-\hbar^2 \nabla_i^2}{2m} + \frac{Ze^2}{4\pi\epsilon_0} \frac{1}{|r_i|} \right) + \sum_i \sum_{j>i} \frac{e^2}{4\pi\epsilon_0} \frac{1}{|r_i - r_j|} \ . \tag{1.3}$$

While the first two terms are familiar: the kinetic energy and the electron-nucleus interaction, the last term is a double sum, depending on the position of two electrons at the same time. The wavefunction of the system depends on all the electron coordinates $\Psi = \Psi(r_1, r_2, ...r_N)$. For a crystal, with multiple atoms, we get the Hamiltonian:

$$H = \sum_i \frac{-\hbar^2 \nabla_i^2}{2m} + \frac{e^2}{4\pi\epsilon_0} \left(\sum_i \sum_{j>i} \frac{1}{|r_i - r_j|} + \sum_{i,I} \frac{Z_I}{|r_i - R_I|} + \sum_I \sum_{J>I} \frac{Z_I Z_J}{|R_I - R_J|} \right) \ , \tag{1.4}$$

where the upper-case indices are used to indicate the nuclei.

The Hamiltonian in Eq. (1.4) becomes unwieldly as its complexity scales with the number of electrons and ions. To reduce the computational complexity, we turn to electron-density-based methods as a solution. The electron density is the square of the wavefunction integrated over all-but-one of the coordinates:

$$n(r_1) = N \int d^3 r_2 \int d^3 r_3 ... \int d^3 r_N |\Psi(r_1, r_2, ...r_N)|^2 \ . \tag{1.5}$$

Hohenberg and Kohn [14] demonstrated in their first theorem that the ground-state energy is a unique functional of the electron density, and their second theorem states that the density that minimizes the energy of the functional is exactly the electron density corresponding to the solution of the full Schrödinger equation. The analytic form of the functional that satisfies the Hohenberg-Kohn theorem is not known exactly, and determining suitable approximations that give accurate results has been an ongoing focus in the field of density functional theory.

The classical Coulomb interaction can be written out in terms of the electron density as follows:

$$E^{\text{Coulomb}} = \int d^3r V_{\text{ext}}(r) n(r) + \frac{1}{2} \int d^3r d^3r' \frac{n(r)n(r')}{|\mathbf{r} - \mathbf{r}'|} + E_{\text{nuclei}} \ . \tag{1.6}$$

In the first term, V_{ext} is the potential corresponding to the atomic nuclei in the system. The second term, also called the Hartree energy, describes the electron-electron interaction. Lastly, the nucleus-nucleus interaction is not written out as it is a constant with respect to the electron density. Several important issues emerge by inspecting this expression for the classical Coulomb energy. Firstly, the electron-electron term includes interactions from every electron interacting with every electron, including each electron interacting with itself, which is unphysical. (Consider the case where there was only one electron: the electron-electron term should be zero, but clearly is not.) Secondly, it neglects the effects of the Pauli exclusion principle, a restriction that electrons with the same spin cannot occupy the same state. Further, we have not addressed how kinetic energy can be described as a density functional, as the exact form of the kinetic energy as a function of the density is not known. These issues are handled by the Kohn-Sham equations, which demonstrate an ansatz which can be used to reformulate the problem into a set of single-electron equations.

The Kohn-Sham system describes a set of non-interacting particles that result in the same electron density as the full interacting system. The wavefunctions of the particles are the eigenfunctions of the equation

$$\left[-\frac{\hbar^2}{2m_e}\nabla^2 + V_{\text{ext}}(\mathbf{r}) + V_{\text{Hartree}}(\mathbf{r}) + V_{XC}(\mathbf{r})\right]\phi_i(\mathbf{r}) = \varepsilon_i\phi_i(\mathbf{r}) \ . \tag{1.7}$$

As the equation is based on single-particle wavefunctions, it is simple to express the kinetic energy in closed form. The V_{ext} and V_{Hartree} are the same as before, but the new term V_{XC} captures all of the quantum mechanical information that was lacking. XC stands for eXchange and Correlation, and it attempts to correct for the energy difference that occurs as a result of Pauli interaction and correlation between electrons. It also corrects the kinetic energy, as the proper expression for the kinetic energy needs to account for electron-electron interactions. As the other terms have well defined formula, it is this V_{XC} term that is the most mutable, which gives rise to many 'flavors' of density functional theory, each with its own expression for the exchange-correlation functional.

Once the functional has been settled on, the procedure finds a ground state using iteration. First a density is assumed, and single-particle wavefunctions are determined using the Kohn-sham equations. A new density is calculated from the Kohn-Sham wavefunctions. The cycle is repeated self-consistently until the density is converged. From the density, a total energy for the ground state can be calculated. Forces can be computed from derivatives in the total energy with respect to ionic coordinates. These forces can be used to determine the atomic coordinates that result in the lowest energy.

The simplest functional is the local-density approximation, where the XC functional is simply a function of the density. More sophisticated models allow the XC functional to vary as a function of derivatives of the density. These are the *generalized-gradient approximation* (GGA) functionals; my work often makes use of the Perdew-Burke-Ernzerhof

(PBE) functional [15]. However, these functionals have significant drawbacks: first, they severely underestimate the band gap, second, they do not fully account for the self-interaction portion of the Hartree energy, which results in inaccurate predictions for localized charges.

There are numerous methods that have been employed to correct for these issues. Hybrid functionals mix the XC functional from the approximations above with exact exchange from Hartree-Fock theory. Hartree-Fock theory solves the multi-electron Schrödinger equation using a Slater determinant which treats the Pauli exclusion principle appropriately. It also avoids the self-interaction issue in the Hartree term. However, Hartree-Fock theory does not account for correlation effects. In practical use, Hartree-Fock tends to overestimate the band gap in semiconductors significantly, thus the concept of mixing the Hartree-Fock exchange with that of DFT. The amount of mixing used is often tuned to the material to yield accurate calculations for the lattice constant and the band gap. In my work, I have primarily used the Heyd-Scuseria-Ernzerhof (HSE) functional [16, 17], which mixes 25% of the Hartree-Fock exchange with 75% of the PBE XC functional at short range.

There are also post-processing methods that can be used to correct the band gap of a DFT calculation. Most common among them is many-body perturbation theory in the GW approximation, which uses the Green's function G and the screened Coulomb interaction W to correct the self-energy. This method was not used in this work, but was used by others in works that will be discussed in Chapter 4.

1.3 Computational framework

To implement density functional theory, further simplifications and approximations have to be made. A crystal is periodic in space, meaning we do not need to calculate the

wavefunctions for each electron in the crystal. We can calculate the electronic structure for a single repeating unit and apply periodic boundary conditions.

The smallest repeating unit in a crystal structure is called the primitive unit cell. The size and shape of the primitive unit cell depend on the symmetries present in the crystal. Translational symmetry determines the Bravais lattice, while symmetries that leave at least one point fixed (reflections, rotations, etc.) make up the point group. For example, the wurtzite crystal structure has a hexagonal lattice and point group 6mm, which indicates it has 6-fold rotational symmetry along one axis, and two planes of reflection.

For a crystal with translational symmetry, a lattice vector $\mathbf{R}$ is any vector that translates the crystal onto itself. We can then define reciprocal lattice vectors $\mathbf{K}$, which have the property $\mathbf{K} \cdot \mathbf{R} = 2\pi n$, where $\mathbf{R}$ is a lattice vector and n is any integer.

The solutions to the system under periodic boundary conditions are Bloch wavefunctions $\psi_n(\mathbf{k}, \mathbf{r}) = e^{i\mathbf{k}\cdot\mathbf{r}} u_{n,\mathbf{k}}(\mathbf{r})$, which consist of a periodic function $u_{n,\mathbf{k}}(\mathbf{r})$ with the same periodicity as the crystal, and an oscillating part $e^{i\mathbf{k}\cdot\mathbf{r}}$. The vector $\mathbf{k}$ is called the wavevector, while n is the band index, highlighting that there are multiple solutions for each $\mathbf{k}$. The associated energies for these wavefunctions are continuous as a function of $\mathbf{k}$.

Further, for any reciprocal lattice vector $\mathbf{K}$, we find that $\psi(\mathbf{k}+\mathbf{K}, \mathbf{r}) = \psi(\mathbf{k}, \mathbf{r})$. This implies that we can find all the wavefunctions and eigenenergies associated to a problem by only examining a limited range of wavevectors $\mathbf{k}$. The set of all such $\mathbf{k}$ points that are closer to the origin than to any other value of $\mathbf{K}$ is called the first Brillouin zone. Integrations over all the electrons in the system are often performed as integrals of $\mathbf{k}$ over the first Brillouin zone. When we plot energies for the electrons in the crystal, we will do so at key values of $\mathbf{k}$ within the first Brillouin zone.

To calculate the Bloch wavefunctions, we use plane wave basis functions $f = e^{i\mathbf{K}\cdot r}$ that satisfy the periodicity of the lattice. Calculations on plane waves are convenient

as they can be constructed to have the same periodicity as the lattice. Further, they also give a convenient convergence test for our calculations: we can limit our calculation to the set of basis functions to $\frac{\hbar^2|\mathbf{K}^2|}{2m_e} < E$, which limits the maximum energy of the functions. Once the eigenenergies do not vary significantly with a change in E, we can be satisfied our results are converged.

However, using plane wave basis functions is challenging when the potential varies strongly with position, such as near the nucleus (where U diverges as $1/r$). Here the solution is to use pseudopotentials. Pseudopotentials treat the electrons that are localized near the nucleus and largely unaffected by other atoms as *core* electrons. These electrons are not explicitly evaluated and combined with the nucleus into an ionic core. The *valence* electrons, which do interact with other atoms, are treated selfconsistently, but the removal of the core electrons allows eliminating the strong oscillations in the wavefunctions in the vicinity of the nucleus. The pseudopotentials I use my calculations are projector-augmented-wave (PAW) pseudopotentials, which include information about the core states and allow reconstructing an all-electron wavefunction.

1.3.1 Point defects

Defects determine the electronic properties of a semiconductor. We aim to determine the concentration and nature of point defects in the system [6]. In order to examine the properties of a single defect within periodic boundary conditions, we use a supercell approach. A supercell consists of multiple copies of the primitive cell. For example, for $ZnGeN_2$, we use a $2 \times 2 \times 2$ unit cell consisting of 128 atoms. The supercell spaces the defects in all three dimensions, limiting defect-defect interactions. We define the

formation energy of a defect as:

$$E^f(D^q) = E_{\text{tot}}(D^q) - E_{\text{tot}}(\text{bulk}) + \sum_i n_i \mu_i + q\epsilon_{\text{F}} + \Delta^q \ , \tag{1.8}$$

where $E_{\text{tot}}(D^q)$ is the total energy of the supercell with the defect in charge state q. $E_{\text{tot}}(\text{bulk})$ is the total energy of the pristine supercell structure. μ_i is the chemical potential of the atoms added to ($n_i < 0$) or removed from ($n_i > 0$) to form the defect. ϵ_{F} is the Fermi energy, referenced to the VBM. Δ^q is an electrostatic correction to the energy that accounts for interactions of the charged defect with its periodic images and with the neutralizing background charge [18, 19].

In equilibrium, the concentration of point defects follows a Boltzmann distribution:

$$c = N_{\text{sites}} e^{\frac{-E^f}{k_{\text{B}}T}} \ , \tag{1.9}$$

where N_{sites} is the concentration of available sites for the defect to form, k_{B} is the Boltzmann constant, and T is the temperature. Because of the exponential factor, the defects with the lowest formation energies will have concentrations orders of magnitude larger than those with higher formation energies. For this reason, we focus our work on identifying the defects with the lowest formation energy.

For charged defects, we plot the formation energy as a function of the Fermi level in the system. The Fermi level is determined by charge neutrality. In equilibrium, the total number of positive and negative charges in the system is zero. These charges can be positively charged donors, negatively charged acceptors, free holes in the valence band, and free electrons in the conduction band. We use our formation-energy diagrams to determine the concentration of these charges.

1.3.2 Band alignments

In order to determine band alignments, we first calculate the bulk electronic structure for each material. The eigenvalues that determine the band structure are referenced to the average electrostatic potential. In a bulk calculation, this average electrostatic potential is arbitrary (and commonly set to zero), and hence cannot serve to align different materials. We can align the bulk electrostatic potential to the vacuum level by performing a surface calculation, using a geometry in which a slab of material is surrounded by vacuum. By taking a macroscopic average [20], we can compare the average electrostatic potential within the slab to the electrostatic potential in vacuum. We can then use this value to align the bulk band structure to the vacuum level.

Another way to calculate alignments between different materials is based on using the charge-state transition level of an interstitial hydrogen impurity (H_i) as a common reference [21]. The $(+/-)$ charge-state transition level for interstitial hydrogen, which we will label $H_i(+/-)$, is defined as the Fermi level (referenced to the VBM) at which H_i has the same formation energy in the $+$ and $-$ charge states [6]. These formation energies are calculated using our supercell methodology discussed above.

Lastly, it is also feasible to calculate band alignments using explicit superlattices between two materials. This requires selecting a lattice constant and straining one or both materials to enforce epitaxy. This method has been employed by other groups studying the Zn-IV-nitrides. We make use of superlattices in our work on ScN/GaN interfaces and briefly examine band alignments.

1.3.3 Computational details

In our calculations, we use the Vienna Ab initio Simulation Package (VASP) [22, 23], which provides pseudopotentials based on the PAW method. Our pseudopotentials treat

Zn $3d^{10}4s^2$, Si $3s^23p^2$, Ge $4s^24p^2$, Ge $5s^25p^2$, N $2s^22p^3$, Ga $4s^23p^1$ and Sc $4s^23d^1$ electrons as valence, with all other electrons treated as core electrons. We use the HSE hybrid functional. For our primitive unit cell calculations, integrations over the Brillouin zone are computed by sampling k-space with a grid of points.

1.4 Outline

In Chapter 2, I elaborate on the methodology I used for calculating bulk polarization and polarization at interfaces. In Chapter 3, I briefly examine the bulk properties of the Zn-IV-nitrides, before discussing native defects and doping in $ZnGeN_2$ and $ZnSiN_2$ in Chapters 4 through 6. I return to polarization in Chapter 7, where I also examine band alignments between the Zn-IV-nitrides and III-nitrides. I then turn to formal polarization differences at rocksalt/wurtzite heterostructures in Chapter 8.

1.5 Permissions and Attributions

1. The content of Chapters 3, 4, 5, and 6 is the result of collaboration with Zhen Zhu, Darshana Wickramaratne, and Chris G. Van de Walle, and has lead to three publications. The work on native point defects in $ZnGeN_2$ has previously appeared in the Journal of Applied Physics [24]. The work on n-type doping previously appeared in Physical Review B [25]. The work on p-type doping previously appeared in Applied Physics Letters [26].

2. The content of Chapter 7 is the result of collaboration with Darshana Wickramaratne and Chris G. Van de Walle. It has previously appeared in the Journal of Materials Chemistry C [27].

3. The content of Chapter 8 is the result of collaboration with Cyrus E. Dreyer and Chris G. Van de Walle. It has previously appeared in Applied Physics Letters [28].

Chapter 2

Methodology for calculating polarization

2.1 The modern theory of polarization

The polarization is an intensive vector quantity that expresses the electric dipole moments per unit volume in a material. In the simple Clausius-Mossotti model, this value is defined as the sum of the dipole moments in a given cell, divided by the cell volume [29]. However, in infinite crystals with periodic boundary conditions, there is no unique fashion by which to partition the charges in the system. This is particularly clear for covalent crystals, where the charge is delocalized and the charge density is continuous throughout the cell: defining an associated center of charge (and therefore dipole moment) is arbitrary. The Clausius-Mossotti model is therefore insufficient. As a result, polarization is defined based on the flow of polarization currents between an initial and final state:

$$\Delta\mathbf{P} = \int_0^1 d\lambda \frac{d\mathbf{P}}{d\lambda} \ . \tag{2.1}$$

Here $\lambda = 0$ and $\lambda = 1$ correspond to initial and final states of the system. Defining polarization as an integral requires selecting an appropriate constant of integration; however most properties of interest (e.g., piezoelectricity or pyroelectricity) are derivatives of the polarization. In Eq. (2.1) $d\lambda$ could be a strain, or a change in temperature, and in each case $\frac{d\mathbf{P}}{d\lambda}$ is a well-defined bulk vector property that corresponds to a physical observable.

Selecting an appropriate constant of integration is still necessary when considering polarization differences between two structures or materials, such as for the ferroelectric effect (two structures of the same material) and for heterostructures (two different materials). Resta and Vanderbilt define the spontaneous polarization as the *effective polarization* [29]

$$\Delta\mathbf{P}_{\text{eff}} = \int_0^1 d\lambda \frac{d\mathbf{P}}{d\lambda} \ , \tag{2.2}$$

where $\lambda = 0$ corresponds to the centrosymmetric reference. In this equation, λ is an adiabatic deformation that maps the crystal structure of interest ($\lambda = 1$) to a crystal structure belonging to a higher symmetry structure that has centrosymmetric symmetry. This mapping explicitly sets the constant of integration equal to the polarization of the centrosymmetric structure, which, as we will see later, is not necessarily zero. It is also important to note that the material must be insulating throughout the deformation in order to uniquely define the current $\frac{d\mathbf{P}}{d\lambda}$.

To calculate the polarization, we make use of the Berry phase. This methodology for computing the contribution from electron wavefunctions is explained in Refs. [29, 30, 31, 32]. An adiabatic perturbation λ is applied to the Bloch wavefunctions, yielding a first-order correction in the wave functions. From the perturbed wavefunctions, a total polarization current can be defined. The total change in polarization due to a single band

is determined to be

$$\frac{d\mathbf{P}_n}{d\lambda} = \int dk \, \langle \nabla_{\mathbf{k}} u_{n\mathbf{k}} | \partial_\lambda u_{n\mathbf{k}} \rangle + \text{complex conjugate} \ . \tag{2.3}$$

Integrating over λ and summing over all bands n, the polarization as a result of all the electrons is:

$$\mathbf{P}_{\text{el}} = \frac{-ie}{(2\pi)^3} \sum_n \int dk \, \langle u_{n\mathbf{k}} | \nabla_{\mathbf{k}} | u_{n\mathbf{k}} \rangle \ . \tag{2.4}$$

The contribution from ions is more straightforward:

$$\mathbf{P}_{\text{ion}} = \frac{e}{\Omega} \sum_j Z_j \mathbf{R}_j \ , \tag{2.5}$$

where Z_j is the charge on ion j, $\mathbf{R}_j$ are the coordinates of each ion in the system, and Ω is the volume of the primitive unit cell. The total *formal polarization* is therefore:

$$\mathbf{P}_{\text{f}} = \frac{e}{\Omega} \sum_j Z_j \mathbf{R}_j - \frac{ie}{(2\pi)^3} \sum_n \int dk \, \langle u_{n\mathbf{k}} | \nabla_{\mathbf{k}} | u_{n\mathbf{k}} \rangle \ . \tag{2.6}$$

It is this quantity which is central to our discussion of polarization.

A consequence of the definition above is that the formal polarization of a material is defined only modulo the "quantum of polarization" $e\mathbf{R}/\Omega$, where $\mathbf{R}$ is any lattice vector. This multivalued vector (which leads to different "branches" in $\mathbf{P}_{\text{f}}$) must map onto itself under the symmetry operations of the crystal [29]. This means that a crystal that has a center of symmetry does not need to have a formal polarization branch at zero. An example is rocksalt symmetry, where there are two distinct sets of vectors that satisfy all the symmetry operations: the formal polarization can be written as $\frac{e}{\Omega}\mathbf{R}$ or $\frac{e}{\Omega}[\mathbf{R} + a_{\text{rs}}(\frac{1}{2}, \frac{1}{2}, \frac{1}{2})]$, where a_{rs} is the rocksalt lattice parameter. Since the formal polarization itself is multi-valued, it is only differences in formal polarizations that are

physically meaningful.

To determine the polarization difference at an interface between two materials, we use the interface theorem [31]: if an insulating interface can be constructed between the two structures, the bound charge at the interface can be determined from the differences in the formal polarization:

$$\sigma_{\mathrm{b}} = (\mathbf{P}_{\mathrm{f}}^{\mathrm{A}} - \mathbf{P}_{\mathrm{f}}^{\mathrm{B}}) \cdot \hat{n} \ . \tag{2.7}$$

The formal polarizations are only defined modulo a quantum of polarization, as discussed above. Specifically, Eq. (2.7) is modulo e/A_{int} [31], where A_{int} is the unit cell area of the interface. To resolve the ambiguity, we need to select a specific branch of the formal polarization for each material. We will do this by choosing a reference structure for each of the two materials that allows connecting them at the specific interface under study.

2.2 Calculating bulk polarization

In this section I go into detail the process I used for calculating bulk polarization properties and how I determined the proper branch alignments between materials.

To calculate bulk polarization, I used the VASP program. Starting from a fully relaxed primitive unit cell, the tag LCALCPOL can be used to call for a calculation of the dipole in the cell using the Berry phase approach. This code will output two (or three, if spin polarization is applied) lines, listing an electronic dipole and an ionic dipole for the unit cell. Each of these values is only well-defined modulo $e\mathbf{R}/\Omega$, where $\mathbf{R}$ is any lattice vector.

Both the ionic and electronic contributions are calculated referenced to the center of the unit cell. Calculating with respect to the same origin is critical for the total polarization to be meaningful. However, I have found that, due to an error in VASP, the

ionic contribution can be incorrect if there are atoms very near the origin. This issue is particularly problematic for materials like the perovskites, which place an atom exactly at the origin. To fix this, the origin for the ionic calculation can be set with the DIPOL tag. The ionic contribution is linear in the position of the origin, and periodic with period $\mathbf{R}/N_{elec}$, where $\mathbf{R}$ is any lattice vector, and N_{elec} is the total number of electrons in the system (which, in a neutral system, equals the total ionic charge in the system). As a result, the origin for the ionic calculation can be shifted from the electronic origin, so long as the ionic contribution is at an equivalent point under the periodicity. I tend to pick the point (1/4, 1/4, 1/4) when the original origin does not work, as the total number of electrons in the system for a typical semiconductor is usually divisible by 4 (but this point may not work for all possible POTCARs).

Once a branch of the formal polarization has been determined, it is useful to apply modular arithmetic to select a branch that is more conventional. Doing so can also highlight any errors that have occurred. For instance, in the wurtzite material system, it is practical to select a branch that points along the c axis; if there is no branch along the c axis, then an error in calculation is likely. This error could be related to the issue with the origin for the ionic calculation described above, or it could be related to the electronic contribution. I have observed that even starting from a converged WAVECAR, it is possible the electronic dipole moment will not be calculated properly the first time. Simply restarting the calculation fixes this issue.

For materials without a center of symmetry, it is useful to define the effective polarization [29] following Eq. (2.2). This can be done by first identifying a reference structure belonging to a higher symmetry supergroup with centrosymmetry, and then constructing a sequence of structures along the deformation path between the structure of interest and the high symmetry structure. Formal polarization is then calculated for each of the structures along this path. As long as all the structures along the path are insulating, then

an adiabatic deformation exists between the two structures, and an effective polarization can be defined. However, the formal polarization of the centrosymmetric structure is not necessarily zero, and this can cause issues for calculating polarization for materials with different reference structures.

Because formal polarization is multivalued, we need to ensure that we compare the same branch of the polarization for both structures. This is accomplished by calculating the formal polarization of structures interpolated between the end points such that the differences in formal polarization are significantly smaller than the quantum of polarization $\frac{ec}{\Omega}$. In Fig. 2.1, the case for $ZnGeN_2$ is plotted between the stable $Pna2_1$ structure and the high-symmetry $Pnma$ structure. Inserts show the unit cells for the orthorhombic $Pna2_1$ structure and the centrosymmetric $Pnma$ structure of $ZnGeN_2$.

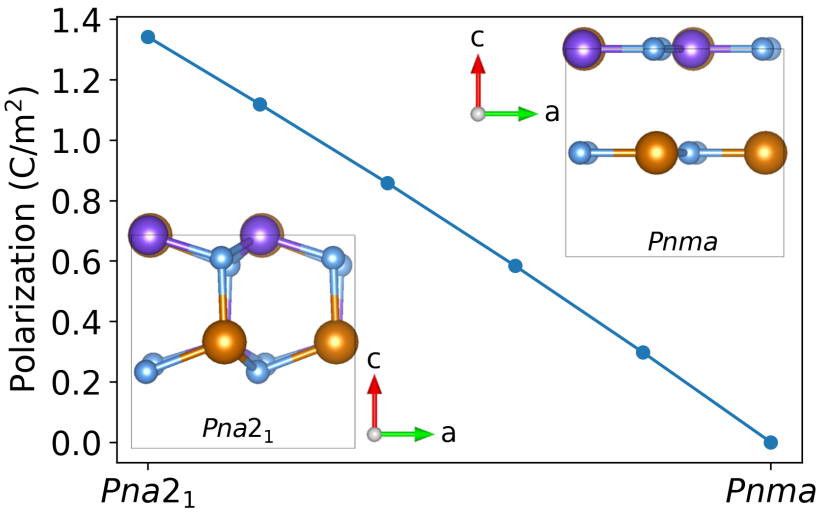

Figure 2.1: Spontaneous polarization as a function of interpolated atomic coordinates between the orthorhombic $Pna2_1$ structure and the high-symmetry $Pnma$ structure of $ZnGeN_2$.

2.3 Calculating polarization at interfaces

To calculate polarization between two dissimilar materials, we must invoke the interface theorem [Eq. (2.7)]. In principle, from the interface theorem, only the formal polarization of the two materials is necessary to determine the charge accumulation at their interface; however, in practice, the ambiguity with respect to the polarization branch complicates this issue. To unambiguously determine the polarization charge we must, in general, explicitly evaluate the electronic properties (such as internal electric fields) of the interface.

Implicit in this construction is the fact the materials can be epitaxially aligned. In the plane of the interface, there will be a periodicity common to both materials. The area of the smallest repeating unit is A_{int}. It is also practical to define $R_{\text{P}_i} = \Omega_i / A_{\text{int}}$ for each material i, which is the magnitude of the periodicity along the axis normal to the interface. The polarization normal to the interface is defined up to the quantum of polarization $\frac{eR_{\text{P}_i}}{\Omega} = e/A_{\text{int}}$.

For classes of materials with structural similarities, shortcuts may be available such that a superlattice calculation is not needed. For instance, to calculate the polarization between wurtzite materials with hexagonal reference structures [33], we can imagine superlattices involving the reference structures instead. A superlattice between hexagonal GaN and hexagonal InN along the c axis can be constructed with centers of symmetry at the center of each of the GaN and InN layers. Without doing any calculations, this immediately implies that there cannot be a field within each layer, and therefore that there cannot be charge accumulation at the interface. This aligns the branches of the polarization for the reference structures for InN and GaN, and polarization charges at interfaces between the actual wurtzite structures can then be calculated by taking a difference between their effective polarizations.

However, for crystal structures that are very different, such a shortcut cannot be made. Consider polarization differences between the rocksalt structure along [111] and the wurtzite structure along [0001]. The rocksalt structure is centrosymmetic; however it is difficult to align the polarization of the rocksalt structure to that of the hexagonal reference structure. It is not possible to construct a superlattice between the two centrosymmetric structures that contains a center of symmetry. Therefore, performing a superlattice calculation is necessary.

The superlattice, with basal area A_{int}, should be constructed with layers of each material thick enough such that we can define a bulk region sufficiently far away from any interface relaxations. A self-consistent calculation of the electronic states of the superlattice should be performed. If the superlattice is insulating, then the electric fields within each material can be calculated and the bound charge at the interface can be determined, which provides the branch alignment between the formal polarization of the materials. To calculate the electric fields, the planar average of the electrostatic potential is calculated throughout the superlattice. I then convolve the planar average with a rectangle function of length R_{P} in each material to remove any oscillations and get the averaged electrostatic potential as a function of the distance from the interface. The electric fields are the slope of this function in each of the respective bulk regions. In Fig. 2.2, I plot the averaged electrostatic potential for a superlattice between eight layers of hexagonal GaN and eight layers of layered ScN. The electric fields are taken from the slopes over the bulk regions.

If the polarization difference between the two materials is too large, there is a chance that the material will undergo breakdown, and free carriers will move to screen the electric fields. As a result, the difference in calculated electric fields will not correspond to the full polarization charge at the interface. Instead, if we can define an insulating superlattice of alternative structures of the materials with smaller internal electric fields,

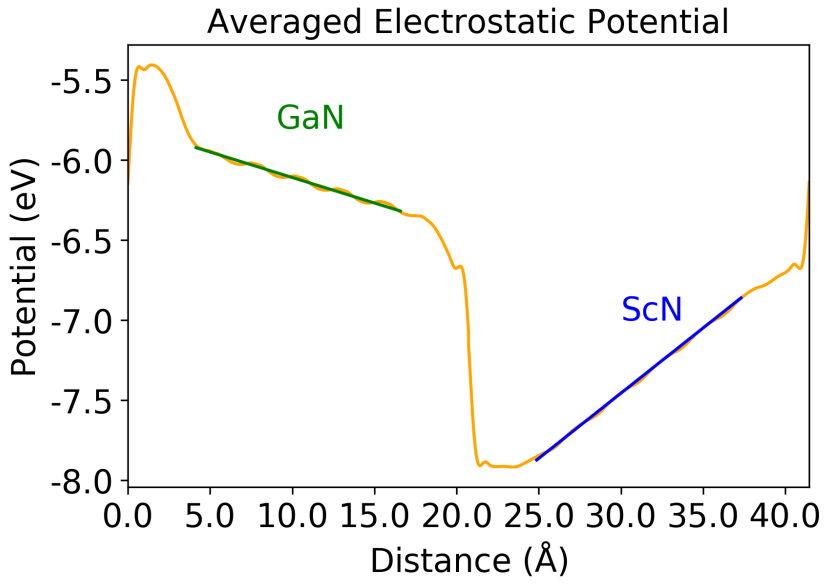

Figure 2.2: Smoothed planar average of the electrostatic potential in a superlattice consisting of hexagonal GaN and layered ScN. Bulk regions for each material are indicated.

we can use that superlattice to make the correct choice of branch.

We observe in calculations for the wurtzite materials system that the effective polarization scales approximately linearly with the separation of planes of cations and anions along the polar axis. Therefore, it is reasonable to assume materials with similar separation between planes of cations and anions will exhibit smaller polarization differences. For the rocksalt structure, that is indeed what we observe.

To determine the polarization difference between rocksalt ScN and wurtzite GaN, the simplest choice of superlattice with small electric fields is to place anions and cations into the same planes. As a result, each layer will be electrically neutral. For wurtzite this creates the higher symmetry hexagonal structure that was already used as a reference structure. For rocksalt, this results in a lower symmetry structure which I refer to as 'layered-ScN'.

Once the electric fields are determined in each region, the bound charge at the inter-

face can be calculated by Gauss's law. The electric displacement field is discontinuous across the interface, and the discontinuity is equal to the polarization difference:

$$\sigma_b = \varepsilon_0 \varepsilon_r^{\mathrm{A}} \mathcal{E}_{\mathrm{A}} - \varepsilon_0 \varepsilon_r^{\mathrm{B}} \mathcal{E}_{\mathrm{B}} \ , \tag{2.8}$$

where $\mathcal{E}$ is the electric field in each material, ε_0 is the permittivity of free space, and ε_r is the relative permittivity. This value can then be compared to the bulk polarization values in each material, and the correct branch alignment can be selected. Since ionic positions are kept fixed in this calculation (the ionic coordinates are prevented from moving, or the ions have previously been allowed to relax), only electrons are able to screen the charge, the dielectric constant chosen should be the clamped-ion dielectric constant.

Once the alignment between any two crystal structures of materials is known precisely, adiabatic transformations can be performed on each material separately to determine the correct polarization discontinuity between materials of interest. For example, the polarization discontinuity between layered ScN and hexagonal GaN can be determined unambiguously from the electrostatic potential plotted in Fig. 2.2. The polarization difference between rocksalt ScN and layered ScN can be determined from an adiabatic transformation analogous to Fig. 2.1, as can the difference between hexagonal GaN and wurtzite GaN. These differences can all be summed to give the polarization difference between rocksalt ScN and wurtzite GaN.

2.4 Piezoelectricity

Piezoelectric materials are materials that produce a current when a mechanical strain is applied. The proper piezoelectric tensor (which is the one that is commonly cited in literature) describes the relation between the strain rate applied to the system and the

resulting current density in a *closed circuit*, given by

$$e_{ijk}^{\text{prop}} = \frac{dJ_i}{d\dot{\epsilon}_{jk}} \ . \tag{2.9}$$

Here J_i is the current density along direction i, and $\dot{\epsilon}_{jk}$ is the time derivative of a strain ϵ_{jk} applied to the system [34].

Now consider a thin layer of polar material with *open-circuit* boundary conditions [33]. The crystal will have an electric field across it due to its spontaneous polarization. If we apply a strain on the crystal, then the electric field in the crystal will be affected in two ways. The first is the same as in the proper case with the closed circuit: strain will cause a flow of polarization current. The second effect is that as the cross-sectional area of the crystal changes, the bound charge at the surfaces will be diluted or concentrated. The sum of these effects is given by the improper piezoelectric constant.

At an epitaxial interface between two semiconductors, there is typically some degree of strain, since the lattice parameters of the two materials are usually not perfectly matched. For purposes of calculating polarization differences at interfaces between two semiconductors, improper piezoelectric coefficients should be used [33, 34]. The improper piezoelectric tensor is given by:

$$e_{ijk}^{\text{imp}} = \frac{dP_i}{d\epsilon_{jk}} \ , \tag{2.10}$$

where P_i is the formal polarization along axis i, and ϵ_{jk} is the applied strain. Despite the different formulations, the proper and improper piezoelectric tensors are calculated with the same methods.

The improper piezoelectric tensor can be expanded into three terms:

$$e_{ijk}^{\text{imp}} = \left.\frac{\partial P_i}{\partial \epsilon_{jk}}\right|_{\mathbf{R},\Omega} + \sum_{\alpha,l} \frac{\partial P_i}{\partial R_{\alpha,l}} \frac{dR_{\alpha,l}}{d\epsilon_{jk}} - \delta_{jk} P_i + \delta_{ij} P_k \ . \tag{2.11}$$

Here, $R_{\alpha,l}$ is the l^{th} fractional coordinate of atom α and δ is the Kronecker delta. The first term fixes all the internal coordinates and the volume of the cell, and is referred to as the clamped-ion term. This term depends entirely on the electron wavefunctions, and corresponds to the degree to which electrons fail to follow a homogeneous deformation under applied strain [34]. The second term accounts for the changes in atomic coordinates as a function of strain. These first two terms make up the proper piezoelectric response, which is independent of the choice of branch and hence is not subject to the ambiguity associated with the modulo of polarization [34]. The improper and proper piezoelectric tensors are related by the last two terms, given by Kronecker deltas of two indices multiplied by the branch-dependent formal polarization along the third axis [34]. These terms describe the effect of diluting or concentrating the bound charge under open circuit boundary conditions.

The number of nonzero piezoelectric constants in the proper piezoelectric response is determined by the symmetry of the crystal. For the wurtzite structure, using Voigt notation, only $e_{31}^{\text{prop}}, e_{32}^{\text{prop}}, e_{33}^{\text{prop}}, e_{24}^{\text{prop}}$, and e_{15}^{prop} are nonzero. Of these, $e_{31}^{\text{prop}} = e_{32}^{\text{prop}}$ and $e_{24}^{\text{prop}} = e_{15}^{\text{prop}}$ by symmetry. For the orthorhombic structure of the Zn-IV-nitrides, the same selection of constants are nonzero, but the symmetries between e_{31}^{prop} and e_{32}^{prop} and between e_{24}^{prop} and e_{15}^{prop} are broken. For the centrosymmetric rocksalt structure, all proper piezoelectric tensor values are zero.

Each of the terms in Eq. (2.11) is calculated separately. VASP calculates the clamped-ion piezoelectric tensor by making use of the converse piezoelectric effect [35]: the derivative of the polarization with respect to strain is equal to negative of the derivative of stress with respect to electric field. VASP applies a small electric field and calculates the clamped-ion piezoelectric effect without applying any strain.

For the internal-strain term, it is convenient to invoke the Born effective charge, which

describes how the polarization changes as a function of an atomic coordinate:

$$Z^*_{\alpha,il} = \frac{\Omega}{ea_l}\frac{dP_i}{dR_{\alpha,l}} \ , \tag{2.12}$$

where a_l is the l^{th} lattice parameter. The internal strain term can then be written as

$$e^{\text{int}}_{ijk} = \frac{e}{\Omega}\sum_{\alpha,l} a_l Z^*_{\alpha,il}\frac{dR_{\alpha,l}}{d\epsilon_{jk}} \ . \tag{2.13}$$

The changes in fractional coordinates can be computed directly in response to an applied strain, while the Born effective charges are computed by VASP as a response to an applied electric field.

The last portion of Eq. (2.11), $-\delta_{jk}P_i + \delta_{ij}P_k$ is unique in that it is branch dependent [34]. This term can be thought of as the effect of diluting or concentrating the polarization into a larger or smaller area. In the wurtzite nitrides, the value of this term is $-P_3$ for e^{imp}_{31} and e^{imp}_{32}, and zero for all other piezoelectric elements.

By summing all of the terms in Eq. (2.11), we get the full piezoelectric response which can be added to the spontaneous polarization to give the total polarization of each material.

2.5 Polarization of alloys

Finally, we comment on how polarization of alloys should be handled. In most of the literature, spontaneous polarization values for ternary alloys (in units of C/m^2) have been obtained by linear interpolation between the values for the binaries. I will show that there is a more accurate way of performing this interpolation. We take as our central assumption Vegard's law, which states that the lattice parameters scale linearly

	$P_{\text{eff,lin}}$ (C/m^2)	A_{int} (Å^2)	P_r	$P_{\text{eff,alloy}}$ (C/m^2)
AlN	1.346	8.34	0.702	–
GaN	1.315	8.88	0.730	–
InN	1.038	11.05	0.717	–
$Al_{0.5}Ga_{0.5}N$	1.331	8.61*	0.716	1.330*
$Al_{0.5}In_{0.5}N$	1.192	9.65*	0.710	1.175*
$In_{0.5}Ga_{0.5}N$	1.177	9.93*	0.724	1.165*

Table 2.1: Polarization parameters for AlN, GaN, and InN, along with ternaries $Al_{0.5}Ga_{0.5}N$, $Al_{0.5}In_{0.5}N$, and $In_{0.5}Ga_{0.5}N$. The symbol * indicates the parameter correctly accounts for the nonlinear dependence on the alloy concentration. All values were calculated using the HSE hybrid functional with 25% mixing.

with alloy content. The polarization is a dipole per unit volume. The dipole (defined as charge times displacement) scales approximately as lattice parameter to the first power, while the volume scales as lattice parameter to the third power. The quotient therefore scales as lattice parameter to the power of –2. As a result, the polarization should not be linearly interpolated as a function of alloy content.

Instead, we should factor out all spatial dependence and work with the polarization in dimensionless units. Then the polarization can be linearly interpolated as a function of alloy content properly.

As an example, let us consider the formal polarization of the wurtzite system. Here, I write the polarization P_r in dimensionless units:

$$P_{\text{eff}} = \frac{e}{A_{\text{int}}} P_r \ . \tag{2.14}$$

In Table 2.1, we list all of the values for AlN, GaN, and InN, along with their ternaries at 50% composition. The first value, $P_{\text{eff,lin}}$, is the effective polarization of the alloy using linear interpolation, while $P_{\text{eff,alloy}}$ is the corrected effective polarization, by linearly interpolating in units of e/A_{int} before converting back.

The values using both types of interpolation are provided in Table 2.1. For $Al_{0.5}Ga_{0.5}N$, linear interpolation of the polarization gives 1.331 C/m^2, while interpolation in dimensionless units gives 1.330 C/m^2. The difference is not large in this case. For the alloys including In, the difference is much more significant because the difference in lattice constant is much larger. These differences on the order of 0.01-0.02 C/m^2 may seem small, but correspond to interfacial charge differences on the order of 1×10^{13} cm^{-2}. We will see in Chapter 7 that these interfacial charges directly impact the carrier density of two-dimensional electron gases at these interfaces. We thus see that a more correct way of performing interpolation for alloys can have a noticeable impact on quantities obtained in device modeling.

The effect described here is not the same as the nonlinearity observed by Bernardini and Fiorentini [36]. They perform calculations on explicit alloys and observe variations in the polarization as a result of microscopic alloy structure. Further, they use zinc-blende as their reference structure. While issues with the zinc-blende reference were pointed out in Ref. [33], calculations referenced to zinc-blende are not as susceptible to errors from using linear interpolation. This is because the formal polarization of zinc-blende reference already depends on the lattice constant to the power of –2, and the error in the difference $P_{\mathrm{f}} - P_{\mathrm{zb}}$ is only about 0.001 C/m^2.

Chapter 3

The Zn-IV-nitrides

This work was done in collaboration with Darshana Wickramaratne, Zhen Zhu, and Chris G. Van de Walle.

3.1 Introduction

The Zn-IV-nitrides are a group of semiconductors with wide band gaps and other properties that make them promising candidates for a variety of electronic and optoelectronic devices [5]. Taking advantage of the small lattice mismatch between Zn-IV-nitrides and the III-nitrides, a variety of device applications have been proposed based on heterostructures involving both sets of materials [37, 38, 39]. The success of these applications depends on accurate knowledge of the bulk physical electronic structure.

II-IV-V_2 compounds have been studied since the 1960s [40]. $ZnGeN_2$ was first synthesized in the early 1970s [41, 42], followed by synthesis of $ZnSiN_2$ [43, 44]. In the last decade we have seen a surge of interest in these materials, particularly in $ZnSnN_2$ [45] and $ZnGeN_2$ [46] and their application to optical devices.

Our focus in this chapter is to introduce the Zn-IV-nitrides, their physical and elec-

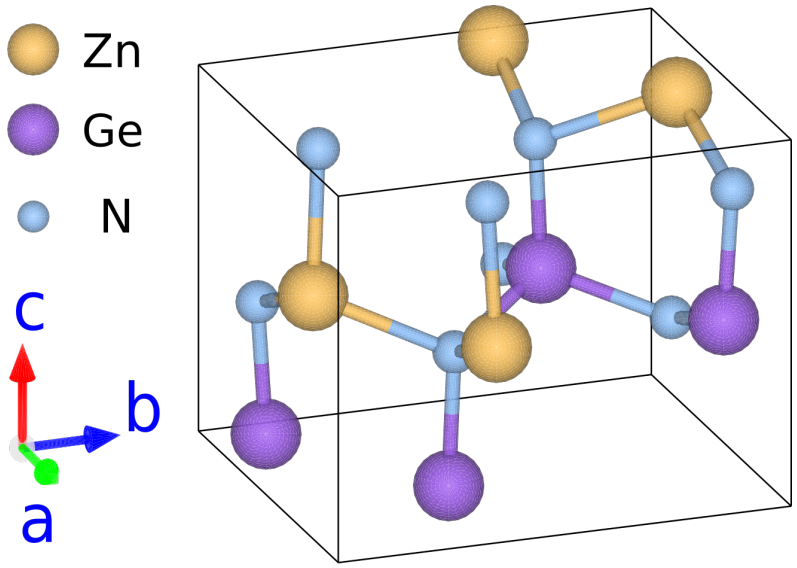

Figure 3.1: Unit cell of $ZnGeN_2$ in the orthorhombic $Pna2_1$ phase.

trical structure, and explore where they fit with respect to other nitride semicondcutors. In Chapters 5 and 6, we will investigate doping, while in Chapter 7 we will examine heterostructures between Zn-IV-nitrides and III-nitrides, including band alignments and polarization effects.

3.2 Physical structure

The structure of the Zn-IV-nitrides ($ZnSnN_2$, $ZnGeN_2$, and $ZnSiN_2$) can be envisioned as starting from, e.g., GaN in the wurtzite (wz) structure and replacing pairs of Ga atoms with Zn-(group-IV) pairs. This lowers the symmetry of the crystal, and as a result the Zn-IV-nitrides have an orthorhombic lattice with a 16-atom unit cell. The lattice parameters of the orthorhombic cell can be related to those of the wz cell via the relations: $a \approx \sqrt{3}a_{\mathrm{wz}}$, $b \approx 2a_{\mathrm{wz}}$, and $c \approx c_{\mathrm{wz}}$, where a_{wz} and c_{wz} are the wz lattice parameters. In Fig. 3.1, we illustrate the $ZnGeN_2$ primitive cell.

The space group for this structure is $Pna2_1$, which imposes an ordering on the cation

sublattice. There are two glide plane symmetries: one perpendicular to the a axis, and one perpendicular to the b axis; as a result, polarization is zero along these directions. Similar to the wz structure, the spontaneous polarization points along the c axis.

Our calculations are performed using the HSE functional (See Sec. 1.3) and a plane-wave energy cutoff of 500 eV. We use the default mixing parameter of 25%. For integrations over the Brillouin zone, we use a Monkhorst-Pack [47] $4 \times 4 \times 4$ k-point grid.

In Table 3.1, we list the calculated lattice parameters for the Zn-IV-nitrides relative to values reported in the literature. Very good agreement is observed. In the same table, we also include the lattice parameters for the III-nitrides. The lattice parameters can be compared using the relations listed above. In Fig. 3.2, we plot the lattice parameters of the Zn-IV-nitrides and III-nitrides on the same figure using wurtzite-equivalent lattice parameters $a/\sqrt{3}$ and $b/2$. $a/\sqrt{3}$ is smaller than $b/2$ for each of the nitrides. For $ZnSiN_2$, there is a large difference between the two values, but this difference is smaller for $ZnGeN_2$ and extremely small for $ZnSnN_2$. This effect can be explained by the ionic radii differences between Zn and each of the group-IV cations. The Zn^{2+} ion has a radius of 0.60 Å, while Si^{4+} has an ionic radius of 0.26 Å, Ge^{4+} 0.39 Å, and Sn^{4+} 0.55 Å. A much larger structural change is required to fit Zn and Si together than for Zn and Sn.

We find $ZnGeN_2$ has an average in-plane lattice parameter that is extremely close to that of GaN. $a/\sqrt{3}$ is about 1% smaller, while $b/2$ is about 1% larger. As a result, $ZnGeN_2$ may be grown epitxially on GaN with very low strain. For the other Zn-IV-nitrides, we find $ZnSiN_2$ has an average in-plane parameter of 3.08 Å, slightly smaller than that of AlN, while the average in-plane parameter of $ZnSnN_2$ sits between GaN and InN.

Compound	Property	Calc.	Expt.
$ZnSnN_2$	a(Å)	5.85	5.84 [48]
	b(Å)	6.74	6.75 [48]
	c(Å)	5.47	5.46 [48]
	E_g(eV)	1.40	...
$ZnGeN_2$	a(Å)	5.47	5.45 [42]
	b(Å)	6.45	6.44 [42]
	c(Å)	5.20	5.19 [42]
	E_g(eV)	3.19	...
$ZnSiN_2$	a(Å)	5.24	5.25 [49]
	b(Å)	6.27	6.28 [49]
	c(Å)	5.02	5.02 [49]
	E_g(eV)	4.83	...
InN ($\alpha = 25\%$)	a(Å)	3.59 [33]	3.55 [50]
	c(Å)	5.76[33]	5.70 [50]
	E_g(eV)	0.65[33]	0.78 [50]
GaN ($\alpha = 29.5\%$)	a(Å)	3.19	3.19 [50]
	c(Å)	5.19	5.19 [50]
	E_g(eV)	3.48	3.51 [50]
AlN ($\alpha = 31\%$)	a(Å)	3.10[33]	3.11[50]
	c(Å)	4.96[33]	4.98[50]
	E_g(eV)	6.04[33]	6.25[50]

Table 3.1: Calculated lattice parameters and band gaps for the Zn-IV-nitrides and GaN; experimental values are included for comparison. For AlN and InN, we use calculated values from Dreyer *et al.* [33].

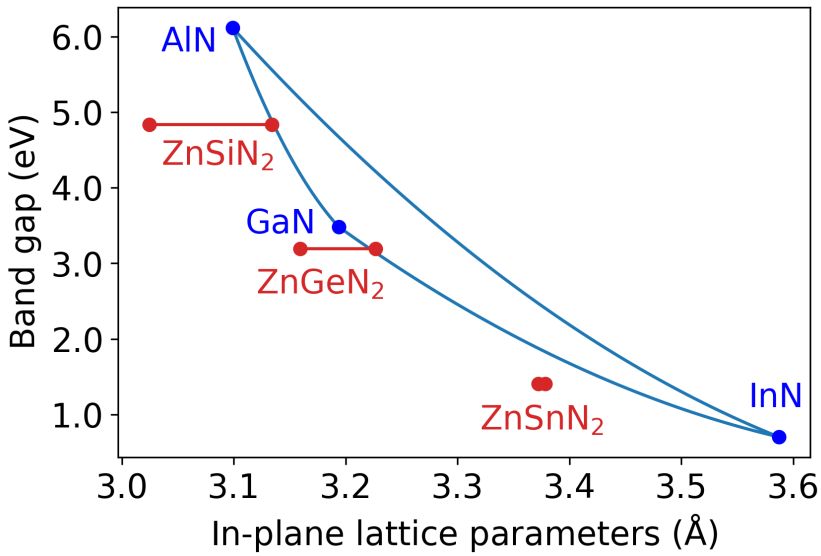

Figure 3.2: In-plane lattice parameters and band gaps for the Zn-IV-nitrides and III-nitrides. The two data points for the Zn-IV-nitride materials are the wurtzite-equivalent lattice parameters $a/\sqrt{3}$ and $b/2$.

3.3 Electronic structure

We calculate the band gaps by plotting the eigenvalues for all the electrons in the system along high-symmetry lines in the first Brillouin zone. For the orthorhombic crystal structure, the Brillouin zone is also orthorhombic; we depict the Brillouin zone in Fig. 3.3(a). For $ZnGeN_2$ and $ZnSnN_2$, we find the band gap to be direct, with both the CBM and VBM occuring at the Γ point. However, for $ZnSiN_2$, we find the band gap to be indirect, as the VBM is at the T point. A direct band gap is important for optical devices, as efficient optical absorbtion and emission requires electrons and holes to recombine at the same k-point to conserve momentum. The band gaps for each of the Zn-IV-nitrides are listed in Table 3.1. In Fig 3.2, we plot the band gaps as a function of the lattice constant, while in Fig 3.3, we plot the full bandstructure of each of the Zn-IV-nitrides.

We calculate an indirect gap for $ZnSiN_2$ of 4.83 eV and a direct gap at Γ of 5.18

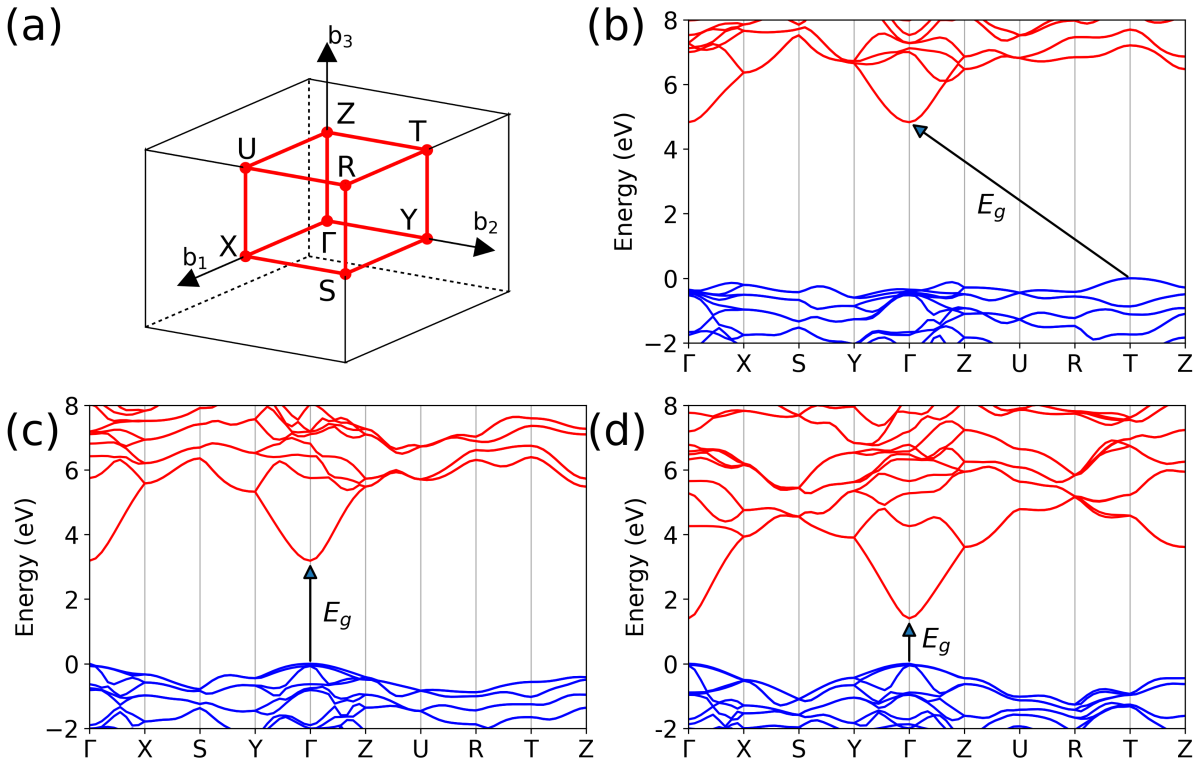

Figure 3.3: (a) The First Brillouin zone for the orthorhombic $Pna2_1$ phase. (b-d) The band structure of (b) $ZnSiN_2$, (c) $ZnGeN_2$, and (d) $ZnSnN_2$, calculated using the HSE hybrid functional.

eV. As a result, $ZnSiN_2$ cannot be used as the active region in an light-emitting device, but might still have applications as a barrier layer or in electronic devices that uniquely make use of electrons (unipolar devices). Punya *et al.* previously calculated the band structure of $ZnSiN_2$ using the quasiparticle self-consistent GW approximation [51]. They found an indirect band gap of 5.44 eV with the VBM residing between Γ and X. We find the same local maxima in the valence band but find the maximum at the T point to be higher than the local maximum between Γ and X. These differences are small, about 0.2 eV, and mostly result from small differences in the lattice parameters. Note that there is a difference in labeling of **k** points between our results and the results of Punya *et al.* as they have interchanged the a and b lattice vectors.

Previous experimental reports have determined the band gap of $ZnGeN_2$ to lie within the range of 2.99 eV to 3.3 eV [52, 53, 54], in good agreement with our calculated value of 3.19 eV. For $ZnSnN_2$, the gap has been reported in the range of 1 to 2 eV [55, 56], with uncertainties arising from significant disorder on the cation sublattice and a Burstein-Moss shift resulting from degenerate electron doping. Our $ZnSnN_2$ band gap of 1.4 eV is consistent with previous calculations [56, 57].

Due to the small lattice mismatch between GaN and $ZnGeN_2$, and the band gap of $ZnGeN_2$ lying close to the visible spectrum, the majority of our work focuses on $ZnGeN_2$. The following three chapters study point defects and n and p-type doping in $ZnGeN_2$. We also examine point defects and n-type doping in $ZnSiN_2$ for potential applications to unipolar electronics. Point defects and doping in $ZnSnN_2$ have been studied in a variety of other works [57, 58, 59]. In Chapter 6, we study heterojunctions between Zn-IV-nitrides and III-nitrides.

Chapter 4

Point defects and unintentional n-type doping in $ZnGeN_2$ and $ZnSiN_2$

The defect properties of materials significantly impact their applications in electronic and optoelectronic devices. Some defects can be beneficial, such as shallow donors and acceptors that enable the formation of *p*-*n* junctions; while other defects can be detrimental, causing compensation or leading to deep traps that increase recombination and reduce carrier mobility. In this work, we examine interstitials, vacancies, antisites, and substitutional dopants. This work was done in collaboration with Darshana Wickramaratne, Zhen Zhu, and Chris G. Van de Walle.

4.1 Introduction

Defects in semiconductors, such as vacancies, interstitials, and antisites affect the electronic properties of the material. The Zn-IV-nitrides have two cations: Zn, from

group-II, and a group-IV cation. As a result, cation-cation antisite defects can be particularly important.

Prior work on point defects and impurities in $ZnGeN_2$ was performed by Skachkov *et al.* [60] using density functional theory and the local density approximation (LDA). The LDA functional significantly understimates the band-gap, which they addressed by applying an on-site potential U to the Ge and Zn s and p states. The $LDA+U$ formalism was designed to treat highly localized states, such as d of f states [61, 62], and there is no formal justification for applying it to s and p states. In addition, while $LDA + U$ can bring the band gap into closer agreement with experiment, it does not necessarily produce the correct values for the VBM and CBM on an absolute energy scale. This can lead to deficiencies in formation energies and thermodynamic transition levels. Our work, using the HSE functional, avoids these pitfalls. Skachkov *et al.* [60] also examined O and Ga as potential dopants in $ZnGeN_2$, showing O_N acts as a shallow donor, and that Ga acts as a shallow donor on the Zn site, and a shallow acceptor on the Ge site. We found no previous defect studies on $ZnSiN_2$

Our focus in this chapter is to access the relative stability of native point defects in $ZnGeN_2$ and $ZnSiN_2$. We evaluate vacancies, interstitials, antisites, in a variety of charge states, in order to determine their electronic behavior. Furthermore, we investigate the role of oxygen and hydrogen, which may be unintentionally incorporated during growth. We find that native point defects in $ZnGeN_2$ do not lead to electrically conductive material, while both hydrogen and oxygen, substituting on the nitrogen site, act as donors in both $ZnGeN_2$ and $ZnSiN_2$.

Our point-defect calculations are performed within the VASP code, using the HSE functional with the standard mixing parameter of 25% (See Sec. 1.3). For calculations involving supercells, we use the single special k-point at (1/4, 1/4, 1/4) for integrations over the Brillouin zone. We apply spin polarization in all our calculations.

Under the formalism discussed in Sec. 1.3.1, the formation energy of a defect D in charge state q is:

$$E^f(D^q) = E_{\text{tot}}(D^q) - E_{\text{tot}}(\text{bulk}) + \sum_i n_i \mu_i + qE_F + \Delta^q \,, \tag{4.1}$$

where $E_{\text{tot}}(D^q)$ is the energy of the supercell with the defect present, $E_{\text{tot}}(\text{bulk})$ is the energy of the pristine supercell, and μ_i is the chemical potential of the atoms added to ($n_i < 0$) or removed from ($n_i > 0$) to form the defect. E_F is the Fermi energy, referenced to the VBM, and Δ^q is the Freysoldt correction [18, 19, 63].

4.2 Chemical potentials and phase stability

The chemical potentials in Eq. (4.1) act as proxy for the semiconductor growth and processing conditions. The chemical potentials for each atom are bounded by the conditions for stability in thermodynamic equilibrium. We reference these chemical potentials to the total energies, per atom, of their respective ground-state phases; for instance $\Delta\mu_{\text{Zn}} = \mu_{\text{Zn}} - \mu_{\text{Zn(bulk)}}$, where $\mu_{\text{Zn(bulk)}}$ is the per-atom energy of hexagonal close-packed Zn. Using this notation, the constraints imposed by the formation of $ZnGeN_2$ and $ZnSiN_2$ are:

$$\Delta\mu_{\text{Zn}} + \Delta\mu_{\text{Ge}} + 2\Delta\mu_{\text{N}} = \Delta H^f(\text{ZnGeN}_2) \tag{4.2}$$

and

$$\Delta\mu_{\text{Zn}} + \Delta\mu_{\text{Si}} + 2\Delta\mu_{\text{N}} = \Delta H^f(\text{ZnSiN}_2) \,, \tag{4.3}$$

where ΔH^f is the formation enthalpy. We calculate a formation enthalpy of -1.09 eV/(formula unit) (eV/f.u) for $ZnGeN_2$ and -3.71 eV/f.u for $ZnSiN_2$.

To define regions where $ZnGeN_2$ and $ZnSiN_2$ are thermodynamically stable, we also

need to take into account secondary phases that can form during growth. Ge_3N_4 is one such phase that can form during the growth of $ZnGeN_2$; the appropriate restriction to prevent formation of Ge_3N_4 is therefore:

$$3\Delta\mu_{\mathrm{Ge}} + 4\Delta\mu_{\mathrm{N}} \leq \Delta H^f(\mathrm{Ge_3N_4})\,. \tag{4.4}$$

Similar equations hold for the other secondary phases. The formation enthalpies of secondary phases that we have considered are included in Table 4.1 where they are compared to experimental values. We calculate a small positive formation enthalpy of formation for Zn_3N_2. Ge_3N_4 is the only limiting phase for $ZnGeN_2$, and Si_3N_4 is the only limiting phase for $ZnSiN_2$. We illustrate the phase diagram for $ZnGeN_2$ and $ZnSiN_2$ in Fig. 4.1. We highlight the vertices of the $ZnGeN_2$ and $ZnSiN_2$ stability regions as they will be informative choices of chemical potentials for plotting formation energies.

For the purposes of presenting formation-energy results in $ZnGeN_2$, we focus on two extreme cases: the points labeled "Zn-poor A" and "Ge-poor" in Fig. 4.1(a). "Ge-poor" is where $\Delta\mu_{\mathrm{Zn}} = 0$ and $\Delta\mu_{\mathrm{Ge}} = -1.09$ eV. "Zn-poor A" is where $\Delta\mu_{\mathrm{Zn}} = -0.71$ eV and $\Delta\mu_{\mathrm{Ge}} = 0$ eV. For $ZnSiN_2$, the conclusions do not depend on the choice of chemical potential, and we will present results only in the Zn-poor limit. Formation energies under other conditions can always be obtained by referring back to Eq. (4.1).

We also consider the chemical potential of potential dopant elements. For example, high concentration of O doping could result in growth of ZnO or GeO_2. In calculating dopant formation energies and concentrations, we are assuming that we are at the solubility limit of the dopant, where growth of these competing phases prevents further doping. The formation enthalpies of these secondary phases are also included in Table 4.1. For H, the limiting phase was taken to be H_2 gas.

Compound	Calc. (eV)	Expt. (eV)
$ZnGeN_2$	-1.09	...
$ZnSiN_2$	-3.71	...
Zn_3N_2	$+0.20$	-0.25 [64]
Ge_3N_4	-0.77	-0.64 [65]
Si_3N_4	-8.83	-8.58 [66]
Li_3N	-1.65	-1.71 [67]
AlN	-3.15	-3.30 [68]
GaN	-1.20	-1.29 [68]
ZnS	-1.88	-2.12 [69]
ZnSe	-1.73	-1.84 [69]
P_3N_5	-3.87	-3.32 [70]
Zn_3P_2	-1.28	-1.71 [71]
Zn_3As_2	-1.29	-1.34 [72]
GeAs	-0.13	...
$ZnGeAs_2$	-0.93	...
ZnO	-3.10	-3.62 [64]
GeO_2	-4.93	-5.70 [64]
SiO_2	-8.90	-9.44 [70]

Table 4.1: Formation enthalpies for $ZnGeN_2$, $ZnSiN_2$, and limiting phases.

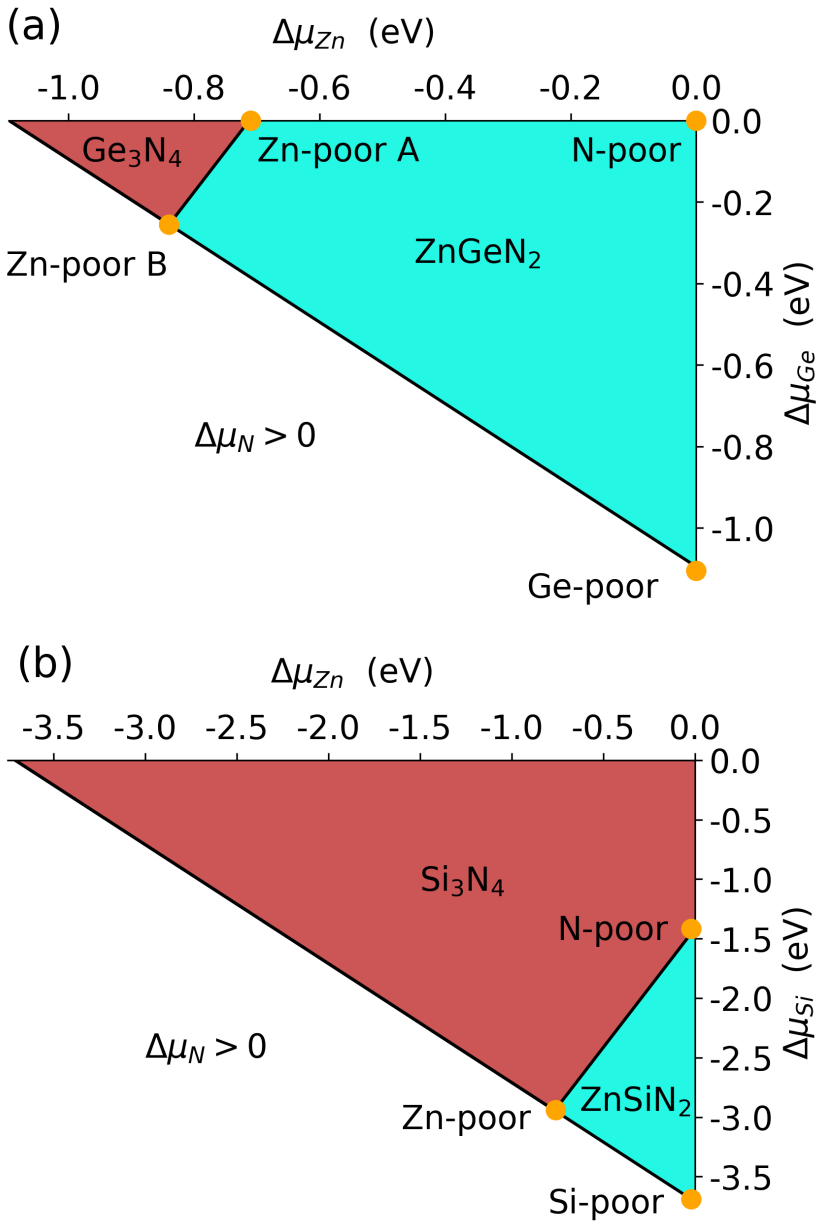

Figure 4.1: Calculated phase stability diagrams for (a) $ZnGeN_2$ and (b) $ZnSiN_2$. For any pair of $\Delta\mu_{Zn}$ and $\Delta\mu_{Ge}$ ($\Delta\mu_{Si}$), $\Delta\mu_N$ is given by Eq. (4.2) [Eq. (4.3)].

4.3 Native point defects in $ZnGeN_2$

The formation energies of all the native defects we have considered are shown in Fig. 4.2. We first consider the properties of the vacancies. We find the Ge vacancy (V_{Ge}) has a high formation energy for all values of the Fermi level under both chemical potential conditions. Hence, V_{Ge} is unlikely to form in $ZnGeN_2$ in any appreciable concentration during growth. The Zn vacancy (V_{Zn}) exhibits low formation energies under n-type conditions (Fermi level high in the gap), particularly under Zn-poor conditions. V_{Zn} is stable as a deep acceptor in the 2– charge state for Fermi levels above 1.44 eV; it would thus act as a compensating center in n-type material. The nitrogen vacancy V_{N}, on the other hand, acts as a deep donor; it is in a + charge state when the Fermi level is below the (+/0) transition level, at 0.71 eV from the CBM. V_{N} has a low formation energy, particularly when the Fermi level is low in the gap; it has a (3+/+) transition 0.22 eV from the VBM. V_{N} can also be stable in the negative charge state, with a (0/–) level 0.32 eV below the CBM.

Next, we address the properties of interstitials. The Zn interstitial (Zn_i) has a low formation energy under p-type conditions and is stable only in the 2+ charge state. The Ge interstitial (Ge_i) has high formation energy across most of the band gap and is stable as a donor in various positive charge states. The N interstitial (N_i), on the other hand, is amphoteric, exhibiting both positive and negative charge states across the $ZnGeN_2$ band gap.

Turning to cation antisites, the $\mathrm{Ge}_{\mathrm{Zn}}$ antisite is the defect with the lowest formation energies when the Fermi level is below mid gap. Ge has two more electrons than Zn and therefore $\mathrm{Ge}_{\mathrm{Zn}}$ is stable in a 2+ charge state across a majority of the $ZnGeN_2$ band gap, with a (2+/0) level at 0.20 eV below the CBM. For the $\mathrm{Ge}_{\mathrm{Zn}}$ antisite in the 2+ charge state we find a small outward relaxation of the nearest-neighbor N atoms, while in the

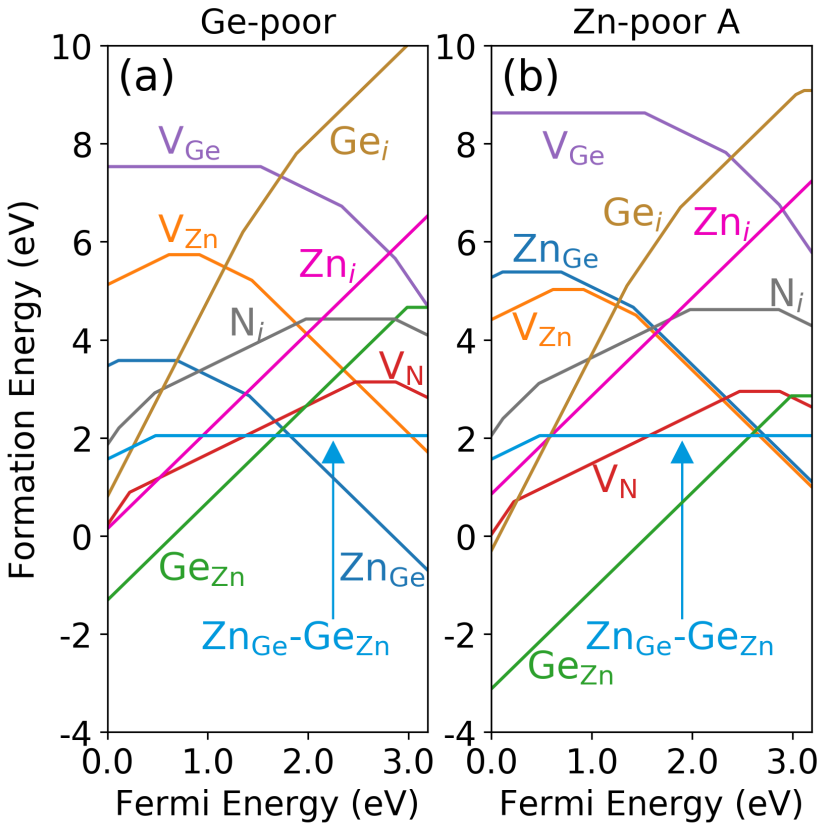

Figure 4.2: Formation energies of point defects in $ZnGeN_2$ as a function of Fermi level under (a) Ge-poor and (b) Zn-poor conditions. The slope of each line segment indicates the stable charge state of the defect at a particular Fermi level, and kinks in the curves correspond to charge-state transition levels.

neutral charge state, we find a large asymmetric displacement of the nearest-neighbor N atoms.

Since Zn has two fewer electrons than Ge, we find the Zn_{Ge} antisite to act as a double acceptor. Under Ge-poor conditions, we find Zn_{Ge} to be the lowest-energy defect under n-type conditions. In the 2– charge state of Zn_{Ge}, a small inward relaxation of the nearest-nightbor N atoms occurs. Under Zn-poor conditions, the formation energies of Zn_{Ge} and V_{Zn} (both in the 2– charge state) are comparable when the Fermi level is high in the gap.

Results for nitrogen antisites (N_{Zn} and N_{Ge}) are not included here as we found them to have very large formation energies. This can be attributed to the mismatch in atomic radii. Indeed, the formation energies of N_{Ga} antisites in GaN were also found to be very large for all values of the Fermi level [73], and we note that Zn, Ge, and Ga have similar atomic radii. In GaN, it was also found that Ga_N antisites are high in energy, and thus we expect Zn_N and Ge_N to also be energetically unfavorable.

Finally, we address the formation of Zn_{Ge}–Ge_{Zn} complexes. Since these cation antisites are the lowest-energy point defects, and they act as donors and acceptors, respectively, we expect that they might form a complex with high binding energy. Also, since the complex involves a simple interchange of Zn and Ge atoms, its formation energy is independent of chemical potentials. The formation energy of the Zn_{Ge}–Ge_{Zn} complex is included in Fig. 4.2. As expected, the complex is neutral for most Fermi-level positions, and the formation energy is 2.05 eV. The binding energy, defined as the energy difference between the formation energy of the complex and the sum of the formation energies of Zn_{Ge}^{2-} and Ge_{Zn}^{2+}, is 2.33 eV.

In the absence of impurities, Ge_{Zn}, Zn_{Ge} and V_{Zn} are the dominant defects. Charge neutrality between these defects will pin the Fermi level within the band gap. Under Ge-poor conditions, charge neutrality is achieved by having equal concentrations of Ge_{Zn}

and Zn_{Ge}, pinning the Fermi level at 1.44 eV below the CBM. Zn-poor conditions, on the other hand, will lead to the Fermi level being pinned at 0.56 eV below the CBM with equal concentrations of Ge_{Zn} donors and Zn_{Ge} or V_{Zn} acceptors. We have checked that any other combination of chemical potentials leads to Fermi-level positions between these two extremes. Hence, for any choice of chemical potentials, native point defects would lead to insulating behavior in $ZnGeN_2$, since the Fermi level would be pinned far away from the band edges.

4.4 Hydrogen and oxygen impurities in $ZnGeN_2$

Next, we consider hydrogen and oxygen impurities. These elements are ubiquitous during growth and can affect the electronic properties of unintentionally doped material. The formation energies of oxygen incorporated on the nitrogen site, O_N, and of the hydrogen interstitial, H_i, are plotted in Fig. 4.3 alongside the formation energies of Ge_{Zn}, Zn_{Ge}, and V_{Zn}.

We find O_N to act as a shallow donor in $ZnGeN_2$; that is, it is only stable in the singly positive charge state for all values of the Fermi level. The incorporation of O on the N site leads to a small outward relaxation of the nearest-neighbor Ge atoms, but a significantly larger displacement of the Zn neighbors. We find the O–Zn bond lengths to be about 9% larger than the equilibrium Zn–N bond length, while the O–Ge bonds are elongated by only $\sim$2%.

The hydrogen interstitial, H_i, is stable in the positive charge state for most of the band gap; the negative charge state can be stabilized when the Fermi level is within 0.06 eV from the CBM. In the positive charge state, the interstitial occupies a hydrogen bond-center position, between Zn and N, while in the negative charge state, it occupies the octahedral site. In nitride and oxide semiconductors, hydrogen can also substitute

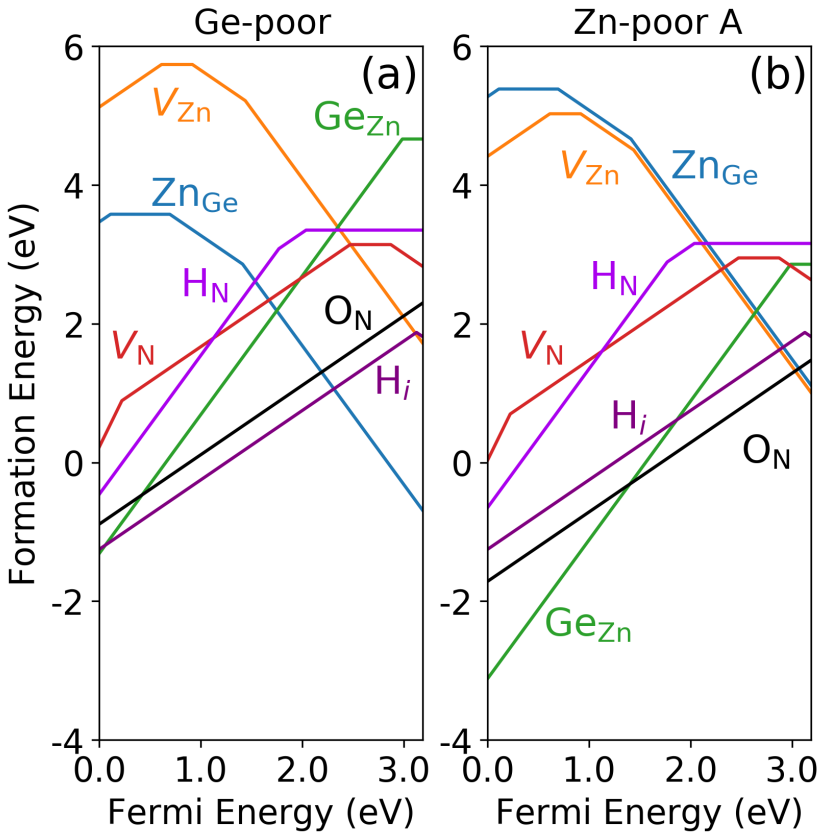

Figure 4.3: Formation energies of O_N and H_i impurities as well as the lowest-energy native point defects under (a) Ge-poor and (b) Zn-poor A conditions.

on the anion site (alternatively considered a complex with an anion vacancy) [74]. The formation energy of this H_N configuration is included in Fig. 4.3. H_N behaves as a deep donor, with (2+/+) and (+/0) levels well below the CBM. Therefore, unlike H_N in some nitrides [75], H_N in $ZnGeN_2$ will not contribute to n-type conductivity.

The incorporation of O_N and H_i will drive the Fermi level towards the conduction band, and these impurities (which can easily be present in the growth environment) could therefore in principle be responsible for the unintentional n-type conductivity that has been observed in some experiments [76]. However, Fig. 4.3 shows that significant compensation by the Zn_{Ge} and V_{Zn} acceptor-type defects is likely.

As noted in Sec. 1.3.1, the concentration of each defect, at equilibrium, follows a Boltzmann distribution:

$$c = N_{\text{sites}} e^{-\frac{E_D^f}{k_B T}} . \tag{4.5}$$

N_{sites} is the concentration of available sites for the defect to form, E_D^f is the formation energy of the defect as defined in Eq. (4.1), k_B is the Boltzmann constant, and T is the temperature. It is evident that only defects with low formation energies will be present in appreciable concentrations.

As an example, we consider the concentration of O_N donors that may form in $ZnGeN_2$ under Zn-poor conditions, based on the formation energies shown in Fig. 4.3(b). The formation energies depend on the Fermi level, which in turn is established by charge neutrality. For Zn-poor conditions, the Fermi level is pinned close to 3.03 eV above the VBM, where the formation energies of both the dominating defects (V_{Zn} and Zn_{Ge}) and O_N are equal to 1.32 eV. At a growth temperature of 755°C, as used in MOCVD growth of $ZnGeN_2$ [52], the resulting equilibrium concentration of O_N would be approximately 10^{16} cm^{-3}.

The actual formation energies of H_i and O_N will depend on the abundance of H and

O in the environment. The values shown in Fig. 4.3(b) assume equilibrium with ZnO, GeO_2, and H_2. If the concentration of oxygen can be increased beyond this value, n-type material could potentially be achieved. Our results show, however, that *unintentional* n-type doping due to hydrogen or oxygen is not very likely. In Chapter 5, we will expand on our methodology and examine intentional doping in $ZnGeN_2$.

4.5 Discussion

Skachkov *et al.* previously examined the electronic and structural properties of native point defects, oxygen and gallium impurities, and "exchange defects" such as the Zn_{Ge}–Ge_{Zn} complex in $ZnGeN_2$ using the LDA [60, 77]. While some of their results (such as on the qualitative issue of which defects have the lowest formation energies) agree with ours, important quantitative differences occur, both in the magnitude of formation energies and in the position of transition levels. To assess the impact of the underestimated LDA band gap on their results, Skachkov *et al.* employed an LDA+U approach, using an on-site U potential of ∼47 eV applied to the s states and ∼32 eV applied to the p states of Zn and Ge. While this may provide an *ad hoc* correction of the gap, the physical meaning of such a correction and its impact on total energies is unclear. We note that the enthalpies of formation of $ZnGeN_2$, Zn_3N_2, and Ge_3N_4 obtained by Skachkov *et al.* (estimated from the boundaries in their chemical potential diagram) differ significantly (by as much as several eV) from ours as well as from experiment (see Table 4.1).

In addition, the on-site U potential does not necessarily correct for the *absolute* position of the valence-band edge, which in turn affects the formation energies [6, 63, 73]. We can use the formation energy of Zn_{Ge} in the 2– charge state as a representative example. Under Zn-rich conditions, our HSE formation energy at the CBM for this defect is ∼2 eV larger than the LDA+U formation energy at the CBM. This is consistent with the

absolute position of the CBM in our calculations being as much as 1 eV lower than in Ref. [60]. In addition to shifts in the positions of charge-state transition levels, some transition levels that we identify to be stable in our calculations are missing in the work of Skachkov *et al.* [60] For instance, for Ge_{Zn} we find a (2+/0) level at 0.20 eV below the CBM, while Skachkov *et al.* report only the 2+ charge state to be stable across the band gap. In this case, we attribute the difference to a large lattice relaxation occurring for the neutral charge state, which may have been missed in Ref. [60]. For the Zn_{Ge}–Ge_{Zn} complex, Skachkov *et al.* reported a formation energy of 2.8 eV [77], significantly larger than our value of 2.05 eV (Fig. 4.2).

We also note that Ref. [60] reported very low formation energies for O_N, suggesting that oxygen would incorporate at high concentrations in $ZnGeN_2$. However, the reference for the oxygen chemical potential (μ_O) was taken as half of the total energy of an O_2 molecule. It is more realistic to assume that O_N incorporation is limited by the formation of competing phases such as GeO_2 and ZnO, which significantly raises the formation energy.

We agree with the qualitative conclusions of Skachkov *et al.* about the dominance of antisite defects and the role of Zn_{Ge} as a compensating center in n-type material. However, we also find V_{Zn} to be low in energy under Zn-poor conditions [see Fig. 4.2(b)], while Skachkov *et al.* find it to be higher than Zn_{Ge} by about 1.4 eV (when comparing similar chemical potential conditions).

4.6 Point defects in $ZnSiN_2$

$ZnSiN_2$ has a large indirect band gap of 4.83 eV. An indirect band gap suggests $ZnSiN_2$ is unlikely to be useful for optical emitters or absorbers, but may be practical as a wide-band-gap unipolar electronic device. We therefore investigate the native point

defects as they relate to n-type doping, focusing on the native acceptors that lead to charge compensation and evaluating O_N and H_i as donors. The native acceptors we examine are analogous to those we identified in $ZnGeN_2$: the cation vacancies V_{Zn} and V_{Si} and the zinc antisite Zn_{Si}. Formation energies for these defects are shown in Fig. 4.4.

Qualitatively, the native defects in $ZnSiN_2$ behave similarly to the native defects in $ZnGeN_2$. We find V_{Si} has much higher formation energy than V_{Zn} and Zn_{Si}, similar to the high formation energy seen for V_{Ge} in $ZnGeN_2$. V_{Zn} and Zn_{Si} have properties similar to V_{Zn} and Zn_{Ge} in $ZnGeN_2$: they both have low formation energies in the -2 charge state under n-type conditions. Furthermore, the positions of the transition levels of V_{Zn} and Zn_{Si} within the band gap of $ZnSiN_2$ are very similar to those of V_{Zn} and Zn_{Ge} in $ZnGeN_2$ when the band alignment between the two materials is taken into account. Band alignments will be examined in Chapter 7.

O_N has a (+/–) transition level within the gap; this is an example of DX-center behavior [78]. This phenomenon will be explored in more detail in Chapter 5. Since the transition level is very near the CBM (0.13 eV), O_N could still contribute electrons to the conduction band. In the positive charge state, O_N causes an asymmetric relaxation, with O–Zn bonds 11% longer than bulk N–Zn bonds but O–Si bond lengths within 2% of bulk N–Si bonds. In the negative charge state, the O atom shifts away from a nearest-neighbor Zn atom and assumes a position in the plane formed by the other nearest-neighbor Zn atom and the two nearest-neighbor Si atoms.

H_i has a (+/–) transition level deep within the gap, acting as an amphoteric impurity. H_i behaves as a deep donor in the presence of the native acceptors V_{Zn} and Zn_{Si}. The transition level occurs 1.33 eV below the CBM, significantly deeper in the gap than the 0.06 eV below the CBM found in $ZnGeN_2$. In the positive charge state, it again occupies a bond-center position between Zn and N. In the negative charge state, it occupies the octahedral site, as it does in $ZnGeN_2$. In Chapter 7, we will demonstrate how the H(+/–)

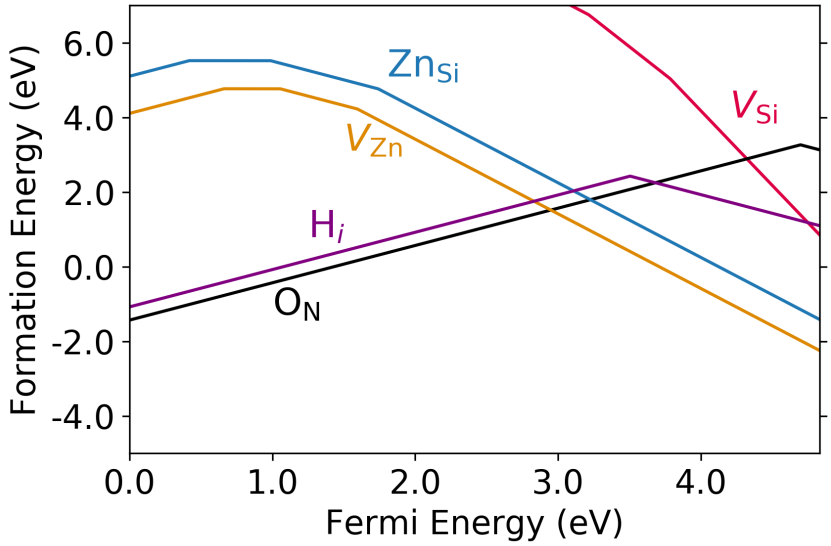

Figure 4.4: Formation energies of O_N and H_i impurities as well as the lowest-energy native point defects under Zn-poor conditions.

transition level can be used to align the band edges between the Zn-IV-nitrides and GaN.

4.7 Summary

We have investigated a variety of native point defects in $ZnGeN_2$ and $ZnSiN_2$. In $ZnGeN_2$, we found that the most stable defects are the V_{Zn} and the cation antisites Zn_{Ge} and Ge_{Zn}. In equilibrium, charge neutrality pins the Fermi level within the band gap, leading to insulating behavior. However, unintentionally incorporated impurities such as O_N and H_i can shift the Fermi level to near the CBM. In $ZnSiN_2$, we find V_{Zn} and Zn_{Si} have similar thermodynamic transition levels as the V_{Zn} and Zn_{Ge} defects in $ZnGeN_2$, when band alignment is taken into account.

Chapter 5

n-type doping in $ZnGeN_2$ and $ZnSiN_2$

This work was done in collaboration with Darshana Wickramaratne, Zhen Zhu, and Chris G. Van de Walle.

5.1 Introduction

The Zn-IV-nitrides have been considered for a variety of applications, such as solar cells [5], light-emitting diodes [48], and high-power electronics [44]. However, each of these applications requires controllable doping of the material.

Experimental work has shown that $ZnSnN_2$ is typically degenerately n-type doped, with carrier concentrations on the order of $10^{20} - 10^{21}$ cm^{-3}, while growth of $ZnGeN_2$ [79, 53] and $ZnSiN_2$ [43] typically results in insulating material. Theoretical work has pointed to O_N dopants and Sn_{Zn} antisites as the likely sources of n-type conductivity in $ZnSnN_2$ [59, 80]. As for $ZnGeN_2$, previous work using density functional theory demonstrated that O_N acts as a shallow donor and the Ge_{Zn} antisite acts as a deep donor; however, they are

heavily compensated by Zn_{Ge} antisite and V_{Zn} vacancy defects that act as acceptors [60]. We are not aware of any studies of defects or doping in $ZnSiN_2$. To determine if $ZnGeN_2$ and $ZnSiN_2$ can be intentionally doped, we examine a variety of donors and acceptors and evaluate the effect of compensation from the native defects we identified in Chapter 4.

Unlike binary semiconductors, the Zn-IV-nitrides have two distinct cations with different charges. To obtain strong n-type conductivity, we search for dopants with a strong preference for substitution on a specific site. If the dopant substitutes on the wrong site, it may contribute to compensation. Group-III dopants, such as Al, Ga, and In, may suffer from self-compensation as they are likely to substitute both on the Zn site as a donor, and on the group-IV site as a compensating acceptor. O has been investigated as an unintentional dopant, where it substitutes as a donor on the N site. Similarly, S and Se can be expected to preferentially substitute on the N site [78]. We also consider P and As, which can substitute as donors on the cation site and are isoelectronic with nitrogen.

DX behavior poses a challenge for n-type doping in wide-band-gap semiconductors. A *DX* center occurs when a donor impurity undergoes a large lattice relaxation and captures two electrons, in the process converting to an acceptor. For example, Si_{Ga} acts as a shallow donor in GaN, but for $Al_xGa_{1-x}N$ with high Al concentration, silicon has a transition level between the positive and negative charge states that lies within the band gap [78]. As a result, it is difficult to achieve high carrier concentrations in $Al_xGa_{1-x}N$ [81]. With a different set of potential donors, the Zn-IV-nitrides could potentially enable levels of n-type doping that are difficult to achieve in $Al_xGa_{1-x}N$.

Using our density functional methodology, we investigate P, As, S, and Se as dopants substituting on each potential site in $ZnGeN_2$ and $ZnSiN_2$. We compare the formation energies of these dopants acting as donors with their formation energies when incorporating on competing sites. Since the concentrations of the donors as well as the native

acceptors depend on the growth conditions, we calculate the n-type carrier concentration for a range of growth conditions to determine the effect of compensation and select the optimal donor for achieving n-type conductivity.

Our dopant calculations are performed using the HSE functional within the VASP program as previously discussed in Sec. 1.3.1. To evaluate each dopant, we determine the maximum carrier concentration that can be induced in each material. In equilibrium, the total number of positive and negative charges in the material will be equal. The positive charges in the material are the free holes and positively charged point defects or impurities, while the negative charges are the free electrons and negatively charged point defects or impurities. For n-type material, the hole concentration, p, is small and can be neglected. The concentration of charge resulting from a particular defect or impurity is

$$Q_{_i} = q_i N_{\text{sites}} \exp\left(\frac{-E_i^f}{k_B T}\right), \tag{5.1}$$

where q_i is the charge of the defect or impurity, N_{sites} is the concentration of sites it can occupy, E_i^f is the formation energy, k_B is Boltzmann's constant and T is the growth temperature. This expression is summed over all point defects and impurities in the system. The full charge balance equation in equilibrium can be written as:

$$\sum_i q_i N_{\text{sites}} \exp\left(\frac{-E_i^f}{k_B T}\right) = N_c \exp\left(\frac{-E_F}{k_B T}\right), \tag{5.2}$$

where the electron concentration, n, is expressed assuming the Boltzmann approximation (nondegenerate limit) and N_c is the effective density of states for the conduction band.

5.2 n-type doping in $ZnGeN_2$

As $ZnGeN_2$ is a ternary material, there are three types of substitutional impurities that can result in (single) donors: substitution of a group-III element on the Zn site, substitution of a group-V element on the Ge site, or substitution of a group-VI element on the N site. As will be discussed in detail in Chapter 6, the group-III elements (Al, Ga, and In) can substitute on the Zn site, where they act as donors, but also on the Ge site, where they act as acceptors. This strong tendency for self-compensation renders it difficult (or impossible) to obtain n-type doping with group-III elements. We will therefore focus on group-V and group-VI dopants. We will first examine the properties of each of the substitutional dopants, and then evaluate the carrier concentrations that can be achieved.

5.2.1 Group-V donors: P and As

In Fig. 5.1, we plot the formation energies as a function of Fermi level for P and As substituting on each of the Zn, Ge, or N sites. The group-V elements are expected to act as donors when substituting on the Ge site. Indeed, we find that P_{Ge} and As_{Ge} act as shallow donors (i.e., the positive charge state is the only stable charge state over the entire range of Fermi levels). We have explicitly investigated potential formation of DX centers and find that the (+/−) charge transition levels are not stable for P_{Ge} and As_{Ge}.

P_{Ge} and As_{Ge} also have relatively low formation energies. However, P and As can also substitute on the Zn or N sites, and the effects of incorporation on those sites need to be examined. On the Zn site, P and As should still act as donors (expected to be triple donors), but on the N site they are isoelectronic and would be expected to be electronically inactive. In Fig. 5.1 we plot the formation energies under N-poor conditions so as to show the worst-case scenario for incorporation on the N site.

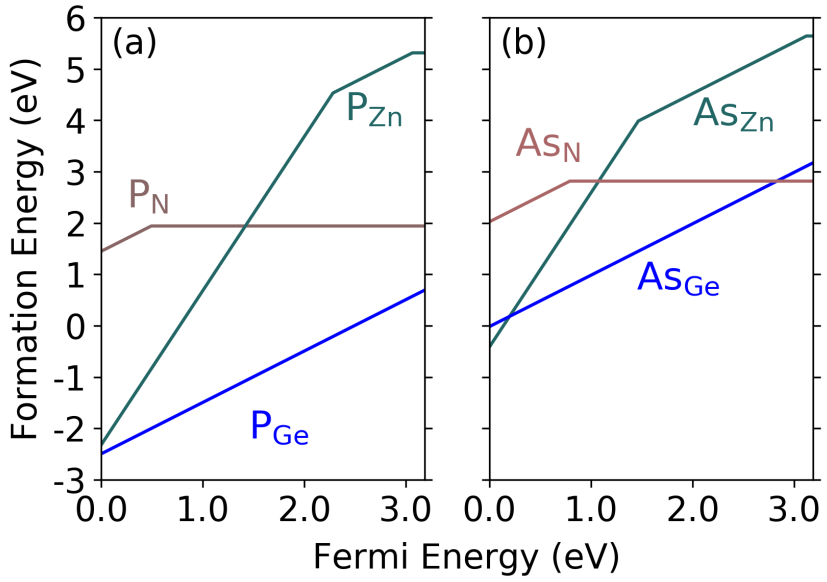

Figure 5.1: Formation energies for (a) P and (b) As substitutional impurities in $ZnGeN_2$ under N-poor conditions.

We find that P prefers to substitute on the Ge site for all chemical potentials and all Fermi levels. Examining the local relaxations we find that P_{Ge} bonds symmetrically to its four nearest-neighbor N atoms, causing a breathing relaxation as the four P–N bond lengths contract by 10% of the bulk Ge–N bond lengths. For P_N, there is an asymmetric relaxation in the neutral state, where the P–Zn bonds are 17% longer than bulk N–Zn bonds, and the P–Ge bonds are 9% longer than bulk N–Ge bonds. These large relaxations are an indication of the size mismatch between P and N, and partially explain why, despite P being isoelectronic to N, P_N has a significantly higher formation energy than P_{Ge}. We also find P_{Zn} acts as a triple donor, but has a very high formation energy under n-type conditions and is unlikely to form.

As shown in Fig. 5.1, we find that As prefers substitution on the Ge site for most Fermi levels, but under N-poor conditions, As_N is more stable than As_{Ge} when the Fermi level is high in the gap. Conveniently, since As_N is electrically neutral under n-type conditions, it will not compensate As_{Ge} donors. In terms of relaxations, we find that

As_{Ge} in the positive charge state causes only a small breathing relaxation where As–N bond lengths are 3% shorter than bulk Ge–N bond lengths. Similar to P_N, As_N causes a large asymmetric relaxation, where As–Zn bonds are 20% longer than bulk N–Zn bonds and As–Ge bonds are 11% longer than bulk N–Ge bonds. Lastly, like P_{Zn}, As_{Zn} acts as a donor, but under n-type conditions, it is unlikely to form.

Ionic radii can be used to explain the relaxations around P_{Ge} and As_{Ge} in the positive charge state. P^{5+} has an ionic radius of 0.17 Å, As^{5+} 0.34 Å, and Ge^{4+} 0.39 Å [82]. The differences in these ionic radii agree with the differences in length between the N–P, N–As, and N–Ge bond lengths to within 0.03 Å.

P and As are isovalent with N and we therefore expect them to occur in the neutral charge state. We find, however, that for Fermi levels in the lower part of the gap they can also be stable in the positive charge state. The positive charge states are associated with localized hole states. These findings are consistent with the As_N substitutional impurity in GaN [83, 84].

5.2.2 Group-VI donors: S and Se

In Chapter 4, we studied O as a potential unintentional dopant and found that O_N acts as a shallow donor, but O doping does not lead to high n-type conductivity due to effects of compensation. However, other group-VI elements such as S and Se may act as good donors. This is indeed confirmed by the results in Fig. 5.2, where S_N, and Se_N are found to be stable only in a positive charge state. DX configurations are not stable; in each case, the transition level between the between the positive and negative charge states occurs well above the CBM.

The formation energies in Fig. 5.2 are plotted for Zn-poor conditions. Since we would like the group-VI dopants to substitute on the N site, Zn-poor (i.e., N-rich) conditions

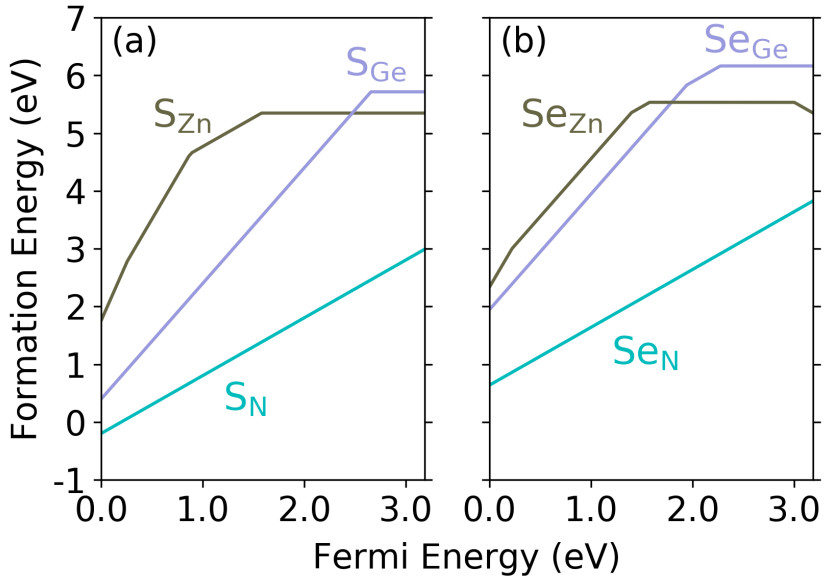

Figure 5.2: Formation energies for (a) S and (b) Se substitutional impurities in $ZnGeN_2$ under Zn-poor conditions [Zn-poor B in Fig. 4.1(a)].

constitute a worst-case scenario for such incorporation. Even then, S_{Zn}, Se_{Zn}, S_{Ge}, and Se_{Ge} all have much higher formation energies than S_N or Se_N. Substitution on the N site is thus strongly preferred under all growth conditions. However, the formation energies of S_N and Se_N are high when E_F is high in the gap, and we will see that this leads to very low electron concentrations when n-type doping is attempted.

S_N bonds to two Zn atoms and two Ge atoms. In the positive charge state, S_N causes a large asymmetric relaxation, where S–Ge bond lengths are 19% longer than bulk N–Ge bond lengths and S–Zn bond lengths are 12% longer than bulk N–Zn bond lengths. A similar relaxation occurs for Se_N in the positive charge state, where Se–Ge are 23% longer than bulk N–Ge bonds, and Se–Zn bonds are 15% longer than N–Zn bonds.

5.2.3 Carrier concentrations

We now examine the levels of n-type doping that can be achieved with various donor impurities. This will depend on the formation energies of the substitutional donors

as well as any compensating acceptors that may form. In Chapter 4, we previously identified Zn_{Ge} and V_{Zn} as the dominant native acceptors in $ZnGeN_2$, V_{Ge} being much less likely to form. In Fig. 5.3 we plot the formation energies of these dominant acceptors alongside those of our candidate donors. We chose Zn-poor conditions, which were found to suppress the formation of native acceptors. The plot shows that even under these conditions, compensation by native acceptors is a serious problem in $ZnGeN_2$. However, given that there is a lot of flexibility in choosing chemical potentials (corresponding to growth under different conditions), one may wonder whether it is possible to identify conditions that would be more optimal for achieving n-type doping.

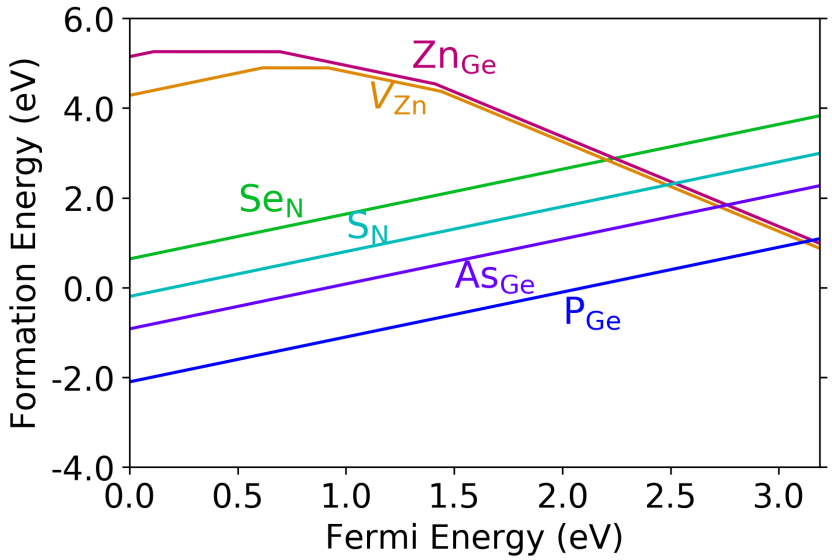

Figure 5.3: Formation energies for candidate dopants and native acceptors in $ZnGeN_2$ under Zn-poor conditions [Zn-poor B in Fig. 4.1(a)].

To examine this, we investigate the actual carrier concentrations that can be achieved. These depend on the concentrations of donors and acceptors in the system, which are determined by their formation energies. We have seen that these formation energies depend on the Fermi level. In an actual material, the Fermi level is fixed by the condition of charge neutrality, as expressed in Eq. (5.2). We perform this investigation over the full

range of allowed chemical potentials, which is determined by the phase stability diagram for $ZnGeN_2$, shown in Fig. 4.1(a). This diagram shows the range of chemical potentials $\Delta\mu_i$ for each element i for which $ZnGeN_2$ is stable, in the presence of competing phases. Small changes in chemical potential can significantly change defect concentrations, due to the exponential dependence in Eq. (5.1).

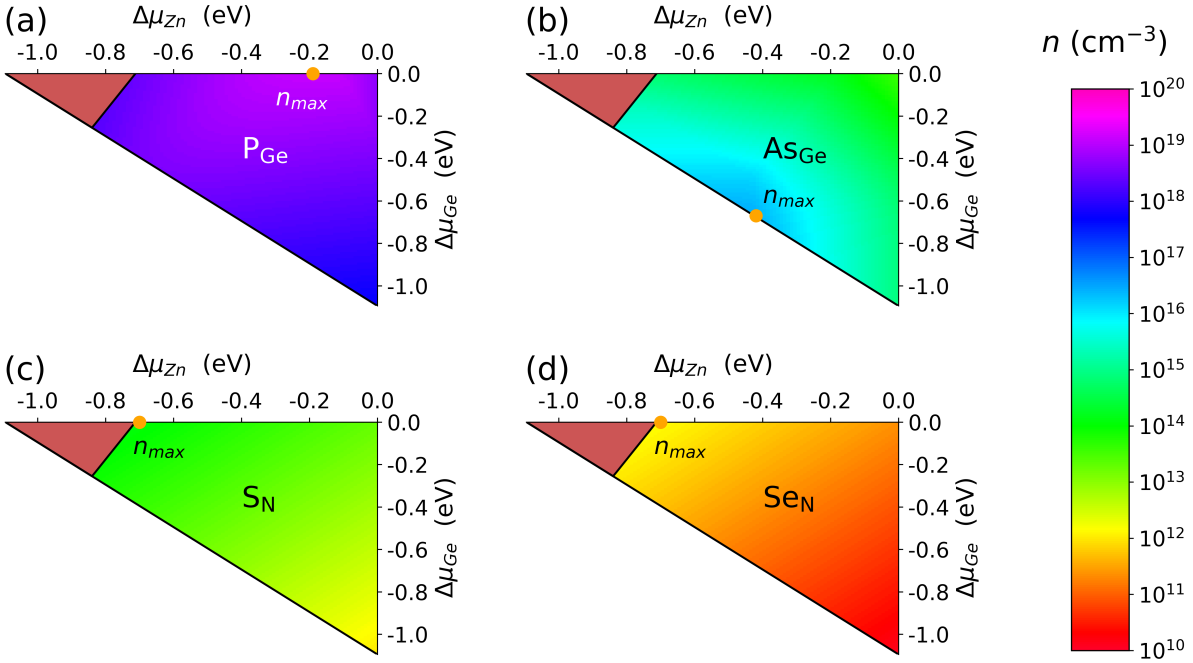

Figure 5.4: Calculated electron concentration as a function of chemical potentials for $ZnGeN_2$ doped with (a) P, (b) As, (c) S, or (d) Se, for a range of chemical potentials allowed by the phase stability diagram [Fig. 4.1(a)] and at a growth temperature of 1000 K. The chemical potential condition that enables the highest carrier concentration is indicated by n_{max} for each dopant.

In Fig. 5.4, we use a color map to illustrate how the electron concentration depends on the chemical potential for each dopant at a growth temperature of 1000 K. The carrier concentration results from solving the charge-balance condition [Eq. (5.2)] quantitatively, including potential compensation by native acceptors.

Phosphorous [Fig. 5.4(a)] stands out as the best dopant; we find that a concentration of $n = 1.3 \times 10^{19}$ cm^{-3} can be achieved. Notably, we find that the maximum carrier

concentration is found neither at the Zn-poor condition, where the formation energy of the acceptors is highest, nor at the Ge-poor condition, where the formation energy of the P_{Ge} is lowest, but somewhere in the middle, near the N-poor condition.

When doping with arsenic [Fig. 5.4(b)], it is possible to reach concentrations up to $n = 2 \times 10^{16}$ cm^{-3} for conditions roughly midway between the Zn-poor and Ge-poor limits. Sulfur and selenium, finally, are found to be poor dopants (which was evident already from their high formation energies, Fig. 5.2). Sulfur can yield concentrations up to $n = 1 \times 10^{14}$ cm^{-3}, while with selenium $n = 1 \times 10^{12}$ cm^{-3} can be achieved, both under Zn-poor conditions.

5.3 n-type doping in $ZnSiN_2$

For $ZnSiN_2$ we study the same dopants as for $ZnGeN_2$. We will present the results for the dopant configurations in less detail because, as we will show, compensation by native acceptors is an insurmountable problem in $ZnSiN_2$.

In Fig. 5.5, we plot the formation energy of these donors along with the acceptors identified in Sec. 4.6. Similar to the case of $ZnGeN_2$, we find that As_{Si} has much higher formation energy than P_{Si}, and that Se_N has much higher formation energy than S_N. We have also found that Al, Ga, and In, can substitute both as a donor on the Zn site or as an acceptor on the Si sites. As a result, they self-compensate and will not lead to n-type doping. Therefore, we focus on P_{Si} and S_N as potential donors.

P_{Si} is a shallow donor, stable only in the +1 charge state. P_{Si} gives rise to a small breathing relaxation where the P–N bonds are 4.8% shorter than bulk Si–N bonds. The P–N bond lengths in $ZnSiN_2$ are similar to the P–N bonds in $ZnGeN_2$ (just 0.9% shorter). The P_{Si} $\epsilon(+/0)$ and $\epsilon(0/-)$ transition levels occur well above the CBM, indicating that P_{Si} does not exhibit DX-center behavior.

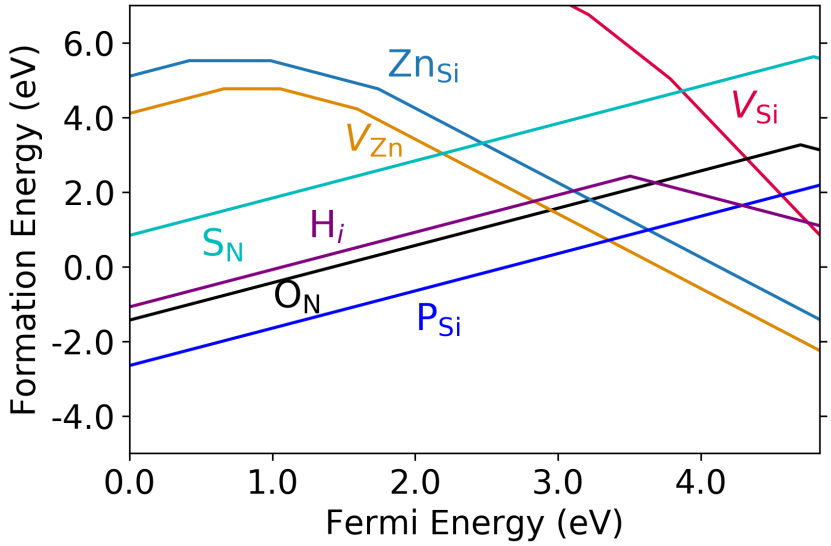

Figure 5.5: Formation energies for candidate dopants and native acceptors in $ZnSiN_2$ under Zn-poor conditions.

S_N behaves as a DX-center, just like O_N (see Sec. 4.6). However, its (+/–) transition level is only 0.04 eV below the CBM. As a result, S_N can still contribute electrons to the conduction band. In the positive charge state, the atoms around S_N relax in a manner qualitatively similar to the relaxation around O_N (Sec. 4.6). S–Zn bonds are 10% longer than bulk N–Zn bonds and S–Si bonds are 21% longer than bulk N–Si bonds. The quantitative differences with the case of oxygen are consistent with the fact that S has a larger ionic radius than O. However, in the negative charge state, the relaxations differ from the oxygen case. For S_N there is no significant change in the position of the S atom; however, one of the nearest neighbor Si atoms moves away from the S atom by 21% of the bulk N–Si bond length; while for O_N, the oxygen atom shifts significantly.

While we observe that P_{Si} acts a shallow donor and S_N and O_N have transitions to the negative charge state near the CBM, compensation by native acceptors is very strong in $ZnSiN_2$. A significant difference between the native defects in $ZnGeN_2$ and $ZnSiN_2$ is that the formation energy of V_{Zn} is much lower in $ZnSiN_2$ than in $ZnGeN_2$. In particular,

the formation energy of V_{Zn} is negative for the Fermi level at the CBM for any choice of chemical potentials. As a result, V_{Zn} would spontaneously form in any n-type $ZnSiN_2$, and therefore n-type conductivity cannot be achieved.

5.4 Summary

We have investigated a variety of potential donors in $ZnGeN_2$. We find S_N, Se_N, P_{Ge}, and As_{Ge} act as shallow donors. However, compensation by the native Zn_{Ge} and V_{Zn} acceptors can hamper doping. We identify P_{Ge} as the best donor: n-type carrier concentrations up to 1.3×10^{19} cm^{-3} may be achieved under N-poor conditions. In $ZnSiN_2$, we identify P_{Si} as a shallow donor; however, the compensation by native acceptors is much stronger. V_{Zn} will form spontaneously for any choice of chemical potentials and it is not possible to achieve n-type conductivity in $ZnSiN_2$.

Chapter 6

p-type doping in $ZnGeN_2$

This work was done in collaboration with Darshana Wickramaratne, Zhen Zhu, and Chris G. Van de Walle.

6.1 Introduction

Light-emitting devices require both an n-type layer and a p-type layer. We have shown that n-type doping is feasible in $ZnGeN_2$ using phosphorus doping; however, it is p-type doping that has proven to be more challenging for nitride semiconductors. The primary issue is a lack of acceptor dopants with low ionization energies [85]. In GaN optoelectronics, use of Mg to achieve controlled p-type doping has proven very successful [86]. Translating this success to the II-IV-nitrides requires a thorough understanding of the electronic properties of candidate p-type dopants. We focus on $ZnGeN_2$ because of its close lattice match to GaN and potential for integration in III-nitride/II-IV-nitride heterostructures. At present, no experimental reports on p-type doping of $ZnGeN_2$ are available. Accurate first-principles calculations can lead the way in addressing the prospects and challenges associated with acceptor doping in $ZnGeN_2$.

Skachkov *et al.* [60] previously performed density functional theory (DFT) calculations on Ga acceptors in $ZnGeN_2$. However, as discussed in Sec. 4.5 their approach using the local density approximation (LDA) severely underestimates the band gap and falls short in describing charge localization, an issue that is particularly important for correctly calculating the ionization energy of acceptors [6, 87]. Use of a hybrid functional overcomes these problems. Hybrid functional calculations were applied by Wang *et al.* [57] to $ZnSnN_2$, which has a lower band gap than $ZnGeN_2$; they identified Li_{Zn} as a shallow acceptor.

Acceptor doping of $ZnGeN_2$ can be achieved with group-I elements substituting on the Zn site; group-III elements substituting on the Ge site; or group-IV elements substituting on the N site. We examine a wide array of candidate acceptors: Li_{Zn}, Li_{Ge}, Cu_{Zn}; Al_{Ge}, Ga_{Ge}, and In_{Ge}; and C_N. Among these, Li_{Zn}, Al_{Ge}, and Ga_{Ge} will be found to have small enough ionization energies to enable p-type conductivity.

We also examine compensation by native defects, as well as self-compensation due to incorporation of the dopant on the "wrong" site: for instance, Al_{Ge} acts as an acceptor, but Al_{Zn} as a donor. The similarity in ionic radii between Zn and Ge indeed leads to a propensity for wrong-site substitution, causing severe self-compensation. We will also propose a potential solution in the form of co-doping with hydrogen. The incorporation of hydrogen donors can be more favorable than the incorporation of wrong-site dopants, thus suppressing self-compensation. Our detailed examinations include calculations of hydrogen-dopant complexes, thus providing guidance as to whether co-doping with hydrogen and subsequent removal of hydrogen in a post-growth anneal is a viable route for p-type doping in $ZnGeN_2$.

6.2 Acceptor levels

We use the same calculation methods as previously discussed in Sec. 1.3.1 using the $2 \times 2 \times 2$ supercell with 128 atoms. The chemical potentials are illustrated in Fig. 4.1(a), and we focus on two extrema in plotting our chemical potentials: Ge-poor (which is N and Zn rich), and Zn-poor A (which is Ge and N rich). For our investigations of candidate acceptors, we use Li_3N, Cu metal, diamond, AlN, GaN and InN as limiting phases. For each dopant configuration we report a formation energy based on chemical potentials that would maximize the incorporation of the acceptor on their respective substitutional site, based on calculated formation enthalpies for Li_3N (-1.65 eV), AlN (-3.15 eV), and GaN (-1.2 eV); these values are in agreement with experiment [67, 68]. In our calculations involving hydrogen we assume μ_{H} is determined by the H_2 molecule at T=0.

The ionization energy of an acceptor is given by the thermodynamic charge-state transition level, $\epsilon(q/q')$. This transition level is defined as the Fermi-level position below which the defect is stable in the charge state q and above which it is stable in the charge state q'. For example, for the case of the Al_{Ge} acceptor, the ionization energy is determined as:

$$\epsilon(0/-) = E^f({Al_{Ge}}^{-1}; E_F = 0) - E^f({Al_{Ge}}^{0}; E_F = 0). \tag{6.1}$$

where $E^f({Al_{Ge}}^{-1}; E_F = 0)$ is the formation energy of Al_{Ge} in the negative charge when the Fermi level is at the VBM and $E^f({Al_{Ge}}^{0}; E_F = 0)$ is the formation energy of Al_{Ge} in the neutral charge state. We will also call this quantity the acceptor level.

The calculated charge-state transition levels are shown in Fig. 6.1. From this figure it is clear that Cu_{Zn}, In_{Ge}, and C_N have deep acceptor levels and cannot lead to p-type conductivity in $ZnGeN_2$. We also considered Li_{Ge} and find it has a large ionization

	Li_{Zn}	Al_{Ge}	Ga_{Ge}
$\epsilon(0/-)$	0.36	0.24	0.30
$E_b(A-D)$	0.99	0.57	0.58
$E_b(A-H)$	1.08	0.55	0.58

Table 6.1: Properties of candidate acceptors in $ZnGeN_2$. $\epsilon(0/-)$ is the acceptor level referenced to the VBM (i.e., the ionization energy). $E_b(A$–$D)$ is the binding energy of the acceptor-donor complex, where the donor is the dopant incorporated on the wrong site. $E_b(A$–H) the binding energy of the acceptor-hydrogen complex. All quantities are in eV.

energy (1.01 eV). The best candidates for shallow acceptors are Li_{Zn}, Al_{Ge} and Ga_{Ge}, with ionization energies of 0.36, 0.24, and 0.30 eV, as listed in Table 6.1. The ionization energy of Al_{Ge}, 0.24 eV, is close to the ionization energy for Mg_{Ga} in GaN (0.26 eV, Ref. [85]) and would thus lead to a reasonable hole concentration. The equations for carrier concentrations in a doped semiconductor show that the hole concentration at room temperature decreases by roughly an order of magnitude for every 100 meV increase in ionization energy. An ionization energy of 0.46 eV due to In_{Ge} would therefore probably be too high to lead to a useful hole concentration. Hence, among the acceptors we have investigated, p-type doping of $ZnGeN_2$ should be feasible using Li, Al, or Ga.

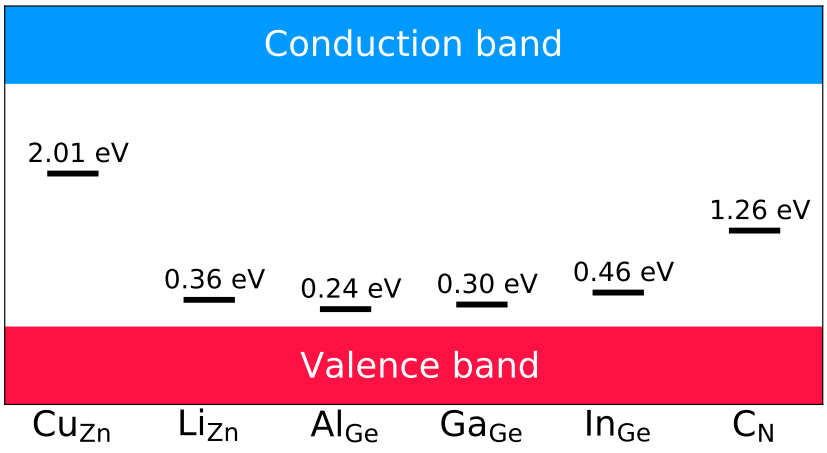

Figure 6.1: Thermodynamic transition levels for candidate acceptors in $ZnGeN_2$. The zero of energy is set at the VBM. Values for ionization energies are indicated.

6.3 Acceptors and compensation

We now discuss the atomic structure of these potential p-type dopants. In Figs. 6.2(d)-(i), we illustrate the local relaxations in terms of deviations from the bulk bond lengths. For Li_{Zn} in the negative charge state [Fig. 6.2(e)], a small breathing relaxation occurs in which the Li–N bonds are extended by ∼1% compared to Zn–N bond lengths in the bulk. In the neutral charge state, however, a large asymmetric relaxation occurs [Fig. 6.2(d)]: three Li–N bonds contract by ∼1.6%, while the fourth Li–N bond extends by 16%, compared to the bulk Zn–N bond lengths. For Al^{-}_{Ge} [Fig. 6.2(g)], there is a breathing relaxation in which Al–N bonds extend by ∼0.4% of the bulk Ge–N bond length; for Ga^{-}_{Ge} [Fig. 6.2(i)], this relaxation is an extension of Ga–N bonds by ∼3.7%. The smaller relaxation of the N atoms in the case of Al_{Ge} compared to Ga_{Ge} can be understood by comparing the ionic radii of Al and Ga in the 3+ charge state with Ge in the 4+ charge state: the ionic radius of Al is identical to that of Ge (0.39 Å), while that of Ga is significantly larger (0.47 Å) [82]. In the neutral charge state, Al_{Ge} [Fig. 6.2(f)] and Ga_{Ge} [Fig. 6.2(h)] exhibit an asymmetric relaxation. For Al_{Ge}, one of the Al–N bond lengths is 2.7% longer than bulk Ge–N bonds, while the other three Al–N bonds are close to the bulk Ge–N bond lengths. For Ga_{Ge}, one of the Ga–N bond lengths is 5.6% longer than the bulk Ge–N bond lengths, while the other three bonds are only about 3.1% longer than bulk lengths.

The formation energies of these candidate acceptors are illustrated in Figs. 6.2(a)-(c). In each case, we focus on a regime where incorporation of the appropriate substitutional configuration of the acceptor is favored: Li should go on a Zn site, which calls for Zn-poor (Ge-rich) conditions, while Al and Ga should go on a Ge site, calling for Zn-rich (Ge-poor) conditions. Figures 6.2(a)-(c) also include information about other configurations of the dopant that may lead to self-compensation. The similarity in atomic size of Zn

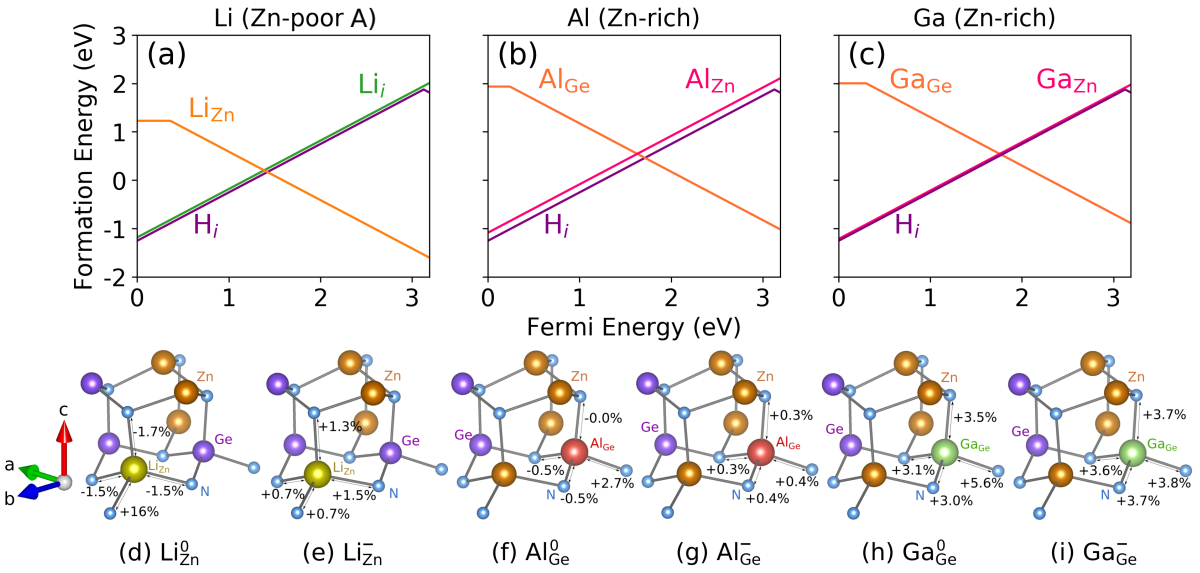

Figure 6.2: Formation energies for (a) Li, (b) Al and (c) Ga in $ZnGeN_2$. The chemical-potential conditions used in each case are shown at the top of each panel. Local relaxations for (d), (e) Li_{Zn}, (f), (g) Al_{Ge}, and (h), (i) Ga_{Ge} in the neutral and negative charge states.

and Ge suggests that Al and Ga may choose to substitute on the Zn site instead of the Ge site, where they will act as donors. In the case of Li, self-compensation may occur by incorporation of Li as an interstitial (Li_i).

In principle we should also consider compensation by native defects. Under Zn-rich conditions, our previous calculations of defect formation energies [24] (see Sec. 1.3.1) indicate that the Ge_{Zn} antisite is the lowest-energy native donor. However, its formation energy is higher than that of the Al_{Zn} and Ga_{Zn} donors, indicating that wrong-site incorporation is the more severe problem. Under Zn-poor conditions, where the incorporation of Al and Ga on the Ge site decreases, self-compensation by Al_{Zn} and Ga_{Zn} donors remains the more severe problem. Turning to Li, under Zn-poor conditions, where the incorporation of Li_{Zn} is favored, we find compensation by the Ge_{Zn} antisite to be more severe than self-compensation. However, under Zn-rich conditions, where the formation energy of both Li_{Zn} and Ge_{Zn} is higher, we find self-compensation by Li_i to be more

severe.

Li_i, Al_{Zn}, and Ga_{Zn} all act as shallow donors, i.e., the positive charge state is the only stable charge state for all Fermi-level positions. The Li interstitial is located in the octahedral site. Incorporation of Al or Ga on the Zn site leads to a symmetric relaxation of the nearest-neighbor N atoms. For Al_{Zn}^{+} the N atoms relax inwards by up to 6.0%, and for Ga_{Zn} by 3.4%. Al_i and Ga_i interstitials are also potential compensating donors, but we find them to have significantly higher formation energies compared to Al_{Zn} and Ga_{Zn}.

Charge neutrality requires the concentration of positively and negatively charged defects and impurities to be equal. In the absence of other defects or impurities, the presence of compensating donors pins the Fermi level at a position corresponding to the intersection point of the formation energies of the donors and acceptors. In the example of Al, the intersection between Al_{Zn}^{+} and Al_{Ge}^{-} occurs at E_F=1.63 eV; this is far away from the VBM and the material will be insulating rather than p-type.

We have also considered the formation of complexes between the negatively charged acceptors and the positively charged donors. We can assess the stability of the Al_{Ge}–Al_{Zn} and Ga_{Ge}–Ga_{Zn} complexes by calculating their formation energies. The binding energy is defined as the energy difference between the formation energy of the neutral complex (which is its only stable charge state) and the sum of the formation energies of the negative acceptor and the positive donor. The binding energies are listed in Table 6.1.

6.4 Hydrogen co-doping

From the results in Fig. 6.2 it is evident that self-compensation is a serious problem. We now discuss a potential strategy to avoid or at least suppress self-compensation, namely co-doping with hydrogen. This approach is inspired by the example of Mg-doped GaN: growth in a hydrogen-rich environment (such as metal-organic chemical vapor depo-

sition) leads to strong compensation by hydrogen donors, suppressing the incorporation of other potential compensating species in the process. However, the advantage of hydrogen as a compensating donor is that it is sufficiently mobile to be removed from the p-type layer in a post-growth anneal, leading to activation of the Mg_{Ga} acceptors [86, 88].

Figure 6.2 includes our calculated formation energy for interstitial H (previously discussed in Sec. 4.4). The case of Al illustrates that the formation energy of H_i is lower than that of the compensating Al_{Zn} donor. Hydrogen will thus be preferentially incorporated, suppressing incorporation of Al on the Zn site. An additional advantage of the hydrogen co-doping is that the Fermi level where the formation energies of donors and acceptors intersect is shifted higher, leading to a decrease in the acceptor formation energy and a higher concentration of acceptors.

Still, the material that is grown in the presence of hydrogen will be completely compensated, with a Fermi level somewhere in the middle of the gap. Generating p-type material depends on the ability to remove hydrogen from the acceptor-doped layer. This needs to be accomplished at a temperature that is sufficiently high to effectively remove hydrogen, but low enough to "freeze in" the impurities at the concentrations that were established during the (hydrogen-rich) growth, and prevent formation of new defects.

To calculate migration barriers, we use the nudged elastic band (NEB) method [89, 90]. In bulk $ZnGeN_2$, H_i^+ is preferentially located in a bond-center position between Zn and N. Configurations placing H_i^+ near Ge are much higher in energy; therefore, we calculate the barrier for each hop the H_i^+ ion makes between Zn–N bonds. Each hop consists of a rotation around either a N atom or a Zn atom. Net diffusion requires repeatedly making both types of hops. These hops are illustrated in Figs. 6.3(a) and (b), with saddle points along the hops labeled B_1, B_2, and B_3. The hop around a N atom has a low barrier of 0.2 eV. Hops around a Zn atom have a larger barrier, with a slight anisotropy: hops along the c axis [Fig. 6.3(a)] have a barrier of 1.3 eV, while hops along

the a axis [Fig. 6.3(b)] have a barrier of 1.1 eV. The difference between these barriers is because the H_i^+ ion experiences slightly higher repulsion from second-nearest-neighbor Zn cations while hopping along the c axis. The hop around the N atom is much lower in energy as the H_i^+ is bonded to and remains close to the N atom throughout the hop, while the hop around the Zn atom breaks the N-H bond.

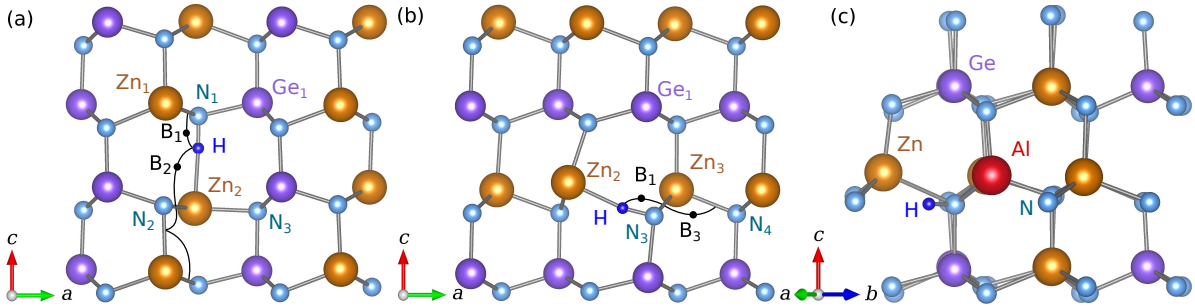

Figure 6.3: (a), (b) Schematic of bonding arrangement within the two distinct layers of $ZnGeN_2$ perpendicular to the b axis, illustrating the connectivity of Zn–N bonds. (a) Path for H_i migration along the c axis, with B_1 and B_2 indicating saddle points. (b) Path for H_i migration along the a axis. A subset of atoms labeled in (a) are the same atoms as in (b). (c) Schematic illustration of the Al_{Ge}–H complex.

Fig. 6.3(a) shows a chain of Zn–N bonds along the c axis. The maximum diffusion barrier along this chain is at the saddle point B_2 with a height of 1.3 eV. Fig. 6.3(b) shows a chain of Zn–N bonds along the a axis. The maximum diffusion barrier along this chain is at the saddle point B_3 with a height of 1.1 eV. There is no similar chain along the b axis, but each H_i^+ ion hop has some displacement component along b. Alternating the steps illustrated for travel along the a and c axes enables net movement and diffusion along the b axis; therefore, H_i^+ can travel between Zn–N bond centers in all three spatial directions with modest migration barriers.

The H_i^+ migration barriers of 1.3 eV along the c axis and 1.1 eV along the a axis in $ZnGeN_2$ are similar to H_i^+ barriers in GaN [91, 92]. This migration barrier is low enough to suggest that moving hydrogen around should not be a problem at elevated temperatures. However, H_i^+ will be attracted to the negatively charged acceptors, and

thus additional energy may be required to dissociate acceptor-hydrogen complexes.

We have therefore investigated Li_{Zn}–H, Ga_{Ge}–H, and Al_{Ge}–H complexes. The Al_{Ge}–H complex is illustrated schematically in Fig. 6.3(c). We find each complex to be stable only in the neutral charge state. In the Li_{Zn}–H complex, hydrogen assumes a position similar to its position in the bulk, close to the center of the Li–N bond. In contrast, in the Al_{Ge}–H and Ga_{Ge}–H complexes, the H_i^+ ion sits in the antibonding position on the extension of a nearby Zn–N bond. The H_i^+ ion is not collinear with the Zn–N bond, but is shifted slightly towards the nearest Zn atom, as seen in Fig. 6.3(c). The binding energies for the acceptor-hydrogen complexes are listed in Table 6.1.

We find the binding energies to be about 0.6 eV for Al and Ga; this is lower than the binding energy of the Mg–H complex in GaN, calculated to be 1.02 eV [85]. This suggests that modest annealing temperatures can be used to disassociate such complexes and remove the hydrogen. As illustrated by Fig. 6.2 and Table 6.1, Al appears to be the best candidate for p-type doping of $ZnGeN_2$.

We note that the formation energies in Fig. 6.2 are plotted for specific choices of the chemical potentials. Specifically, we assumed the highest possible chemical potential of the impurity, corresponding to the solubility limit. At lower impurity concentrations the extent to which hydrogen suppresses compensation would be stronger. In addition, growth conditions that are more hydrogen-rich than assumed in Fig. 6.2 may be achievable.

6.5 Summary

In summary, we have determined the acceptor ionization energies for a wide range of candidate dopants in $ZnGeN_2$. The ionization energy of Al_{Ge} is only 0.24 eV, which is comparable to Mg in GaN. Co-doping with hydrogen is a potential strategy to sur-

mount issues of compensation: incorporation of hydrogen suppresses the formation of self-compensating donors, and hydrogen can be removed in a post-growth anneal.

Chapter 7

Heterostructures with Zn-IV-nitrides

This work was done in collaboration with Darshana Wickramaratne and Chris G. Van de Walle. The calculation of the $H_i(+/-)$ charge transition level in GaN was done by Darshana Wickramaratne. We thank C. E. Dreyer for helpful discussions about determining spontaneous and piezoelectric polarization.

7.1 Introduction

Electronic and optoelectronic devices function by localizing electrons and/or holes in a thin active region or channel. Electronic devices modulate the concentration of charge and its flow using applied voltages, while optoelectronic devices make use of recombination of holes and electrons to emit light. Both types of devices require control over the band alignments to confine the carriers.

Previous work has already addressed band alignments between the Zn-IV-nitrides and the III-nitrides. Punya *et al.*[93, 94] calculated band alignments between $ZnGeN_2$ and

GaN that found the VBM and CBM of $ZnGeN_2$ higher in energy than those of GaN. This configuration means holes and electrons would not be confined to the same layers and has lead to device designs for quantum wells with higher wavefunction overlap [38, 39] and quantum-cascade lasers [37].

Other studies have reported different results for the band alignments, however. All of the studies used explicit interface calculations based on a superlattice geometry. The calculations by Punya *et al.* [93, 94] used the local density approximation with a GW correction. They calculated a valence-band offset of –1.4 eV at the $ZnSnN_2$/GaN interface, and a valence-band offset of -1.1 eV at $ZnGeN_2$/GaN, where the negative sign indicates that the VBM of GaN is lower in each case. These results differ significantly from those of Wang *et al.* [57] who calculated offsets between $ZnSnN_2$ and GaN using the HSE hybrid functional. They calculated a much smaller valence-band offset of –0.39 eV between $ZnSnN_2$ and GaN, where they also noted strain affects the alignment by less than 0.1 eV. More recently, Cao *et al.* [95] calculated the offset between cubic GaN and cubic $ZnGeN_2$ with the HSE functional and found the valence-band offset for $ZnGeN_2$/GaN to be -0.38 eV, different by 0.7 eV from the results of Punya *et al.* [93, 94] Experimentally, the valence- and conduction-band alignments for $ZnSn_{1-x}Ge_xN_2$ alloys of varying composition were measured using x-ray emission and absorption by Narang *et al.* [46], who found the valence band of $ZnGeN_2$ to be slightly lower than that of $ZnSnN_2$, and the conduction band of $ZnGeN_2$ to be significantly higher than that of $ZnSnN_2$.

These inconsistencies (by up to 1 eV) between band alignments reported by different groups prompted us to re-examine band alignments using two different methodologies: (1) using surface calculations to align the electrostatic potential to the vacuum level [96], and (2) using alignment based on the $(+/-)$ level of interstitial hydrogen [21]. We apply both methods to determine the band alignments between the Zn-IV-nitrides and GaN, and compare the results to previous reports.

Another key aspect of nitride heterostructures is polarization charge at the interface. The Zn-IV-nitrides, like the wurtzite (wz) III-nitrides, exhibit spontaneous polarization and piezoelectric effects [3, 97]. The polarization leads to large bound charges at the interface, which can either be a detriment or provide useful functionality for device operation. In light-emitting devices, polarization discontinuities produce the quantum-confined Stark effect, which reduces electron-hole wavefunction overlap and reduces efficiency [98]. On the other hand, large polarization discontinuities can be favorable for electronic devices since they lead to high-density two-dimensional carrier gases at interfaces [99]. Interest in controlling these polarization charges has led to the field of polarization engineering [10], which relies on the manipulation and control of ternary and quaternary alloy concentrations to identify polarization differences that are beneficial for the intended device application, taking lattice-matching constraints into account.

Some prior results on polarization properties of the Zn-IV-nitrides have also been reported. Paudel *et al.* [97] calculated stiffness tensors, spontaneous polarization, and piezoelectric coefficients. They reported spontaneous polarization values for $ZnSnN_2$, $ZnGeN_2$, and $ZnSiN_2$ between -0.022 Cm^{-2} and -0.029 Cm^{-2} and concluded that, since differences between these values are markedly smaller than between III-N compounds, polarization-induced electric fields would be significantly suppressed at heterostructures between II-IV-nitrides. However, these spontaneous polarization values were calculated referenced to a zinc-blende (zb) structure. Recent work on wz nitrides has demonstrated that differences in spontaneous polarization values referenced to the zb structure require corrections to account for lattice-parameter differences [33]. Such corrections were not included in the work of Ref. [97]. In the present work, we evaluate the spontaneous polarization values for the Zn-IV-nitrides using a proper centrosymmetric reference [33]. We also perform calculations of the proper piezoelectric constants and the stiffness tensors to generate a consistent set of parameters.

Our results allow us to determine the magnitude of polarization charges at Zn-IV-nitride/III-nitride heterostructure interfaces. Using these polarization properties, along with our calculated band alignments, we can identify interfaces with significantly reduced polarization charge, as well as interfaces with increased polarization charge that are favorable for applications in electronic devices.

7.2 Computational Methods

Our calculations are performed using DFT with the HSE hybrid functional, as described in Sec. 1.3 and 3.2. In this chapter, we also calculate properties of GaN in the wurtzite structure. For GaN, we adjust the HSE mixing parameter to reproduce the experimental band gap; at 29.5% we obtain a band gap of 3.48 eV. Calculations on the primitive unit cell of GaN were performed using a Γ-centered $6 \times 6 \times 8$ grid.

We perform slab calculations to align eigenvalues of the system to the vacuum level. Our bulk calculations report the eigenvalues relative to the electrostatic potential average of the system, and the slab calculations can be used to align the electrostatic potential to the vacuum level. For our slab calculations, we use a $8 \times 1 \times 1$ slab in a supercell geometry, separated by 20 Å of vacuum, and a $1 \times 4 \times 4$ Monkhorst-Pack k-point grid. Calculations for GaN were performed using slabs with nonpolar $(1\bar{1}00)$ (m-plane) surfaces. For the Zn-IV-nitrides we use (100) slabs which are also nonpolar and analogous to the m plane in III-nitrides.

Valence-band alignments are calculated based on the VBM in each material. To determine the band alignments between Zn-IV-nitrides and III-nitrides, we first determine alignments to GaN, then use the results of Moses *et al.* [96] to align to AlN and InN. Note that in Ref. [96] alignments were expressed for an *average* of the top three valence bands; we have combined those values with values of crystal-field splitting to obtain the

VBM positions reported in the present work.

We also examine the band alignments with reference to the $(+/-)$ charge-state transition level of interstitial hydrogen (H_i). This method has been successfully used to align the band gaps of a variety of semiconductors, including the III-nitrides [21]. The position of $H_i(+/-)$ is calculated using formation energies as discussed in Chapter 4.

7.3 Results

7.3.1 Band alignments

Surface calculations

In Table 7.1, we list the VBM and CBM with respect to the vacuum level as obtained from surface calculations in which the atomic positions are not relaxed; effects of atomic relaxation are discussed below. Conduction-band positions for the III-nitrides are obtained based on E_{VBM} and the experimental band gaps. These results allow us to determine the band alignments shown in Fig. 7.1. The band offsets between the three Zn-IV-nitrides are "type I", i.e., the band edges of the material with the smaller gap lie within the band gap of the material with the larger gap, similar to how the III-nitrides are aligned. Between $ZnGeN_2$ and GaN, there is a type-II alignment: the VBM and CBM of $ZnGeN_2$ are both lower in energy than the corresponding bands in GaN.

We investigated atomic relaxations and found them to have only a small effect on alignments. Allowing the atoms in the slab to relax resulted in a lowering of the average electrostatic potential within the slab by 0.1-0.2 eV for all three Zn-IV-nitrides. We also examined alignments based on slabs with a different orientation, namely (010), a nonpolar surface analogous to $(11\bar{2}0)$ (a plane) in the III-nitrides. For this surface orientation the average electrostatic potential in the slab is systematically slightly higher (by up to 0.14

eV) than for the (100) surface. Relaxation of the atoms for the (010) surface results in a larger shift of the electrostatic potential than for (100): a lowering by 0.30±0.05 eV is found for each of the Zn-IV-nitrides. These effects are consistent with the 0.30±0.01 eV reduction in the electrostatic potential upon relaxation for GaN and InN surfaces found by Moses *et al.* [96] The differences are systematic, and as a result very similar band alignments are obtained irrespective of whether relaxed or non-relaxed surfaces are used in the calculations.

	$ZnSnN_2$	$ZnGeN_2$	$ZnSiN_2$	InN	GaN	AlN
E_{CBM}	−4.48	−3.40	−1.95	−5.04	−2.82	−0.60
E_{VBM}	−5.88	−6.59	−6.78	−5.69	−6.30	−6.76
$\mathrm{H}_i(+/-)$	−3.33	−3.46	−3.34	...	−3.58	...

Table 7.1: Position of the valence-band maximum E_{VBM} and conduction-band minimum E_{CBM} with respect to the vacuum level as obtained from surface calculations for nonpolar (100) Zn-IV-nitride and $(1\bar{1}00)$ GaN surfaces. InN and AlN values are from Ref. [96]. The $\mathrm{H}_i(+/-)$ was calculated relative to the VBM and then combined with the E_{VBM} values to obtain a position relative to the vacuum level. All values are in eV.

In Table 7.1 and Fig. 7.1 we combine this information with the positions of the valence-band edges obtained from surface calculations. Among the Zn-IV-nitrides, the position of the $\mathrm{H}_i(+/-)$ level varies by only 0.1 eV on an absolute energy scale, showing that alignment based on the $\mathrm{H}_i(+/-)$ level is very consistent with the alignment based on surface calculations.

Comparison with previous calculations

The band alignment between $ZnSnN_2$ and GaN has been calculated by two other groups, using a superlattice geometry: Wang *et al.* [57] found a VB offset of –0.39 eV, while Punya *et al.* [93, 94] calculated a VB offset of –1.4 eV. Our calculated offset of –0.42 eV is very close to the value reported by Wang *et al.*, but disagrees with the Punya

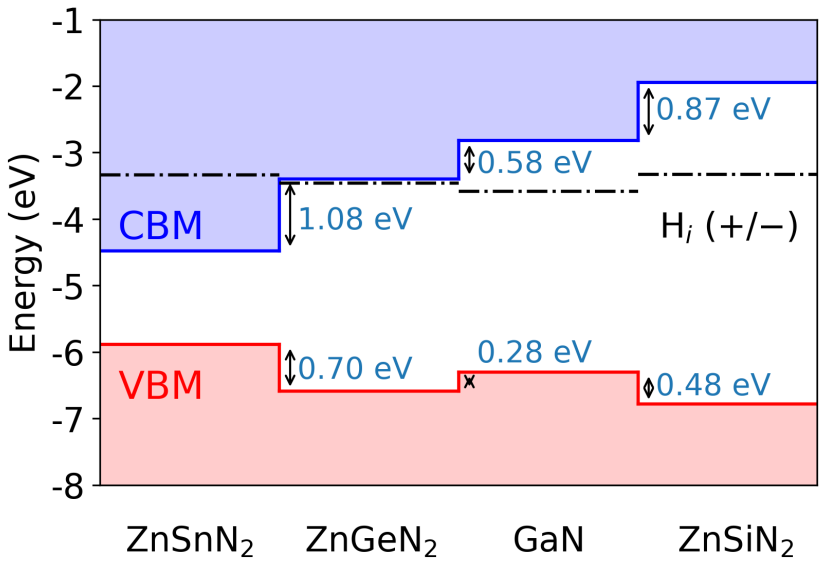

Figure 7.1: Band alignments between Zn-IV-nitrides and GaN, shown on an absolute energy scale where zero is the vacuum level.

et al. result by 1.0 eV. Punya *et al.* also reported the VBM of $ZnGeN_2$ to be 1.1 eV higher than that of GaN, while we find the VBM of $ZnGeN_2$ to be 0.28 eV lower than that of GaN: a difference of 1.4 eV.

The difference with the results of Punya *et al.* is likely due to the difference in computational approach. While we (and Wang *et al.* [57]) use the HSE functional, Punya *et al.* used the LDA functional and applied a correction based on *GW* calculations. It is known that *GW* results can depend on the accuracy of the DFT calculations used as a starting point.

Based on superlattice calculations for cubic $ZnGeN_2$/GaN Cao *et al.* [95] found a VB offset of −0.38 eV, a difference of 0.70 eV from our results. The discrepancy here is likely due to the fact they are evaluating the (001) interface for cubic material, i.e., a different interface and crystal structure from what we evaluate here.

7.3.2 Polarization

Spontaneous polarization

The Zn-IV-nitrides have an orthorhombic unit cell, with space group $Pna2_1$ and point group $mm2$. $Pna2_1$ is a polar space group that has two glide planes, and as such it has two nonpolar axes and one polar axis. The direction along the polar axis is labeled the c direction, consistent with the notation for the wz III-nitrides. We calculate the spontaneous polarization along this polar axis.

As explained in Sec. 2.2, the effective spontaneous polarization is the difference between the formal polarization of the orthorhombic structure and the formal polarization of a reference structure, for which we choose the centrosymmetric $Pnma$ structure. The effective spontaneous polarization values for the Zn-IV-nitrides are listed in Table 7.2.

	$ZnSnN_2$	$ZnGeN_2$	$ZnSiN_2$
P_{SP}	1.184	1.333	1.433
P_{SP}(zb ref)	−0.033	−0.027	−0.029
P_{SP}(zb ref), Ref. [97]	−0.029	−0.023	−0.022

Table 7.2: Calculated effective spontaneous polarization constants of the Zn-IV-nitrides. Also listed are the spontaneous polarization values calculated with respect to a zb reference as obtained in the present work, and compared with values from Ref. [97]. All values in Cm^{-2}.

In Fig. 7.2, we plot the spontaneous polarization for the III-nitrides and the Zn-IV-nitrides as a function of lattice parameter. For the Zn-IV-nitrides, we use $a_{\mathrm{wz}} = \sqrt{\frac{ab}{2\sqrt{3}}}$ to define a wurtzite-equivalent lattice parameter. To determine the spontaneous polarization of alloys, we first convert to the reduced units of $\frac{ec}{\Omega} = e/A_{\mathrm{int}}$ (the quantum of polarization), where $A_{\mathrm{int}} = \sqrt{3}a_{\mathrm{wz}}^2$ is the area of the base of the wz unit cell [drawn in Fig. 1.1]. In these units, we interpolate the spontaneous polarization linearly, then convert back to Cm^{-2}. This method accounts for the areal dependence of the polarization. The arguments for interpolating in this manner are explained in Sec. 2.5.

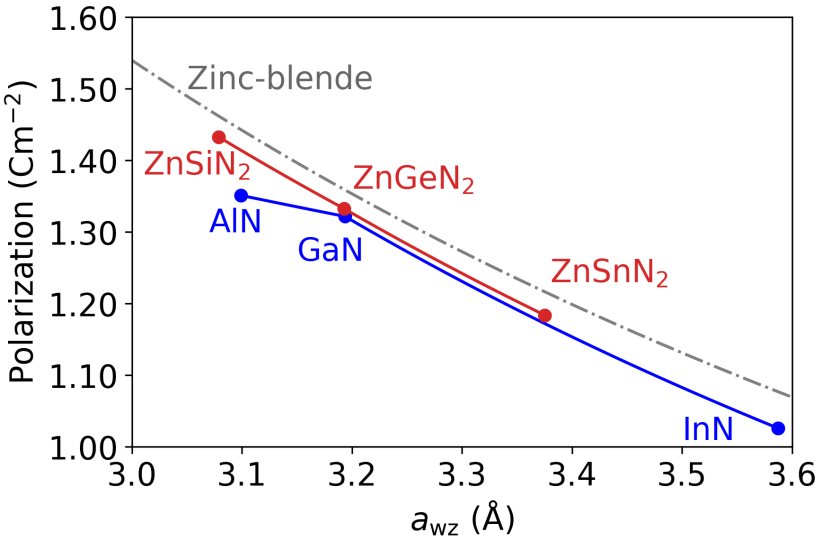

Figure 7.2: Spontaneous polarization for the III-nitrides and the Zn-IV-nitrides, as a function of wurtzite-equivalent in-plane lattice parameter a_{wz}. The values for a zinc-blende structure are also indicated.

Our calculations indicate that the spontaneous polarization values of $ZnGeN_2$ and GaN are quite similar. More generally, the spontaneous polarization of $ZnSnGeN_2$ alloys and InGaN alloys is very similar at the same lattice parameter. Interestingly, there is a significant spontaneous polarization difference between $ZnSiGeN_2$ and AlGaN.

Paudel *et al.* [97] previously calculated spontaneous polarization constants for the Zn-IV-nitrides, reporting values in the narrow range of –0.022 Cm^{-2} to –0.029 Cm^{-2}. However, they used a zb structure as their reference. In Fig. 7.2 we also show the formal polarization (along the [111] axis) for a zb structure. For zb, the magnitude of the appropriate branch of the formal polarization is $\mathbf{P}_{\mathrm{f}}^{\mathrm{zb}} = e\sqrt{3}/2a_{\mathrm{wz}}^2$ (see Ref. [33]), which is equivalent to $\frac{3e}{4A_{\mathrm{int}}}$; i.e., the value for zb depends only on the lattice parameter. This allows us to express our spontaneous polarization values with respect to a zb reference; the values are shown in Table 7.2, and compared to the values reported in Ref. [97]. Reasonable agreemeent is found.

We caution against using spontaneous polarization values referenced to zb. Each

material has different lattice parameters for the zb reference structure, which leads to additional terms in polarization differences calculated at an interface (due to the fact that the formal polarization of zb is nonzero) [33]. Those terms have not been properly included in conventional simulations. When the centrosymmetric structures (which have zero formal polarization) are used as the reference, additional terms are not necessary.

Piezoelectric polarization

For piezoelectric polarization, there are five nonzero piezoelectric tensor elements for orthorhombic materials with the $mm2$ point group [35]. We calculate the proper piezoelectric coefficients, $e_{ij} = \frac{dJ_i}{d\dot{\epsilon}_j}$, where J_i is the current density that flows through the bulk of the material in response to a slow deformation $\dot{\epsilon}_j = d\epsilon_j/dt$, and ϵ_j is a strain. For purposes of calculating polarization differences at pseudomorphic interfaces between two semiconductors, *improper* piezoelectric coefficients should be used [33, 34]. Here we calculate the proper piezoelectric coefficients because they are branch-independent and can be compared to experimental values [34]. Improper coefficients are related to the proper coefficients by expressions that involve the zero-strain (spontaneous) formal polarization [33, 34]. The improper piezoelectric constants e_{31} and e_{32} are related to the respective proper constants by

$$e_{3i}^{imp} = e_{3i}^{prop} - P_{\mathrm{SP}}, \tag{7.1}$$

while the improper coefficient e_{33}^{imp} is the same as the proper coefficient. Our calculated proper piezoelectric constants are listed in Table 7.3. The values of e_{31} and e_{32} are close to the values of e_{31} in the III-nitrides, while the values of e_{33} are significantly smaller than the values of e_{33} for the III-nitrides [33].

Elastic constants are also required to calculate piezoelectric polarization at pseudo-

	$ZnSnN_2$	$ZnGeN_2$	$ZnSiN_2$
e_{15}	−0.307	−0.302	−0.279
e_{24}	−0.286	−0.262	−0.241
e_{31}	−0.397	−0.378	−0.386
e_{32}	−0.403	−0.299	−0.305
e_{33}	0.825	0.666	0.692

Table 7.3: Calculated proper piezoelectric polarization constants for the Zn-IV-nitrides. All values in Cm^{-2}.

morphic interfaces. Calculated elastic constants are listed in Table 7.4. The values are in good agreement with previously published calculations [97]. Elastic parameters for the III-nitrides have been taken from Ref. [50].

	$ZnSnN_2$	$ZnGeN_2$	$ZnSiN_2$
C_{11}	270	342	403
C_{22}	255	330	372
C_{33}	285	385	467
C_{23}	91	103	119
C_{13}	93	98	101
C_{12}	115	138	150
C_{44}	67	97	124
C_{55}	63	87	104
C_{66}	73	108	138

Table 7.4: Calculated elastic constants of the Zn-IV-nitrides. All values in GPa.

Polarization charges at interfaces

Polarization differences between materials manifest in interface charges at a heterojunction. For an interface normal to the c axis the interface charge σ_b can be calculated based on the polarization properties and the elastic constants [33]:

$$\sigma_b = P^m_{\mathrm{SP}} - P^n_{\mathrm{SP}} - \sum_{i=1,2} \epsilon^n_i (e^n_{3i} - P^n_{\mathrm{SP}} - e^n_{33} C^n_{i3}/C^n_{33}) \,. \tag{7.2}$$

Here we assume that material n is strained coherently to material m (i.e., m is the substrate, or a layer much thicker than n) and grown along the $+c$ axis. We will denote such a interface as n/m. P_{SP} is the spontaneous polarization, ϵ_i are the strain components, e_{ij} are the piezoelectric coefficients, and C_{ij} are the elastic constants. Parameters for AlN and InN were taken from Ref. [33]. Elastic parameters for the III-nitrides have been taken from Ref. [50].

Unlike the III-nitrides, the Zn-IV-nitrides exhibit an anisotropy in lattice parameters perpendicular to the c axis (see Table 3.1). A $ZnGeN_2$ layer strained to a c-plane GaN substrate experiences a tensile strain ϵ_1 in the [100] direction, but compressive strain ϵ_2 in the [010] direction. The in-plane lattice parameters can be visually compared in Fig. 3.2. The strain ϵ_3 in the direction normal to the interface can be calculated using the elastic constants (Table 7.4). Each of these strains ϵ_j produces a piezoelectric effect along the c direction with coefficient e_{3j}.

In Fig. 7.3, we plot the total (spontaneous + piezoelectric) polarization for Zn-IV-nitrides strained to wz substrates with a given lattice parameter a_{wz}. Units of e/A_{int} are chosen for clarity of visualization, since the polarization differences are more difficult to discern when expressed in units of Cm^{-2} (as evident from Fig. 7.2). The total polarization lines extend up to $\pm 2\%$ average planar strain (note that the strains along a and b axes are different; this anisotropy is taken into account in the calculation of the piezoelectric polarization). The differences in polarization values between the unstrained III-nitrides (blue line) and the strained Zn-IV-nitrides (green lines) at the same lattice parameter are precisely the bound charges at an interface between the two materials, in accordance with Eq. (7.2).

For $ZnGeN_2$ strained to GaN the total polarization difference is 0.0052 e/A_{int} or 5.9×10^{12} e/cm^2. This interface exhibits a very small net piezoelectric effect, as $ZnGeN_2$ strained to GaN is slightly tensile strained along the a axis, and slightly compressed along

the b axis. The total polarization difference is thus primarily a result of the difference in the spontaneous polarization values. Similarly, the differences in polarization values between the strained III-nitrides (purple lines) and unstrained II-IV-nitrides (red line) correspond to bound charges at an interface between the two materials. To identify an interface with zero polarization difference, we would look for a point where the blue and green lines intersect; this happens, e.g., for an interface between strained $ZnGeN_2$ and $In_{0.09}Ga_{0.91}N$.

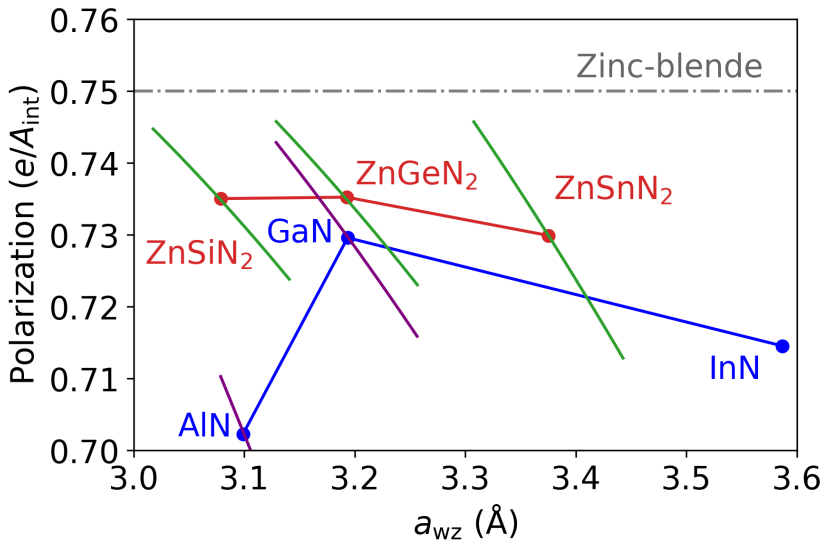

Figure 7.3: Green lines denote total polarization for $ZnSiN_2$, $ZnGeN_2$, and $ZnSnN_2$ strained to wurtzite as a function of in-plane lattice parameter. Purple lines total polarization for AlN and GaN strained to orthorhombic $ZnSi_xGe_{1-x}N_2$ and $ZnGe_xSn_{1-x}N_2$, plotted as a function of wurtzite-equivalent lattice parameter. Spontaneous polarization values for II-IV-nitrides are in red and for III-nitrides in blue.

The anisotropic in-plane strain at the $ZnGeN_2$/GaN interface distinguishes it from conventional III-nitride interfaces. The piezoelectric polarization from the strain along the a axis mostly cancels the effect along the b axis, leaving the spontaneous polarization as the primary contribution to the interface charge at the interface. This is in contrast to III-nitride interfaces, where the piezoelectric effect dominates over the spontaneous polarization.

7.4 Prospects for polarization engineering with Zn-IV-nitrides

7.4.1 Light emitters

We now examine, based on our calculated values of band alignments and polarization constants, specific structures which could improve the light-emission efficiency of nitride quantum wells. The cases discussed here are only examples of the rich space that is opened up by integrating the Zn-IV-nitrides with III-nitrides. *c*-plane devices lead to strong polarization fields, which separate electrons and holes in the quantum well and reduce radiative recombination. To overcome the Stark effect, the use of nonpolar or semipolar orientations has been proposed [100, 101], but growth in those orientations tends to be harder to control than for the *c* plane.

An alternative approach is the use of *c*-plane heterostructures with interfaces that minimize the polarization charge. In Fig. 7.3, we showed that a $ZnGeN_2$ layer strained to $In_{0.09}Ga_{0.91}N$ results in an interface with zero polarization charge. The choice of substrate has only a minor effect on the required composition to achieve zero polarization charge: a $ZnGeN_2/In_{0.07}Ga_{0.93}N$ interface strained to GaN would also have zero polarization charge. These zero-polarization charge structures are not possible within the InGaN ternary system alone.

Minimizing polarization fields is only one aspect of enhancing light emission; the heterostructure also needs to provide adequate confinement for electrons and holes in a quantum well. In Fig. 7.4, we plot the band offsets between $ZnGeN_2$ and ternary III-nitrides; a positive value indicates the band edge of the III-nitride is higher in energy than that of $ZnGeN_2$. For concentrations of In lower than 24%, the CB of InGaN is above the CB of $ZnGeN_2$, indicating that there will be no quantum confinement for electrons

in the InGaN quantum well. This means that the heterostructure with zero polarization charge (with $< 24\%$ In) cannot be directly used for a quantum-well device. Electron confinement would require In concentration higher than 24%.

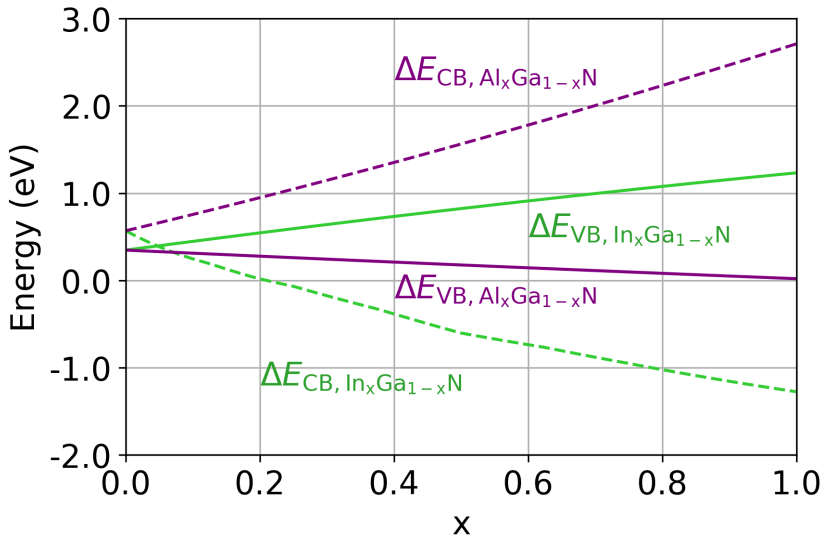

Figure 7.4: CB and VB offsets for AlGaN and InGaN layers relative to the CBM and VBM of $ZnGeN_2$. Band bowing parameters for InGaN are from Ref. [96] and for AlGaN from Ref. [102]. Strain effects are taken into account using deformation potentials from Refs. [103] and [104].

Finally, we comment on proposals for optoelectronic device structures incorporating Zn-IV-nitrides in InGaN quantum wells [38, 39, 105]. The aim was to counteract the Stark effect by confining holes in a thin $ZnGeN_2$ layer. Such confinement of holes will occur only if the $ZnGeN_2$ valence band lies above the VBM in the III-nitride alloy. The simulations of Ref. [38], [39], and [105] relied on the values calculated by Punya *et al.* [93, 94], which show a large and negative value for the $ZnGeN_2$/GaN VB offset (–1.1 eV). As discussed in Sec. 7.3.1, our present calculations show that this is not the case; i.e., we find the $ZnGeN_2$/GaN VB offset to be positive. Therefore the Zn-IV-nitride layer is not able to confine holes, thus casting doubt on these predictions.

7.4.2 Transistors

For electronic applications, enhanced interfacial polarization charge can be beneficial since it allows achieving higher carrier densities [3]. If $ZnSiN_2$ can be grown with sufficiently high quality, forming heterostructures with AlGaN could be advantageous both for electron confinement and for enhanced polarization. Our calculations indicate that the CBM of $ZnSiN_2$ is 1.6 eV below that of AlN, while the VBM of $ZnSiN_2$ is only slightly lower than that of AlN. The large CB offset is beneficial for the two-dimensional electron gas at a $ZnSiN_2$ strained-to-AlN interface. We find the polarization charge to be -3.5×10^{13} cm^{-2} at the $ZnSiN_2$/AlN interface, which is comparable to an interface between GaN and $Al_{0.5}Ga_{0.5}N$. This high polarization charge and large band offset makes $ZnSiN_2$ an interesting material for electronic applications.

7.5 Summary

We have performed a comprehensive study of band alignments and polarization properties of heterostructures between the Zn-IV-nitrides and the III-nitrides. Values for spontaneous and piezoelectric polarization coefficients are reported. We have demonstrated that the Zn-IV-nitrides allow for new combinations of polarization and band gap, which might enable novel device structures. We have identified zero-polarization-charge interfaces between Zn-IV-nitrides and III-nitrides; however these structures cannot be used for quantum-well devices due to the band offsets. For electronic devices, $ZnSiN_2$/AlN interfaces exhibit a larger conduction-band offset and polarization charge than AlGaN/GaN, thus allowing for potentially higher electron sheet densities. The cases discussed are only examples of the space that is opened up by integrating the Zn-IV-nitrides with III-nitrides; our study will enable full exploration of this space.

Chapter 8

Polarization at the rocksalt-wurtzite interface

This work was done in collaboration with Cyrus E. Dreyer and Chris G. Van de Walle.

8.1 Introduction

ScN is a semiconducting nitride that takes the rocksalt crystal structure, and can be integrated with the technologically interesting III-nitride family of compounds. Recently, a great deal of attention has been focused on alloys of ScN and AlN, which exhibit enhanced piezoelectricity at Sc concentrations up to 43% [106] and ferroelectricity at Sc concentrations between 27 and 43% [107]. Pure rocksalt ScN has attracted interest for its low lattice mismatch to GaN; grown along the [111] direction it exhibits a mismatch of less than 1% with *c*-plane GaN [108]. ScN grown by molecular beam epitaxy has been examined as a potential buffer layer for improving the quality of heteroepitaxial GaN [109, 110]. However, questions still remain about properties of the pristine interface, as electrical characterization has only been conducted on polycrystalline films [111] or on

films with oxide contamination at the interface [108].

Interfaces between wurtzite III-nitrides have charges induced by polarization differences [3]. These polarization charges are desirable in power electronics, where they result in large two-dimensional electron and hole gases (2DEGs and 2DHGs) [112, 113]. Polarization can also be utilized to enhance the field in tunnel junctions [114, 115, 116]. Current tunnel structures are based on a GaN *p*-*n* junction with a thin AlGaN or InGaN interlayer that creates a strong polarization field across the depletion region. High Al or In content is desirable to increase the field strength and reduce the width of the depletion region, but the alloy composition is constrained by strain considerations [10].

Here we use density functional theory and the modern theory of polarization to demonstrate that a large polarization sheet charge with magnitude 1.358 Cm^{-2} will exist at the ScN/GaN interface. We clarify that the reason for this charge is not a result of the naïve expectation that, since rocksalt (rs) is centrosymmetric (space group $Fm\bar{3}m$), it has no polarization [35], while wurtzite (wz) GaN has a large spontaneous polarization. In fact, rs-ScN has a nonvanishing *formal* polarization [29] along the [111] direction that must be taken into account when calculating polarization differences that lead to bound charges at the interface. This is confirmed by comparing to explicit superlattice calculations. Based on the large polarization discontinuity, we will propose potential applications of ScN interfaces.

8.2 Bulk properties

ScN has the rocksalt structure, which consists of two interpenetrating face-centered cubic lattices. Using the 2-atom primitive unit cell of ScN, we calculate the lattice parameter to be a_{ScN}=4.48 Å (which corresponds to an in-plane wurtzite equivalent of 3.17 Å) with an indirect band gap of 0.80 eV, in agreement with experimental values [117].

We find that the electric contribution to the polarization of ScN is particularly sensitive to the k-point grid; we report the formal polarization of ScN from a finer $15 \times 15 \times 15$ k-point grid. The lattice parameters of GaN are a_{GaN}=3.20 Å and c_{GaN}=5.20 Å, with a direct band gap of 3.18 eV.

All of our calculations are done using the HSE hybrid functional with 25% mixing. Note that this is different from the previous chapter, where calculations for GaN used a higher mixing of 29.5% in order to reproduce the experimental band gap. We are forced to choose a single HSE mixing parameter for the purpose of performing the ScN/GaN superlattice calculations. The use of 25% mixing causes an underestimation of the GaN band gap (experiment: 3.51 eV, Ref. [50]); however, we have verified that this does not affect the quantities extracted from the superlattice calculations [118], nor the accuracy of calculated polarization values.

Our rs-ScN structure is relaxed using a $7 \times 7 \times 7$ Γ-centered grid. We find that the electronic contribution to the polarization of ScN is particularly sensitive to the k-point grid; we report the formal polarization of ScN based on a finer $15 \times 15 \times 15$ k-point grid. Our GaN structure is calculated using a Γ-centered $6 \times 6 \times 8$ grid, as in Chapter 7.

The rocksalt structure has a center of symmetry. As discussed in Sec. 2.1, within the modern theory of polarization formal polarization is defined only modulo the quantum of polarization. For the rocksalt structure, this means that there are two set of vectors that satisfy the symmetry of the structure: $\frac{e}{\Omega}\mathbf{R}$ or $\frac{e}{\Omega}[\mathbf{R} + a_{\mathrm{rs}}(\frac{1}{2}, \frac{1}{2}, \frac{1}{2})]$, where a_{rs} is the rocksalt lattice parameter. From explicit evaluation of Eq. (2.6) we find that ScN has the formal polarization $\frac{e}{\Omega}[\mathbf{R} + a_{\mathrm{rs}}(\frac{1}{2}, \frac{1}{2}, \frac{1}{2})]$.

In order to properly define polarization differences, we also need to choose a reference structure. For wurtzite, the layered hexagonal structure (h-GaN) has centrosymmetry (space group $P6_3/mmc$) and serves as a convenient reference structure [33]. It is derived from wurtzite by considering planes of atoms along the polar axis and moving the cations

into the plane of the anions, resulting in a centrosymmetric structure with zero $\mathbf{P}_{\mathrm{f}}$ [33]. The formal polarization of GaN is approximately linear as a function of the wurtzite internal parameter u_{wz}, which is defined as the ratio of the Ga–N bond length along the c axis to the c lattice parameter. The equilibrium structure of GaN has $u_{\mathrm{wz}} = 0.377$, whereas layered hexagonal has $u_{\mathrm{wz}} = 0.5$.

Similar to wurtzite [0001], rocksalt in the [111] direction has alternating planes of cations and anions [see Fig. 8.1(c)]. However, the stacking sequence is $ABCABC$, as opposed to $ABAB$ in wurtzite. We follow a similar strategy to obtain a reference structure as we did for wurtzite: moving the cations into the plane of the anions creates the face-centered cubic analog of the $P6_3/mmc$ GaN structure [Fig. 8.1(a)]. Unlike $P6_3/mmc$, this layered version of rocksalt (space group $R3m$) is not centrosymmetric and therefore symmetry does not dictate that its formal polarization should be zero; however, since each layer is charge neutral, we expect the polarization of this structure to be very small, as will indeed be confirmed by explicit calculations.

To generalize u_{wz} to a parameter that can be used with both wurtzite and rocksalt structures, we define δ as the ratio of the separation between planes of anions and cations to the separation between planes of cations; with this definition, $\delta = 1 - 2u_{\mathrm{wz}}$ for the wurtzite structure. The layered structures, in which the anions and cations lie in the same plane, have $\delta = 0$. Ideal wurtzite has $\delta = 0.25$, and bulk GaN has $\delta = 0.245$ along the c axis. The rocksalt structure [Fig. 8.1(c)] has $\delta = 0.5$ along the [111] axis. We find that the formal polarization is approximately linear in δ.

In Fig. 8.1(d), we plot a branch of the formal polarization of ScN and GaN as a function of δ. The branches are chosen so that h-GaN has zero formal polarization, and $\delta = 0$ ScN has a formal polarization close to zero. Our calculated formal polarization of rs-ScN along the c axis is $\frac{e a_{\mathrm{rs}}}{\Omega} \| (\frac{1}{2}, \frac{1}{2}, \frac{1}{2}) \| = 2.731$ Cm^{-2}, while the formal polarization of layered ScN is -0.064 Cm^{-2}. The calculated formal polarization of wz-GaN is 1.315

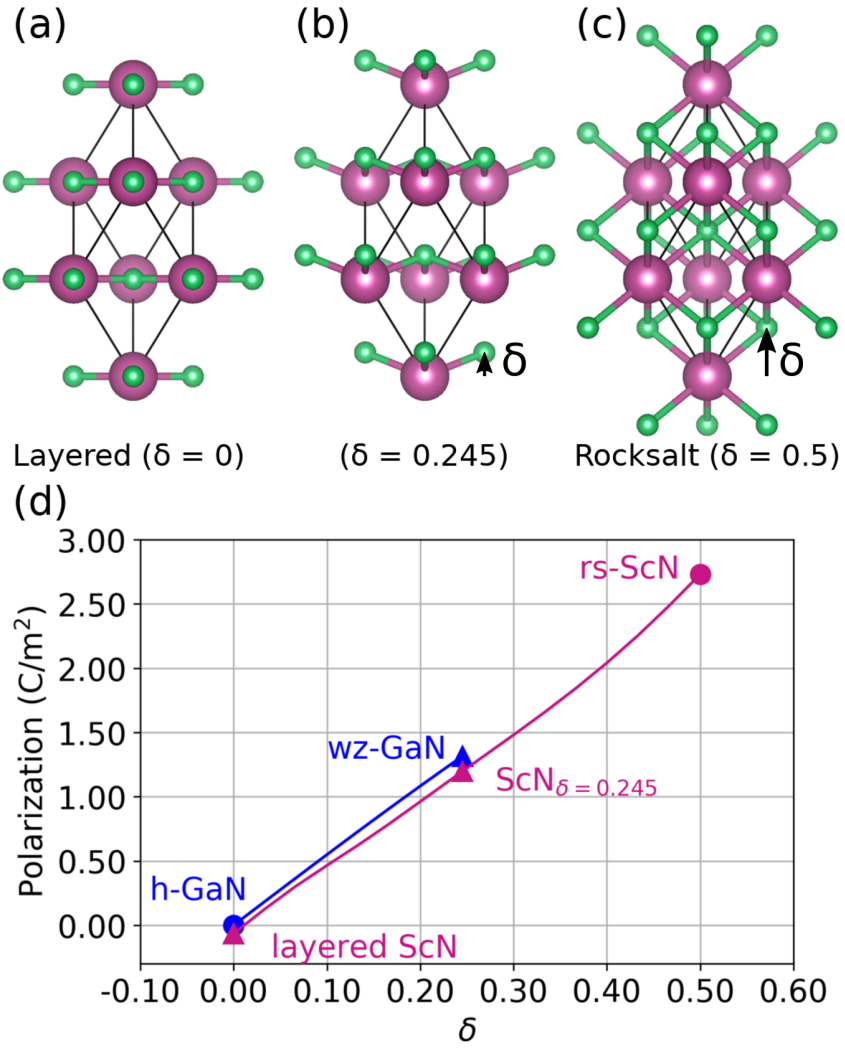

Figure 8.1: ScN in the (a) layered, (b) $\delta = 0.245$, and (c) rocksalt crystal structures. Unit cells are indicated by black lines. (c) Calculated formal polarization as a function of the δ parameter. For ScN, the lattice parameters are held at the rs-ScN values, while for GaN the lattice parameters are held at the wz-GaN values. The circles indicate centrosymmetric structures.

Cm^{-2}. According to the modern theory of polarization [31], differences between formal polarization of two structures A and B are physically meaningful if a gap-preserving deformation exists between A and B; we have verified that the deformations as a function of δ are all gap-preserving, for both GaN and ScN.

8.3 Polarization differences

Our goal is to determine the bound polarization charge at an interface between wz-GaN in the [0001] direction and rs-ScN in the [111] direction. The formal polarizations are only defined modulo a quantum of polarization, as discussed in Sec. 2.1. Specifically, Eq. (2.7) is modulo e/A_{int} [31], where A_{int} is the unit cell area of the interface. To resolve the ambiguity, we need to select a specific branch of the formal polarization for each material. We will do this by choosing a reference structure for each of the two materials that allows connecting them at the specific interface under study.

As mentioned before, the lattice mismatch between rs-ScN and wz-GaN is quite small; however, if we consider the ScN to be strained coherently to GaN, there will be a small piezoelectric contribution to the interface charge. Rocksalt, being centrosymmetric, has no "proper" (in the sense of Ref. [34]; see Sec. 2.4) piezoelectric response; however, strain in the (111) plane will dilute or concentrate the zero-strain formal polarization, and thus there will be an "improper" contribution [34], given by $-2\epsilon P_{\mathrm{f}}^{\mathrm{ScN}}$, where ϵ is the strain induced by the lattice mismatch in the (111) plane, $\epsilon = (a_{\mathrm{ScN}}/\sqrt{2} - a_{\mathrm{GaN}})/a_{\mathrm{GaN}}$. We calculate this piezoelectric contribution to be -0.058 Cm^{-2}. The polarization charge at the interface can then be calculated using

$$\sigma_b = P_{\mathrm{f}}^{\mathrm{GaN}} - (1 - 2\epsilon) P_{\mathrm{f}}^{\mathrm{ScN}} \tag{8.1}$$

and the predicted polarization difference of rs-ScN coherently strained to wz-GaN is $\sigma_{\rm b} = 1.315 - (2.731 - 0.058) = -1.358$ Cm^{-2}, corresponding to a bound charge with magnitude 8.5×10^{14} cm^{-2}. This value is over an order of magnitude larger than the bound charge at interfaces between, e.g., GaN and AlN.

In order to predict this bound charge based on differences between formal polarization values calculated for wz-GaN and rs-ScN, we applied the interface theorem [Eq. (2.7)]. Application of this theorem requires that the interface is insulating; we verify this by performing explicit superlattice calculations, in which the ScN layer is strained to the in-plane lattice parameters of GaN (but allowing all internal coordinates to relax). The layer-resolved density of states (DOS) is shown in Fig. 8.2(a). Strong electric fields are present, due to the large polarization charges at the interfaces. The fields are so large that the resulting voltage drop across the ScN layer exceeds the band gap (no matter how thin we make this layer), leading to charge transfer between the interfaces. Though the presence of mobile charges at the interfaces results in a non-insulating cell, the essential feature in the layered DOS is the presence of a band gap in each of the layers; therefore, the interface itself is insulating and our use of the interface theorem is justified.

In principle, the electric fields present in the superlattice should be quantitatively consistent with our calculation of bound interface charges based on differences of polarization quantities determined for bulk wz-GaN and rs-ScN. However, the presence of mobile charge complicates a direct comparison. It also precludes a direct verification of our choice of branches when calculating formal polarization differences based on bulk values [Fig. 8.1(d)]; indeed, the large polarization charge is on the same order as the quantum of interface polarization, ($e/A_{\rm int} = 1.803$ Cm^{-2}). We will address this by performing superlattice calculations between structures of GaN and ScN that give rise to smaller polarization differences; these structures are based on different values of the interlayer spacing δ [Fig. 8.1(d)].

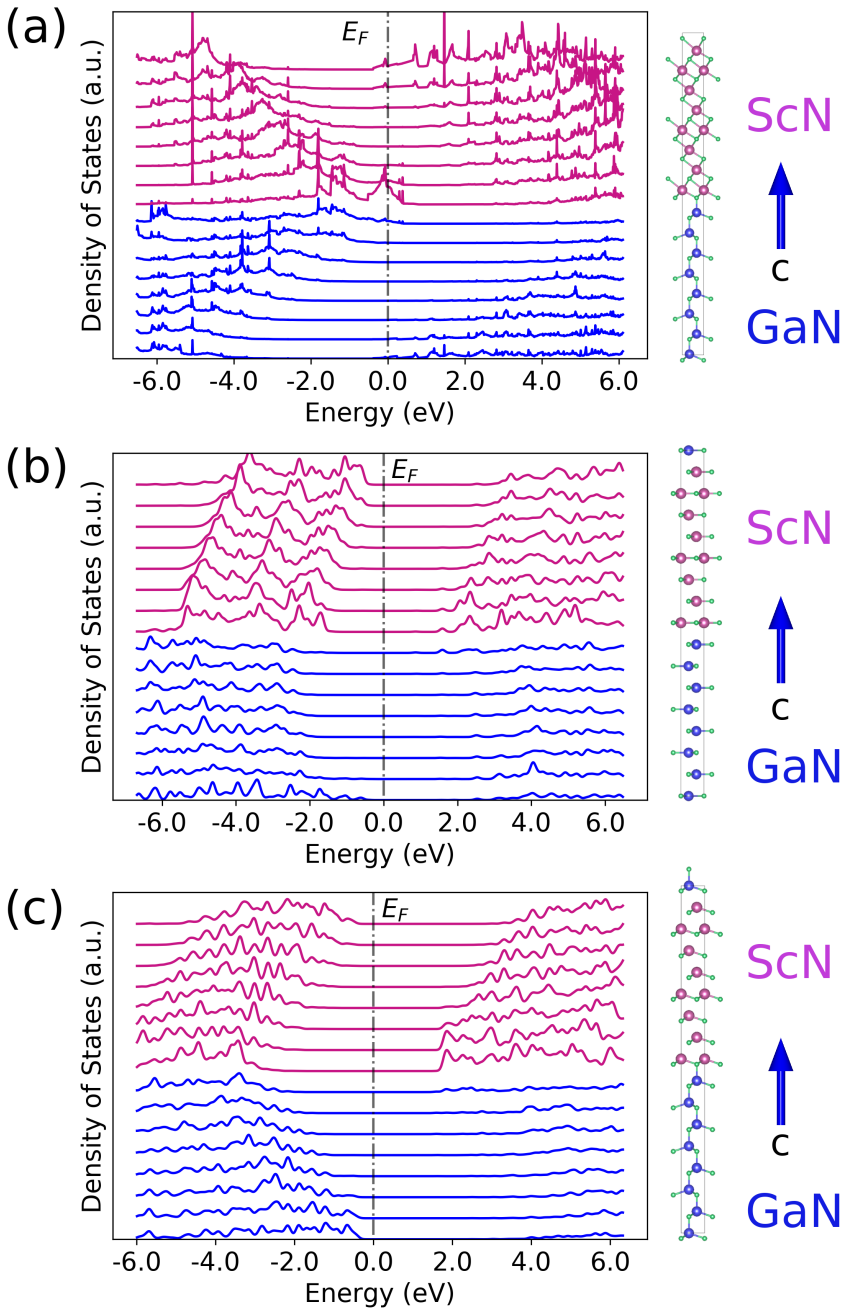

Figure 8.2: Layer-resolved density of states for GaN/ScN superlattices with (a) wz–GaN/rs-ScN, (b) $\delta = 0$, and (c) $\delta = 0.245$. The superlattice structure is illustrated to the right, with Ga atoms in blue, Sc atoms in purple, and N atoms in green.

First, we construct a superlattice for the $\delta = 0$ structures, i.e., between h-GaN and the layered ScN structure [Fig. 8.1(a)]. Based on the formal polarization values in Fig. 8.1(d), and accounting for the improper piezoelectric effect (since ScN is strained to GaN), we expect a relatively small bound charge of 0.070 Cm^{-2}, at the interface. Indeed, in Fig. 8.2(b), we see that the electric fields are significantly smaller and breakdown is avoided, i.e., the entire superlattice is insulating. The fields in Fig. 8.2(b) are opposite in sign to those in Fig. 8.2(a) as the polarization of layered ScN is smaller than that of h-GaN, whereas the polarization of rs-ScN is larger than that of wz-GaN (see Fig. 8.1).

The electric fields extracted from the superlattice and the theory of linear dielectric media allow us to obtain the *zero field polarization difference* between the layers (i.e., removing the additional polarization from the dielectric response of the layers to the fields in the calculation, see Ref. [119]). By Gauss's law, the electric displacement field is discontinuous across the interface, the discontinuity being equal to the polarization difference:

$$\sigma_b = \varepsilon_0 \varepsilon_r^{\mathrm{ScN}} \mathcal{E}_{\mathrm{ScN}} - \varepsilon_0 \varepsilon_r^{\mathrm{GaN}} \mathcal{E}_{\mathrm{GaN}}, \tag{8.2}$$

where $\mathcal{E}$ is the electric field in each material, ε_0 is the permittivity of free space, and ε_r is the relative permittivity. In the superlattice of the layered structures, the atomic positions are fixed; only the electrons screen the electric field, and the relevant permittivity is the clamped-ion dielectric constant. We calculate clamped-ion dielectric constants of 5.6 for h-GaN and 6.7 for layered ScN.

This procedure produces a bound polarization charge of 0.058 Cm^{-2}, to be compared with the bound charge of 0.070 Cm^{-2} obtained from the difference in formal polarizations. Because these values are much smaller than the quantum of interface polarization, we can be confident that we have chosen the correct branch for the formal polarizations in Fig. 8.1(d).

As an additional test we repeat the procedure for an interface between wz-GaN and ScN with $\delta = 0.245$, with respective clamped-ion dielectric constants of 5.1 and 6.5. The ScN layer is strained to the in-plane lattice parameters of GaN. The results are shown in Fig. 8.2(c). An analysis of the electric fields allows us to extract a polarization charge of 0.121 Cm^{-2} at the interface. This is to be compared with a value of 0.126 Cm^{-2} derived from the formal polarization difference. This again confirms that we have made the correct choice of branch for the polarization charge at the (0001)wz-GaN/(111)rs-ScN interface.

The procedure for determining polarization charge at the (0001)wz-GaN/(111)rs-ScN interface can equally be applied to similar interfaces between rs-ScN and other nitride semiconductors (wz-AlN or wz-InN) for which polarization values are known [33]. Using the value of 2.731 Cm^{-2} for the formal polarization of rs-ScN, and Eq. (8.1) to include the effect of the piezoelectric field, polarization charges between ScN and any wurtzite nitride can then be computed.

8.4 Applications

In the absence of free carriers, breakdown will occur if the potential drop over the ScN layer is larger than the band gap of ScN. For a rs-ScN layer grown on semi-infinite wz-GaN, we can apply Eq. (8.2), setting $\mathcal{E}_{\mathrm{GaN}} = 0$. The electric field in the ScN layer will be $|\sigma_b|/\varepsilon_0\varepsilon_r^{\mathrm{ScN}} = 6.1$ GV/m (using $\sigma_b = -1.358$ Cm^{-2} and our calculated static dielectric constant of 25.0). The critical layer thickness for breakdown to occur is then given by $d_c = E_g/e\mathcal{E} = 1.5$ Å, approximately one monolayer. Therefore, for any thickness of the ScN layer, a 2DEG forms when ScN is grown on the $(000\overline{1})$ GaN interface, and a 2DHG forms on the (0001) GaN interface.

For finite-thickness layers, as the thickness of the GaN and ScN layers increases,

increasing numbers of holes or electrons will appear at the interfaces to compensate the bound polarization charge. As the thicknesses of the GaN and ScN layers increase to infinity, the fields in the layers will vanish, and the free-carrier density at the interface will equal the bound polarization charge density (8.5×10^{14} cm^{-2}).

The hole and electron gases at the GaN/ScN interfaces may be useful for contacts or as current spreading layers, due to the extremely high carrier concentrations. *p*-GaN/ScN/*n*-GaN (grown in the [0001] direction) tunnel junctions are another attractive application. Current tunnel junctions make use of the smaller band gap InGaN interlayers to reduce the effective barrier and increase the polarization field across the *p*-*n* junction to reduce the junction width [115, 116]. ScN is a promising alternative, with a higher polarization field, smaller band gap, and much smaller strain.

8.5 Summary

In summary, we have demonstrated a large polarization difference between ScN and GaN. The polarization difference between rs-ScN and wz-GaN is -1.358 C/m^2 when the formal polarizations are appropriately referenced. This polarization difference produces extremely large bound charges and electric fields, which can be exploited for high-density electron and hole gases with concentrations up to 8.5×10^{14} cm^{-2}, in tunnel junctions.

Chapter 9

Outlook

9.1 Summary

I have investigated the Zn-IV-nitrides and ScN for potential integration with III-nitride devices. I identified that $ZnGeN_2$ can be doped n-type and p-type, implying that diode structures could be formed based on p-n junctions in $ZnGeN_2$. By studying band alignments, I found that $ZnGeN_2$ and GaN form a type-II band offset. These offsets make it more difficult to confine electrons and holes within the same layer in III-nitride/Zn-IV-nitride/III-nitride or Zn-IV-nitride/III-nitride/Zn-IV-nitride quantum wells. The band offsets can be advantageous in the case of devices involving $ZnSiN_2$. $ZnSiN_2$/AlN interfaces exhibit a larger conduction-band offset than AlGaN/AlN interfaces where the AlGaN layer has a similar band gap to $ZnSiN_2$. That, along with a large polarization charge at the interface, can enable higher electron sheet densities in $ZnSiN_2$ layers.

ScN/GaN interfaces exhibit a large polarization discontinuity. The most promising of applications for ScN layers are tunnel junction interlayers, which could be grown very thin with low strain and be a significant improvement over existing InGaN based junctions. The high electron sheet densities also render ScN layers useful as current spreading layers.

I am optimistic the calculations performed in this thesis will inform and motivate work on such devices.

9.2 Future prospects

I am most excited about the potential for further developments based on the work I did in the area of polarization. There are many aspects of my calculations on ScN/GaN interfaces that I believe could be applied to other materials. The most obvious is to look at other combinations of rocksalt and wurtzite materials. There are many semiconducting rocksalt oxides with a range of band gaps and lattice parameters, and wurtzite oxides also exist. My calculations indicate that we should see very large polarization charges at these interfaces, similar to the case of ScN/GaN. The methodology is also equally applicable to rocksalt/zinc-blende interfaces grown along the [100] direction, where a similar large polarization difference is expected.

In calculating the superlattices between ScN and GaN, I allowed ions to relax. Most relaxation occurred near the interface, and ions further from the interface did not move significantly. Most interestingly, the ions relaxed in such a manner as to reduce the polarization discontinuity between both materials (the polarization in the ScN layer was reduced, while the polarization in the GaN layer was increased). I think this effect should be studied more quantitatively, particularly as it relates to the ionic contribution to the dielectric constant. This effect has already been experimentally reported in PbSe/InAs interfaces using transmission-electron microscopy [120].

Lastly, there are issues to be addressed relating to the growth of ScN films on GaN due to the differences in symmetry. Experimental reports show that ScN films grown on GaN exhibit twinning, as the ScN (111) axis has 3-fold symmetry, while the GaN (0001) axis has 6-fold symmetry [121]. An alternative would be to look at other crystal structures,

for instance, the Zn-TM-N_2 materials (TM = Zr, Hf). These materials are a unique cross between the Zn-IV-nitrides and the rocksalt nitrides. The Zn atom is tetrahedrally bonded, while the TM atom is octahedrally bonded [122]. The crystal structure consists of alternating tetrahedral Zn layers with octahedral TM layers. It would be interesting to determine their effective spontaneous polarization, for potential heterostructures with the III-nitrides.

I am extremely optimistic the methodologies discussed in this thesis will have applications to a wide variety of materials.

Bibliography

[1] S. Nakamura, T. Mukai, and M. Senoh, Jpn. J. Appl. Phys. **30**, L1998 (1991).

[2] N. Zhang *et al.*, IEEE Electron Device Lett. **21**, 421 (2000).

[3] O. Ambacher *et al.*, J. Appl. Phys. **85**, 3222 (1999).

[4] P. C. Quayle *et al.*, Phys. Rev. B **91**, 205207 (2015).

[5] A. D. Martinez, A. N. Fioretti, E. S. Toberer, and A. C. Tamboli, J. Mater. Chem. A **5**, 11418 (2017).

[6] C. Freysoldt *et al.*, Rev. Mod. Phys. **86**, 253 (2014).

[7] H. Kroemer, Proc. IEEE **51**, 1782 (1963).

[8] W. Shockley, Bell Labs Tech. J. **28**, 435 (1949).

[9] M. Leroux *et al.*, Phys. Rev. B **58**, R13371(R) (1998).

[10] D. Jena *et al.*, Phys. Status Solidi A **208**, 1511 (2011).

[11] B. Biswas and B. Saha, Phys. Rev. Mater. **3**, 020301 (2019).

[12] R. M. Martin, *Electronic Structure: Basic Theory and Practical Methods* (Cambridge University Press, 2004).

[13] D. S. Sholl and J. A. Steckel, *Density Functional Theory* (John Wiley & Sons, Ltd, 2009).

[14] P. Hohenberg and W. Kohn, Phys. Rev. **136**, B864 (1964).

[15] J. P. Perdew, K. Burke, and M. Ernzerhof, Phys. Rev. Lett. **77**, 3865 (1996).

[16] J. Heyd, G. E. Scuseria, and M. Ernzerhof, J. Chem. Phys. **118**, 8207 (2003).

[17] J. Heyd, G. E. Scuseria, and M. Ernzerhof, J. Chem. Phys. **124**, 219906 (2006).

[18] C. Freysoldt, J. Neugebauer, and C. G. Van de Walle, Phys. Rev. Lett. **102**, 016402 (2009).

[19] C. Freysoldt, J. Neugebauer, and C. G. Van de Walle, Phys. Status Solidi B **248**, 1067 (2011).

[20] A. Baldereschi, S. Baroni, and R. Resta, Phys. Rev. Lett. **61**, 734 (1988).

[21] C. G. Van de Walle and J. Neugebauer, Nature **423**, 626 (2003).

[22] G. Kresse and J. Furthmüller, Phys. Rev. B **54**, 11169 (1996).

[23] G. Kresse and J. Furthmüller, Comput. Mater. Sci. **6**, 15 (1996).

[24] N. L. Adamski, Z. Zhu, D. Wickramaratne, and C. G. Van de Walle, J. Appl. Phys. **122**, 195701 (2017).

[25] N. L. Adamski, Z. Zhu, D. Wickramaratne, and C. G. Van de Walle, Phys. Rev. B **100**, 155206 (2019).

[26] N. L. Adamski, Z. Zhu, D. Wickramaratne, and C. G. Van de Walle, Appl. Phys. Lett. **114**, 032101 (2019).

[27] N. L. Adamski, D. Wickramaratne, and C. G. Van de Walle, J. Mater. Chem. C, Advance Article (2020), [doi:10.1039/D0TC01578D].

[28] N. L. Adamski, C. E. Dreyer, and C. G. Van de Walle, Appl. Phys. Lett. **115**, 232103 (2019).

[29] R. Resta and D. Vanderbilt, *Theory of Polarization: A Modern Approach* (Springer Berlin Heidelberg, Berlin, Heidelberg, 2007), pp. 31–68.

[30] R. Resta, Rev. Mod. Phys. **66**, 899 (1994).

[31] D. Vanderbilt and R. D. King-Smith, Phys. Rev. B **48**, 4442 (1993).

[32] R. D. King-Smith and D. Vanderbilt, Phys. Rev. B **47**, 1651 (1993).

[33] C. E. Dreyer, A. Janotti, C. G. Van de Walle, and D. Vanderbilt, Phys. Rev. X **6**, 021038 (2016).

[34] D. Vanderbilt, J. Phys. Chem. Solids **61**, 147 (2000).

[35] J. F. Nye, *Physical Properties of Crystals: Their Representation by Tensors and Matrices* (Clarendon Press, 1985).

[36] F. Bernardini and V. Fiorentini, Phys. Rev. B **64**, 085207 (2001).

[37] L. Han, C. Lieberman, and H. Zhao, J. Appl. Phys. **121**, 093101 (2017).

[38] L. Han, K. Kash, and H. Zhao, J. Appl. Phys. **120**, 103102 (2016).

[39] B. Hyot, M. Rollès, and P. Miska, Phys. Status Solidi RRL **13**, 1900170 (2019).

[40] B. R. Pamplin, J. Cryst. Growth **26**, 239 (1974).

[41] M. Maunaye and J. Lang, Mater. Res. Bull. **5**, 793 (1970).

[42] M. Wintenberger, M. Maunaye, and Y. Laurent, Mater. Res. Bull. **8**, 1049 (1973).

[43] T. Endo, Y. Sato, H. Takizawa, and M. Shimada, J. Mater. Sci. Lett. **11**, 424 (1992).

[44] A. Osinsky *et al.*, New concepts and preliminary results for SiC bipolar transistors: $ZnSiN_2$ and $ZnGeN_2$ heterojunction emitters, in *Proceedings 2000 IEEE/ Cornell Conference on High Performance Devices (Cat. No.00CH37122)*, pp. 168–172, 2000.

[45] L. Lahourcade *et al.*, Adv. Mater. **25**, 2562 (2013).

[46] P. Narang *et al.*, Adv. Mater. **26**, 1235 (2014).

[47] H. J. Monkhorst and J. D. Pack, Phys. Rev. B **13**, 5188 (1976).

[48] P. C. Quayle, K. He, J. Shan, and K. Kash, MRS Commun. **3**, 135 (2013).

[49] H. Jonas, S. Saskia, W. Peter, and S. Wolfgang, Chem. Eur. J. **23**, 12275 (2017).

[50] I. Vurgaftman and J. R. Meyer, J. Appl. Phys. **94**, 3675 (2003).

[51] A. Punya, W. R. L. Lambrecht, and M. van Schilfgaarde, Phys. Rev. B **84**, 165204 (2011).

[52] T. Misaki, A. Wakahara, H. Okada, and A. Yoshida, J. Cryst. Growth **260**, 125 (2004).

[53] S. Kikkawa and H. Morisaka, Solid State Commun. **112**, 513 (1999).

[54] R. Viennois *et al.*, Mater. Sci. Eng. B **82**, 45 (2001).

[55] F. Kawamura, N. Yamada, X. Cao, M. Imai, and T. Taniguchi, Jpn. J. Appl. Phys. **58**, SC1034 (2019).

[56] T. D. Veal *et al.*, Adv. Energy Mater. **5**, 1501462 (2015).

[57] T. Wang, C. Ni, and A. Janotti, Phys. Rev. B **95**, 205205 (2017).

[58] S. Chen, P. Narang, H. A. Atwater, and L.-W. Wang, Adv. Mater. **26**, 311 (2014).

[59] N. Tsunoda, Y. Kumagai, A. Takahashi, and F. Oba, Phys. Rev. Appl. **10**, 011001 (2018).

[60] D. Skachkov, A. Punya Jaroenjittichai, L.-Y. Huang, and W. R. L. Lambrecht, Phys. Rev. B **93**, 155202 (2016).

[61] A. Janotti and C. G. Van de Walle, Phys. Status Solidi B **248**, 799 (2011).

[62] B. Himmetoglu, A. Floris, S. Gironcoli, and M. Cococcioni, Int. J. Quantum Chem. **114**, 14 (2014).

[63] C. Freysoldt *et al.*, Phys. Rev. B **93**, 165206 (2016).

[64] D. D. Wagman, W. H. Evans, and V. B. Parker, J. Phys. Chem. Ref. Data **11**, Supplement No. 2 (1982).

[65] C. Qin, L. Gao, and E. Wang, *Germanium: Inorganic Chemistry* (John Wiley & Sons, Ltd, 2006), pp. 1–21.

[66] P. O'Hare, I. Tomaszkiewicz, I. C.M. Beck, and H.-J. Seifert, J. Chem. Thermodyn. **31**, 303 (1999).

[67] P. O'Hare and G. K. Johnson, J. Chem. Thermodyn. **7**, 13 (1975).

[68] O. Madelung, *Semiconductors-Basic Data, 2nd revised ed.* (Springer, Berlin, 1996).

[69] A. Nasar and M. Shamsuddin, Thermochim. Acta **205**, 157 (1992).

[70] M. W. Chase, *NIST-JANAF Thermochemical Tables, 4th Edition* (American Institute of Physics, 1998).

[71] R. C. Schoonmaker, A. R. Venkitaraman, and P. K. Lee, J. Phys. Chem. **71**, 2676 (1967).

[72] A. S. Jordan, J. Electrochem. Soc. **118**, 1362 (1971).

[73] J. L. Lyons and C. G. Van de Walle, npj Comput. Mater. **3**, 12 (2017).

[74] A. Janotti and C. G. Van de Walle, Nat. Mater. **6**, 44 (2007).

[75] A. Janotti and C. G. Van de Walle, Appl. Phys. Lett. **92**, 032104 (2008).

[76] J. S. Dyck, J. R. Colvin, P. C. Quayle, T. J. Peshek, and K. Kash, J. Electron. Mater. **45**, 2920 (2016).

[77] D. Skachkov, P. C. Quayle, K. Kash, and W. R. Lambrecht, Phys. Rev. B **94**, 205201 (2016).

[78] L. Gordon, J. B. Varley, J. L. Lyons, A. Janotti, and C. G. Van de Walle, Phys. Status Solidi RRL **9**, 462 (2015).

[79] A. M. Shing, N. C. Coronel, N. S. Lewis, and H. A. Atwater, APL Mater. **3**, 076104 (2015).

[80] A. N. Fioretti *et al.*, J. Mater. Chem. C **3**, 11017 (2015).

[81] J. S. Harris *et al.*, Appl. Phys. Lett. **112**, 152101 (2018).

[82] R. D. Shannon, Acta Crystallogr. A **32**, 751 (1976).

[83] T. Mattila and A. Zunger, Phys. Rev. B **58**, 1367 (1998).

[84] C. G. Van de Walle and J. Neugebauer, Appl. Phys. Lett. **76**, 1009 (2000).

[85] J. L. Lyons, A. Janotti, and C. G. Van de Walle, Phys. Rev. Lett. **108**, 156403 (2012).

[86] S. Nakamura, T. Mukai, M. Senoh, and N. Iwasa, Jpn. J. Appl. Phys. **31**, L139 (1992).

[87] J. L. Lyons, A. Janotti, and C. G. Van de Walle, J. Appl. Phys. **115**, 012014 (2014).

[88] J. Neugebauer and C. G. Van de Walle, Phys. Rev. Lett. **75**, 4452 (1995).

[89] G. Henkelman, B. P. Uberuaga, and H. Jónsson, J. Chem. Phys. **113**, 9901 (2000).

[90] G. Henkelman and H. Jónsson, J. Chem. Phys. **113**, 9978 (2000).

[91] J.-S. Park and K. J. Chang, Appl. Phys. Express **5**, 065601 (2012).

[92] C. H. Seager, S. M. Myers, A. F. Wright, D. D. Koleske, and A. A. Allerman, J. Appl. Phys. **92**, 7246 (2002).

[93] A. Punya and W. R. L. Lambrecht, Phys. Rev. B **88**, 075302 (2013).

[94] A. P. Jaroenjittichai, S. Lyu, and W. R. L. Lambrecht, Phys. Rev. B **96**, 079907 (2017).

[95] R. Cao, H.-X. Deng, J.-W. Luo, and S.-H. Wei, J. Semicond. **40**, 042102 (2019).

[96] P. G. Moses, M. Miao, Q. Yan, and C. G. Van de Walle, J. Chem. Phys. **134**, 084703 (2011).

[97] T. R. Paudel and W. R. L. Lambrecht, Phys. Rev. B **79**, 245205 (2009).

[98] S. F. Chichibu *et al.*, Appl. Phys. Lett. **73**, 2006 (1998).

[99] U. K. Mishra, P. Parikh, and Y.-F. Wu, Proc. IEEE **90**, 1022 (2002).

[100] M. C. Schmidt *et al.*, Jpn. J. Appl. Phys. **46**, L190 (2007).

[101] D. F. Feezell, M. C. Schmidt, S. P. DenBaars, and S. Nakamura, MRS Bull. **34**, 318 (2009).

[102] A. Kyrtsos, M. Matsubara, and E. Bellotti, Phys. Rev. B **99**, 035201 (2019).

[103] A. Janotti and C. G. Van de Walle, Phys. Rev. B **75**, 121201 (2007).

[104] Q. Yan *et al.*, Semicond. Sci. Tech. **26**, 014037 (2010).

[105] H. Fu, J. C. Goodrich, O. Ogidi-Ekoko, and N. Tansu, J. Appl. Phys. **126**, 133103 (2019).

[106] M. Akiyama *et al.*, Adv. Mater. **21**, 593 (2009).

[107] S. Fichtner, N. Wolff, F. Lofink, L. Kienle, and B. Wagner, J. Appl. Phys. **125**, 114103 (2019).

[108] F. Perjeru, X. Bai, M. Ortiz-Libreros, R. Higgins, and M. Kordesch, Appl. Surf. Sci. **175-176**, 490 (2001).

[109] J. Hall *et al.*, J. Cryst. Growth **311**, 2054 (2009).

[110] M. Moram *et al.*, J. Cryst. Growth **308**, 302 (2007).

[111] S. W. King, R. J. Nemanich, and R. F. Davis, Appl. Phys. Lett. **105**, 081606 (2014).

[112] A. Nakajima, Y. Sumida, M. H. Dhyani, H. Kawai, and E. M. S. Narayanan, Appl. Phys. Express **3**, 121004 (2010).

[113] M. A. Khan, J. N. Kuznia, J. M. Van Hove, N. Pan, and J. Carter, Appl. Phys. Lett. **60**, 3027 (1992).

[114] J. Simon *et al.*, Phys. Rev. Lett. **103**, 026801 (2009).

[115] S. Krishnamoorthy, F. Akyol, P. S. Park, and S. Rajan, Appl. Phys. Lett. **102**, 113503 (2013).

[116] Y. Jiao, Y. Zheng, M. Jaroniec, and S. Z. Qiao, Chem. Soc. Rev. **44**, 2060 (2015).

[117] H. A. Al-Brithen, A. R. Smith, and D. Gall, Phys. Rev. B **70**, 045303 (2004).

[118] L. Weston, H. Tailor, K. Krishnaswamy, L. Bjaalie, and C. G. Van de Walle, Comput. Mater. Sci. **151**, 174 (2018).

[119] F. Bernardini, V. Fiorentini, and D. Vanderbilt, Phys. Rev. Lett. **79**, 3958 (1997).

[120] B. B. Haidet, E. T. Hughes, and K. Mukherjee, Phys. Rev. Mater. **4**, 033402 (2020).

[121] J. Casamento, J. Wright, R. Chaudhuri, H. G. Xing, and D. Jena, Appl. Phys. Lett. **115**, 172101 (2019).

[122] C. Tholander, C. B. A. Andersson, R. Armiento, F. Tasnádi, and B. Alling, J. Appl. Phys. **120**, 225102 (2016).